SYNTHESIS AND CHARACTERIZATION OF GLASS-CERAMIC MATERIALS FOR OPTICAL APPLICATIONS

by

IVAN POPOV

A dissertation submitted to the Graduate Faculty in Chemical Engineering in partial fulfillment of the requirements for the degree of Doctor of Philosophy,
The City University of New York

2009

Approval Page

This manuscript has been read and accepted for the
Graduate Faculty in Engineering in satisfaction of the
dissertation requirement for the degree of Doctor of Philosophy.

Dr. Leslie L. Isaacs
Chair of the Examining Committee

Mumtaz Kassir
Executive Officer

Dr. Vladimir Petricevic
Dr. Jeffrey Steiner
Dr. Ilona Kretzschmar
Dr. Brian J. Fitzpatrick
Supervisory Committee

THE CITY UNIVERSITY OF NEW YORK

Abstract

SYNTHESIS AND CHARACTERIZATION OF HYBRID MATERIALS FOR OPTICAL APPLICATIONS

by

IVAN POPOV

Advisors: Professor Leslie L. Isaacs and Professor Vladimir Petricevic

Porous glass impregnation with Cr-doped olivine nano-crystallites, and synthesis and devitrification behavior of Cr-doped $CaO–GeO_2–Li_2O–B_2O_3(Al_2O_3)$ glasses have been studied. A range of glass compositions was found to yield transparent glass-ceramics after devitrification. The size of crystallites is below 1 μm. Glass-ceramic samples exhibit broad-band emission in the 1050-1600 nm spectral range, with a maximum around 1260 nm, very similar to the emission of $Cr^{4+}:Ca_2GeO_4$ bulk crystals. X-ray diffraction measurements indicate that the structure of crystallites exhibiting near infrared emission in glass-ceramics may be assigned to $Cr^{4+}:Ca_2GeO_4$ with increased lattice parameters. Nucleation and crystallization kinetics of Cr-doped $CaO–GeO_2–Li_2O–B_2O_3(Al_2O_3)$ glasses were investigated. Activation energies were 530 KJ/mol for nucleation and 415KJ/mol for crystallization. The Avrami coefficient was found to be 3.7, suggesting 3-dimensional bulk crystallization within the glass.

Acknowledgements

First I would like to express my sincere gratitude to my thesis supervisors, Professors Leslie Isaacs and Vladimir Petricevic, for giving me an opportunity to undertake my graduate studies and for all their support in my research project. I also thank them for introducing to me to all the wonders and frustrations of scientific work.

I am also very grateful to Dr. Alexei Bykov who has been a mentor in these years of my graduate studies. His numerous helpful advices and inspiring discussions helped me learn and understand many concepts that were foreign to me. Dr. Alexei Bykov was involved in many aspects of my research project.

I would like to thank my committee members Dr. Jeffrey Steiner and Dr. Ilona Kretzschmar for their helpful advices and words of encouragements in difficult situations.

I would also like to thank Dr. R. Alfano and the Center for Advanced Technology for Ultrafast Photonics at City College for providing financial support under NASA/DoD research grants..

My eternal gratitude goes to my beautiful wife Jennifer, son Dimitri and my parents for their everlasting love and support. I love them with all my heart and without them none of this would have been possible.

TABLE OF CONTENTS

LIST OF FIGURES

LIST OF TABLES

CHAPTER 1

INTRODUCTION

1.1 Background

New materials for ultra wide band optical fiber amplifiers in the near infrared (NIR) spectral range between 1100 nm – 1600 nm are of great importance for current and future optical communication systems. Cr^{4+}-doped materials have the potential for amplifying thousands of channels in wavelength division multiplexing (WDM) systems and for free space optical communications. Tetravalent chromium (Cr^{4+}) is the main ion emitting light at optical fiber communication (1.31μm and 1.55μm) and eye-safe wavelength region (>1.4μm). The Cr^{4+} lasers and amplifiers can be used for fiber optics, remote sensing, biomedical imaging, and free space communications. Over the past decade a number of new Cr^{4+}-doped materials have been developed at CCNY including Cr^{4+}:Mg_2SiO_4 (forsterite) and Cr^{4+}:Ca_2GeO_4 (Cunyite) operating in such near-infrared (NIR) region [1-4].

Since glasses are excellent materials for fiber optic devices while single crystals are not, there were many attempts to develop Cr^{4+}-doped bulk glasses for fiber optics application. Over the past several years, the search for Cr^{4+}-activated materials has been expanded from crystalline to Cr^{4+}-doped glass hosts. However, Cr^{4+}-doped glasses exibit strong nonradiative processes that completely suppress the radiative emission and laser action.

In contrast, glass-based hybrid materials containing nanometer-to micro-sized Cr^{4+}-doped crystals embedded in a glass matrix are intermediate materials between bulk crystals and glasses. This combination gives favorable radiative properties of Cr^{4+}-doped single crystals and the advantages of glasses for fiber optics.

Glass-ceramics are polycrystalline, two-phase materials formed by controlled crystallization heat treatment of appropriate parent glasses, a process known as ceramming. Their microstructure consists of a high concentration of small crystals uniformly distributed in a residual glass phase. They are easier to manufacture into complex shapes than traditional ceramics utilizing standard techniques developed for the glass industry. In addition, the embedded crystallite phase can enhance existing, or offer entirely new properties from those of the parent glass. Recent progress in fiberization of glass ceramic materials has already led to the demonstration of rare earth doped fiber lasers and amplifiers with an efficiency unaffected by the presence of the crystals embedded within the core of the single mode fiber. However, to date the synthesis process and optical properties of Cr^{4+}-doped glass-ceramic systems have received little attention, despite the apparent advantages of crystal size control.

Nucleation and crystallization of glasses are topics of technological as well as scientific interest and importance. Crystallization that usually must be avoided entirely in glasses, in certain applications, (including Cr^{4+}-doped glass-ceramic materials) is desired, but it must occur in a controlled manner. Crystallization of laser olivines (Cr^{4+}:Mg_2SiO_4, Cr^{4+}:Ca_2GeO_4 and appropriate solid solutions) in glasses has never been considered,

except for Cr^{4+}:Mg_2SiO_4 glass ceramics. Therefore, the first key problem is to find the appropriate composition of glass for crystallization of Cr^{4+}:Ca_2GeO_4 during the after growth heat-treatment procedure. Once the right composition is found, optimization of the optical properties of the glass is necessary for making fiber lasers and amplifiers. The subject of this thesis is synthesis and characterization of glass-ceramic materials for optical applications, as outlined in the section below.

1.2 Scope of the Thesis

The goal of the research was to create new hybrid materials based on nanosize laser active crystallites embedded into transparent glass matrix. Our efforts were concentrated in the two following areas:

1. Development of porous glasses impregnated with Cr-doped olivine laser nano-crystallites, and
2. Development of glasses with ability to form glass-ceramics nucleated with Cr-doped olivine laser nano-crystallites after devitrification procedure.

The tasks to be accomplished included:

Porous glasses -

- synthesing of nano-sized Cr-doped laser germanates belonging to the olivine-type structure (Ca_2GeO_4, Mg_2GeO_4);
- making porous glass matrix with sol-gel method using known sol-gel techniques;
- studying liquid solution impregnation and crystallization processes in nano-sized pores
- studying optical behavior of nano- crystallites and compare them with the bulk media

Glass-ceramics -

- searching for appropriate glass compositions and synthesis of glasses with desired devitrification behavior, i.e. predictive devitrification associating with homogeneous nucleation and growth of nano-sized crystallites, particularly Cr^{4+}:Ca_2GeO_4;
- studying kinetics of nucleation and crystallization in glass media during devitrification;
- studying optical properties (absorption, fluorescence) of Cr-doped parent glasses and glass-ceramics after devitrification.

CHAPTER 2

LITERATURE REVIEW

2.1 Introduction

Glass ceramic materials are polycrystalline solids containing nanometer to micrometer sized crystals. These polycrystalline solids are embedded in an amorphous glass matrix and are produced by a process which is referred to as “devitrification of glasses”. The first step toward this transition process involves conventional techniques for glass production, followed by crystallization under carefully controlled operating conditions. This post-treatment of amorphous glass then leads to the separation of a crystalline phase from the glassy parent phase. The crystals so formed are in the nano- to micro- size range. The form of these newly formed crystals, their absolute number embedded in the amorphous vitreous solid, their growth rate and their final size are controlled by a suitable heat treatment for the solids system in question[5].

Generally speaking glass ceramics find use not only because of their desirable mechanical and thermal stability, but also due their electric, magnetic and optic

properties. Transparent glass ceramics produced from aluminosilicates were used initially for LCD displays and storage devices for compters. In recent years, however, a significantly increased interest in other optical application of glass ceramics has developed. Transparent fluoride rare earth optical vitroceramics (FROGS), combining the low phonon energy of fluorides with chemical stability of oxides, show large infrared to visible upconversion more efficient than the parent glass. This is because rare earth ions are preferentially incorporated into the fluoride crystal lattice structure [6,7]. Recently, second harmonic generation in β-barium borate crystals embedded in borate glass matrix and on surface crystallizated glass of $LaBGeO_5$ has been observed in borate glass systems. [8,9].

Glass-ceramics, in contrast to sintered ceramic materials, are produced when an appropriate thermal treatment is applied. The tendency of vitreous amorphous material to change from an amorphous state into a partial crystalline state yields the opportunity of in situ crystallization of a glass melt upon a suitable heat treatment. Generally speaking, homogeneous glass has isotropic properties. When anisotropic properties are to be obtained in glass ceramics, then suitable driving forces have to be supplied in order to bring about this change in properties. The application of a temperature gradient or of an electric or magnetic field during the crystallization, have been found to be proven methods to achieve preferred crystal orientations. Yet another method for obtaining anisotropic glass-ceramics is by means of extrusion of the glass material through an orifice. During the extrusion process the unidirectional deformation of the glass melt generates shear flow, which in turn causes alignment of structure [10].

2.2 Influence of Nucleation Agents

Generally speaking, nucleation agents promote nucleation either by accelerating the process of phase separation, or by lowering the energy barrier of nucleation. There are two accepted mechanisms, namely the heterogeneous nucleation of the oxide phase and also the metastable separation mechanism, by which nucleation agents are though to be functioning [10].

During heterogeneous nucleation of the oxide phase added metallic nucleants such as Au, Ag, Cu, Pt and Pd are involved. It is believed that during melting the added nucleating agents pass into solution and are subsequently precipitated only at relatively low temperature. This is because of a strong decrease in solubility in the melt and a simultaneous reversion of the nucleation agent back into its metallic form.

On the other hand, during metastable separation, initiation of nucleation in glass is presumed to proceed when oxidic agents such as TiO_2, ZrO_2, P2O5, Cr_2O_3 are present. Other highly efficient nucleating agents include fluorides and sulphides.

2.3 Glass and its Crystal Structure

Prior to Zachariasen's Random Network Theory [11], it was believed that glass structures were comprised of nanocrystals with sizes in the range of 8 - 10 Å. This estimate of their size range was found from the broadening of diffraction patterns. It was reasoned that the similarities in mechanical properties of glasses in general and crystals is based upon their measured dimensions and they were expected to have similar structural energies. The author [11] suggested therefore, that glasses and crystals may have the same cationic polyhedral building blocks, but arranged in different patterns, but where glasses have a broader distribution of bond angles.

Based upon Ostwald's rule of successive reactions [12], the nanocrystallite model is supported by the observation that the first devitrification product of a glass may reflect the structural features that are present in glass. It was found that when melting a crystalline phase, on subsequent recrystallization of the glass the same crystalline phase is obtained as was present prior to melting of the glass. Glass-forming oxides produce very viscous liquids. The viscosity of metal oxides at elevated temperatures is related to the structure of the oxide and the bonding between the particles.

During the crystallization process of a metal oxide liquid, many strong ionic bonds must break and reorganization at the atomic level must occur. Therefore it is of interest to learn

whether there exists a relationship between the structures of glasses and the crystals formed from these glasses. Muller et al. [13] investigated, using silicates, the relationship between homogeneous nucleation behavior and the structure of crystals which were formed from the parent glasses melt. Their main assumption was that in the event of the local structure of a glass and its isochemical crystal being similar, then only a few interfacial rearrangements will be necessary for crystal nucleation. In the event that these rearrangements are substantial, then nucleation can only occur on the external surfaces, assisted by unsaturated bonds and solid impurities at the surface. On the other hand, if they occur in volume, then this may proceed only with the aid of nucleating agents.

2.4 Transparent Glass-Ceramics

Transparency of a substance is critical for its optical applications. Heterogeneities, like grain boundaries, composition gradients, lattice imperfections, to name only a few, cause loss to transparency due to light scattering. In order to behave as an effective optical medium for light propagation, certain criteria must be met [11]:

- small particle size
- interparticle spacing comparable with the crystal size
- narrow particle size distribution.

The intensity of transmitted light is shown by the following equation [14]:

$$T = \exp\left(\frac{-3 \cdot r^3 \cdot V_{\mathrm{h}} \cdot d \cdot \left|\frac{n_{\mathrm{crystal}}}{n_{\mathrm{glass}}} - 1\right|}{4 \cdot \lambda^4}\right) \tag{2.1}$$

where:

V_h is the volume fraction of the heterogeneity

r is the radius of heterogeneity

d is the thicknessof material

λ denotes the wavelength of incident the light

$n_{crystal}$, n_{glass} are the refractive indices of crystal and of glass, respectively.

The expression 2.1 shows that the attenuation of light depends on the difference between the refractive indexes of the glass and the crystal, as well as between the size and distribution of crystals in the glass. Therefore it is imperative that a transparent glass ceramic be present to grow small crystals in the glass matrix. It is furthermore necessary that the glassy and the crystalline phases have a similar value of their refractive indexes[14].

2.5 Preparation of the Glass-Ceramic Materials

The typical sequence for glass ceramics preparation involves nucleation of a small volume fraction of the glass followed by bulk growth of crystals. The nucleation step is carried out at lower temperatures, presumably to obtain higher driving forces. The growth step during crystallization is carried out at higher temperatures in order to obtain higher growth rates due to a more rapid diffusion. The glasses initially used for the preparation of glass-ceramic materials were prepared by cooling of glass forming melts.

The heat treatment schedule is described in Fig. 2.1. The temperature and duration of both holding periods have great significance. The process schedule was based upon the assumption that during the first holding period, homogeneous as well as heterogeneous nucleation will take place simultaneously. It is quite conceivable though that the two nucleation processes peak at different temperatures and a large number of nuclei in an amount of about 10^{12} - 10^{15} nuclei / cm^3 are created.

The rate of melt heating is also a significant factor because the glass transition temperature could be higher at a fast temperature ramp rate, while it could be lower at a slow temperature ramp rate.

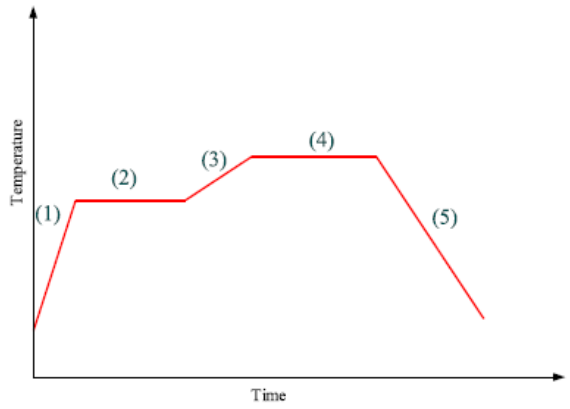

Fig. 2.1 Thermal treatment schedule for glass-ceramics: (1) heating the glass from room temperature, (2) nucleation stage, (3) increasing temperature, (4) crystallization stage, and (5) cooling down to room temperature.

Glass typically consists of:

- glass (or network) formers (SiO_2 and B_2O_3)-
- fluxes which are also called alkali metal oxides (K_2O and Na_2O) –
- network or matrix modifying alkaline earths, like (CaO, BaO, PbO,and ZnO).

Other oxides capable of forming glass network include GeO_2, P_2O_5, As_2O_5, As_2O_3, Sb_2O_3, and to a limited extent V_2O_5, ZrO_2 and Bi_2O_3. The oxides of Ti, Zn, Pb, Al, Th and Be can be included in the network in varying concentrations, however, they will not on their own, yield a glass. These, and other oxides that will not form a glass (including Sc, La, Y, Sn, Ga, In, Mg, Li, Sr, Cd, Rb, Hg, and Cs) are known as network modifiers and are used in this capacity in the formation of glass. Oxygen ions are bridging and also non-bridging entities within the glassy matrix. In a typical glass these anions bond to cations,

like Li^+, Na^+, K^+ or Ca^{++}. Hence, technically speaking, glass is a metal oxide polymer with SiO_2 the principal copolymer of all commercial glasses [15].

Pure SiO_2 glass is commonly referred to as fused quartz. It can be manufactured from rock quartz crystals which lack flux or matrix modifiers. The uninterrupted strands of the Si-O bonds yield fused quartz which is known as a ‘hard” glass with a very high softening temperature. When the Si-O matrix is occasionally interrupted by modifying ions, which are characterized by weaker metal-O bonds, then the presence of the modifying ions will lower the viscosity profile of the glass and render it ‘soft’. It can be generally stated that with higher concentrations of alkaline earth oxides present in glass, its viscosity profile will be depressed. This is glass when everything 'goes right'. When glass devitrifies, it doesn't necessarily revert to its former, solid, crystalline constituents. In many instances a devitrified glass will not be chemically altered, but rather it will crystallize into its ceramic analogue. The presence of the phosphorus oxide is known to increase nucleation densities: without this addition, glass ceramics typically have rather coarse microstructures, which makes them of limited value for practical use.

Glasses cannot be looked upon as "frozen liquids." On close examination one notices the variance of the molar volume of a specific glass with a specific composition vs. temperature, there is a specific temperature level, i.e. the glass transition temperature, Tg.

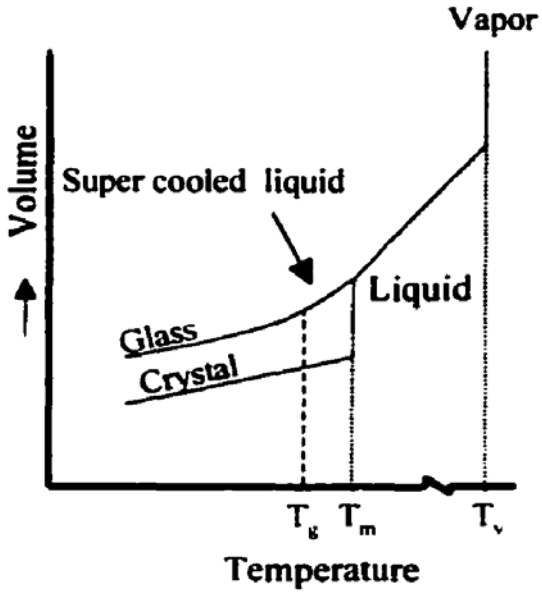

Figure 2.2. Volume - temperature relations for liquid, crystal, and glass phases [16]

The slope of the curve Fig. 2.2 above the Tg is characteristic of a liquid, however, below the Tg the slope is more characteristic for solid-like materials. A change in molar volume is observed upon crystallization.

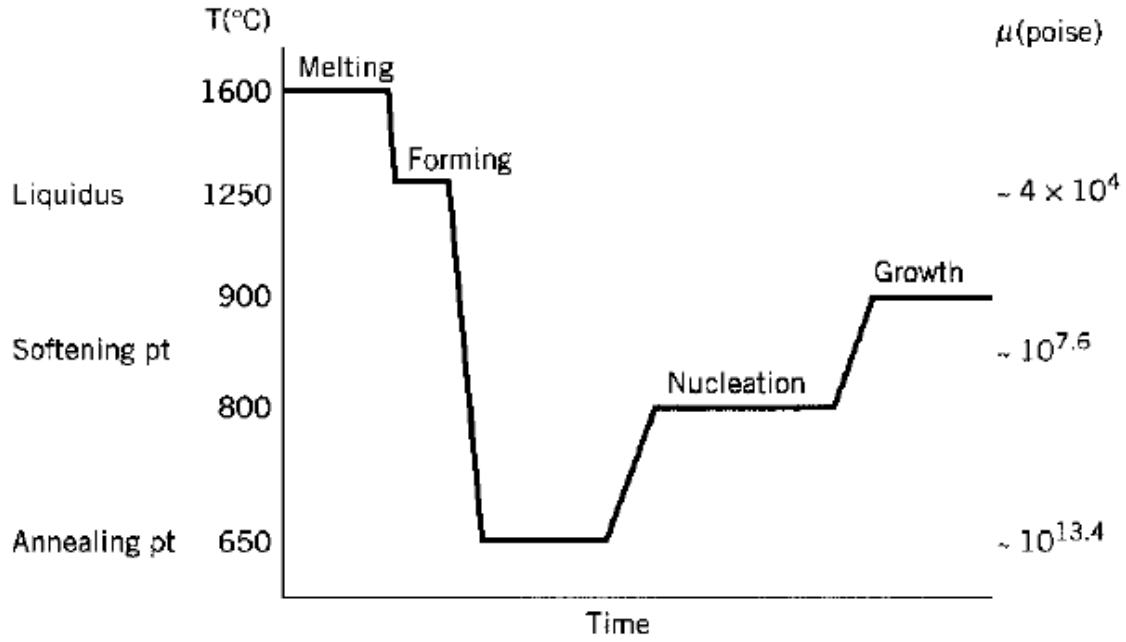

Figure 2.3 Typical processing cycle of LiO_2-Al_2O_3-SiO_2 glass ceramic [17].

Figure 2.3 shows that there are three specific temperature levels which relate to the glass transition temperature of a vitreous material, namely the working point, the softening point and the annealing point.

The working point is at a temperature where the viscosity of the material is in the range of (η)=10^4 cp. The melting point is at a temperature level where the viscosity of the material in question has a viscosity in the range of □=$10^{7.6}$ cp, and finally the annealing point is reached when the viscosity of the glass is in the range of □=$10^{13.4}$ cp. The annealing point of a specific glassy material can also be described as that point at which

internal stresses within the glass material will be relieved within a time period of 15 minutes. The viscosity at the glass transition temperature is in the range $\eta=10^{13\text{-}14.5}$ [14].

The ratio of ionic structure radii provides is an excellent guide to the stability of ionic structures, as well as other crystalline structures. They do not, however, adequately describe the conditions under which glasses are stable. Additional criteria are required to more fully define glass stability characteristics. Zachariasen [12] suggested a set of rules which may be applied to formulate the stability of glass and are analogous to Pauling's rules for crystal structure stability [18]. These are as follows:

Rule No. 1 - each oxygen atom is linked to no more than two cations.

Rule No. 2 - the number of oxygen atoms surrounding the cation must be small, i.e. the number of cations cannot exceed 4.

Rule No. 3 - the oxygen polyhedra may only share corners, never edges of faces.

Rule No. 4 - at least three corners of each oxygen polyhedra are shared.

The above rules proved to be very useful to explain network forming capability of B_2O_3, GeO_2, P_2O_5, SiO_2, to name only a few.

2.6 Nucleation and Crystal Growth in Glass Ceramics.

Glass is defined as:"an inorganic product of fusion which has been cooled to rigid condition without crystallization" [19]. The dominant difference between a glass and a crystal is the random arrangement of long chain molecular structures in the former and the high degree of molecular order in the crystal structures [20]. This is not to say that all materials have to be in either a random order of molecular arrangement or in a crystalline state of molecular order. It is a common occurrence in natural products as well as in man-made products that crystalline areas are interrupted by amorphous regions. These types of materials are generally referred to as "semi-crystalline" and have physical properties which are neither typical for "glass", by definition, nor for pure crystalline materials. The transition of any material from a viscous liquid state to a solid glassy state is called the"glass transition" and the corresponding temperature is referred to "T_g". The reversible transformation from a glassy state into a viscous liquid state takes place when glass is heated to a temperature above its T_g. A change in viscosity also occurs at the glass transition temperature. It has been found that the rate of viscosity increase is dependent on the cooling rate of the material under study, and the glass transition temperature,T_g, in turn is not always the same for a given material, but also depends on the cooling rate.

In the event that the chemical composition of two materials are the same, then their glass transition temperatures need not necessarily be the same, as the rate of cooling during their transitions from a viscous liquid state into a solid state will impact their respective glass transition temperatures.

The Figure 2.2 shows the volume-temperature relationship of a typical glass-forming melt system. A slow cooling allows enough time for a viscous liquid to alter its local atomic arrangement in order to attain a minimum free energy level at the corresponding temperature. Conversely, a rapid cooling rate of the material causes an increase of viscosity that is too quick for the local atomic arrangement to follow. The cooling rate also impacts the structure of the glass. When one compares two chemically identical glass materials which were cooled at different cooling rates, then it is found that the structure of a rapidly cooled glass is more "open" as compared to the slowly cooled glass. This observation may be explained on the basis of the atomic arrangements in the glass materials under study. Rapidly cooled glass "freezes" the chain structures in a random arrangement, whereas in slowly cooled glass the chain structure is allowed to align itself to the lowest free energy composition. It is therefore safe to say that two chemically identical glassy materials show different physical properties, depending on their rate of cooling from the liquid state into the solid state.

An amorphous glass material of broad random atomic arrangement has higher configurational entropy, and therefore a higher free energy, than a crystalline material of the same chemical composition. Glass is therefore generally referred to as a thermodynamically metastable material. The transformation of an amorphous glass into a crystalline state proceeds initially via the pathway of nucleation, followed by crystal growth. The driving force for this transformation is the difference in free energy between the crystal and the glass, ΔG_v. The value of ΔG_v increases, as the numerical value of supercooling, referred to as change in reduced temperature, ΔT_r, also increases [21].

Upon the formation of solids from a liquid, specific interfaces are created. Free energy levels are associated with these interfaces and the total free surface energy increases as the solid grows. There are two competing effects recognized with a drop in temperature:

1. the increased difference in free energy levels between the crystalline state and liquid state of the system favors crystallization
2. the increasing viscosity, however, between the solid state and liquid state reduces the tendency for crystals to form within the system.

Nucleation is referred to as a tri-dimensional process, which involves the formation of longer range atomic order, followed by the growth of the existing crystals. Growth is referred to as a bi-dimensional process (on the surface of existing crystals).

Nucleation can also be described in terms of the free energy balance between the creation of a new crystal and new surfaces created as the crystals grow. Forming nuclei smaller than their critical sizes causes an initial increase in free energy due to the necessity to create surfaces and is therefore thermodynamically unfavorable. The free energy reaches a maximum as the initial nuclei grow larger, but becomes negative as the nuclei grow larger and form into stable nuclei. This is shown in Figure 2.4 below. The nucleation rate, I_0, as well as the crystal growth rate, U, both depend on the viscosity and ΔG_v of the system.

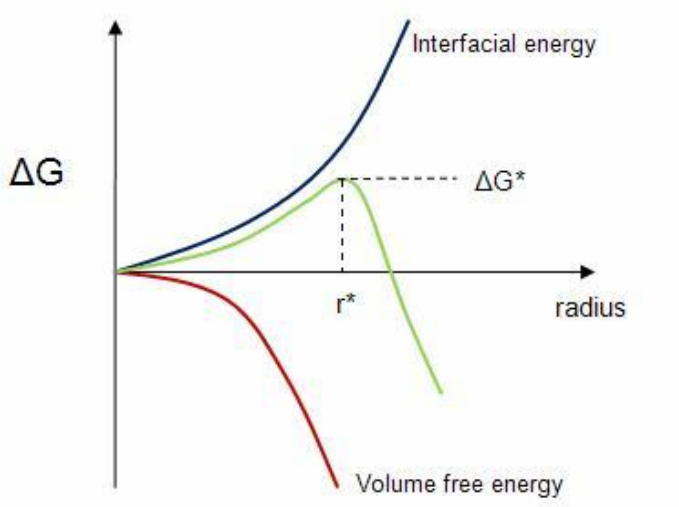

Fig. 2.4 Critical radius versus the change in free energy ΔG[22].

The "Ostwald Ripening" is a spontaneous process that occurs because larger crystals are energetically more favored than smaller crystals. Therefore the formation of many small crystals are kinetically favored, rather than the formation of a few large crystals. It can be shown by simple mathematics that small crystals have a larger surface area to volume ratio than large crystals. It is also well established that molecules located on the surface of a solid are energetically less stable and more easily move than those which are located in an order packed arrangement in the interior of the same solid. From the above can therefore be concluded that large crystals, with their greater volume to surface area ratio, represent a lower energy state. Thus, many small crystals will attain a lower energy state if transformed into a smaller number of larger crystals. This is the basis for what has become "Ostwald ripening".

The nucleation of a large number of small crystals, however, also reduces the degree of supersaturation and therefore the thermodynamically favored formation of large crystals

is no longer favored. Initially numerous small crystals form in a liquid system, however, slowly disappear except for a few that grow larger, at the expense of the small crystals. The areas around large crystals are then depleted of small crystals as the larger crystals continue to grow. The so-called "Ostwald Ripening" is also referred to as the process of growth of larger size crystals from those of smaller size, as the latter have a higher solubility in the liquid phase of the system than the larger ones have [23].

Assuming the product phase consists of spherical particles, the free energy released by transformation is proportional to the volume, and the free energy that's consumed by creation of the interface is proportional to the surface area of particles and the interfacial energy, γ, the net change in free energy per particle, ΔGr, is then given by:

$$\Delta Gr = -4\pi/3r^3\Delta Gv + 4\pi r^2\gamma \qquad (2.2)$$

By differentiating this equation to find the stationary point (at which the rate of change of free energy turns negative), the critical radius and critical energy can be found and are given by the following:

$$r^*=2\gamma/\Delta Gv \qquad (2.3)$$

and

$$\Delta G^*=16\pi\gamma^3/3\Delta Gv^2 \qquad (2.4)$$

To calculate the nucleation rate two factors are needed: population density of the embryos of the critical size and the rate at which these embryos are formed. Population,

or concentration, of these critical embryos, N*, is given by a Boltzmann factor, where N_0 is the number of atoms per unit volume:

$$N^* = N_0 \exp^{-(\Delta G^*/kT)} \quad (2.5)$$

where,

$$\Delta G^* = 16\pi\gamma^3/3(\Delta Gv - \Delta Gs)^2 \quad (2.6)$$

It should be noted in the above equation that ΔGs, which is the elastic energy cost for creation of a new phase, is subtracted from ΔGv since volume changes on transformation are significant and the elastic energy is symmetric (net tension or compression leads to an increase in elastic energy). Thus, the elastic energy is subtracted in proportion to the volume of the new phase.

The rate at which a critical embryo is formed, f, depends on the diffusion of the atoms, which is also given by a Boltzmann factor, where ΔG_{bulk} is the activation energy of bulk diffusion, and ω is of the same order as the atomic jump frequency:

$$f=\omega \exp^{-(\Delta Gbulk/kT)} \quad (2.7)$$

The product of N* and f is the homogeneous nucleation rate and given by the following equation [24]:

$$N = f C^* = \omega \exp\left\{-\frac{\Delta G_{bulk}}{kT}\right\} C_0 \exp\left\{-\frac{16\pi\gamma^3}{3\left(\frac{\Delta H \Delta T}{T_e} - \Delta G_S\right)^2 kT}\right\} \text{ [number/m}^3\text{/s]} \quad (2.8)$$

$\Delta T = T_m - T$. The higher the melt viscosity η at the crystallization temperature,Tm, the lower its crystallization. Qualitatively, the tendency of lower crystallization can be explained by an increased inhibition of motion or molecular rearrangement of the basic units of the melt with increasing viscosity.

If the same arguments are used as for nucleation rates, the crystal growth rate can be calculated using the following equation [26]:

$$U = (kT/3\pi a_0^2/\eta)[1- \exp^{-(\Delta G/kT)}] \quad [\mu/min] \quad (2.9)$$

The process of crystallization can be controlled if the nucleation and growth rate curves are separated as can be seen from Fig. 2.5.

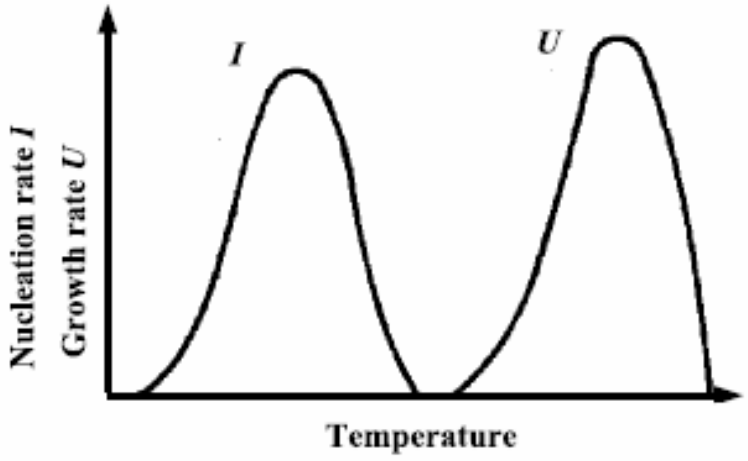

Figure 2.5: Temperature dependence of nucleation rate I and crystal growth rate U.

In the absence of catalyzing agents most supercooled liquids crystallize heterogeneously from the external surfaces. When heated only a few systems undergo bulk crystallization. Most systems favor surface nucleation where the surface of the medium nucleates first, followed by rapid crystallite growth. It was observed for the case of homogeneous nucleation that the reduced glass transition temperature, $T_{gr} = T_g/T_m$, must have a low value ($T_{gr} < 0.58$) and in this case the maximum nucleation rate is above T_g. Where,

Tgr is the reduced glass transition temperature,

Tg is the actual glass transition temperature,

Tm is the crystallization point of the glass.

The above may be applied to classifying in general term the tendency of a glass towards homogeneous or heterogeneous nucleation.

It has been demonstrated that stoichiometric glass forming systems can be separated into two groups:

1) In one system, crystallization proceeds in the volume supposedly by homogeneous nucleation. Their temperatures where maximum homogeneous nucleation rate (Tmax) occurs is close to the experimental glass transition temperatures,Tg.
2) The opposite behavior is observed for the other types of glasses, which only crystallize heterogeneously on the surfaces, i.e., the calculated temperature of

maximum homogeneous nucleation rate is substantially lower than Tg (Tmax << Tg).

Thus, for this second family of glasses, the induction periods in the temperature range where nucleation could in principle be detected are too long. Thus their rates can be undetectably low. The critical cluster size and the energy needed for a critical cluster formation decreases with the difference Tm − T. For this reason, when the glass transition range is reached at relatively high temperatures Tgr > 0.60, this energy is still too large to allow measurable internal crystallization. However, close to or on interfaces, the energetic barrier for nucleation and the viscosity may be lower than bulk values. Therefore, surface crystallization is more commonly observed than internal crystallization. The transition from glasses demonstrating only surface crystallization Tgr > 0.60 to glasses showing volume nucleation Tgr < 0.58 may be qualitatively explained by an increase in nucleation rate with decreasing Tgr [26].

2.7 Classical Nucleation Theory

It is well known that on cooling a melt or reheating a glass, crystal nucleation can occur homogeneously or heterogeneously. The classical nucleation theory (CNT) for condensed systems, derived by Turnbull and Fischer [24] in the late 40s, is often used to understand and predict nucleation rates in under cooled melts. The subsequent step, crystal growth of internally distributed nuclei can lead to glass-ceramics. The requirement for bulk (or volume) crystallization is that the glass melt must consist of two liquid phases.

Overall crystallization occurs by a combination of nucleation and growth. The kinetics of such a process is usually described by a theory derived independently, in the late 1930s by Kolmogorov [25], Johnson and Mehl [27] and Avrami [28-30], hereafter denoted as the JMAK theory. If the assumptions on which the JMAK theory is based are not violated, the volume fraction transformed as a function of time, $\alpha(t)$, in isothermal conditions, is given by

$$\alpha(t)=1-\exp[-g_0\int^t(I(t')[_{t'}\int^t U(t)dt]^3dt'] \qquad (2.10)$$

Here g is a shape factor, which is equal to $4\pi/3$ for spherical crystals, and I and U are the crystal nucleation and growth rate, respectively. This equation has two limiting forms. For constant crystal nucleation and growth rates throughout the transformation (homogeneous nucleation), equation (a) can be expressed by

$$\alpha = 1- \exp [gIU^3t^4/4] \qquad (2.11)$$

If the induction periods for nucleation, t_{ind}, are significant, then, to a first approximation, t should be replaced by $(t - t_{ind})$ in the above equations. On the other hand, if the number of growing crystals does not change, e.g., all nucleation centers are exhausted at an early stage of transformation due to fast heterogeneous nucleation, crystal growth occurs from a fixed number of sites and the limiting value of equation (2.11) is then

$$\alpha=1-\exp[-gNU^3t^3] \qquad (2.12)$$

N is the number of sites per unit volume.

Avrami proposed that for three-dimensional nucleation and growth processes, the following general relation should be used:

$$\alpha=1-\exp[-Kt^m], \quad 3\leq m \leq 4 \qquad (2.13)$$

This expression covers all cases where I is a function of time, up to the limit when I is constant. It also covers the case of heterogeneous nucleation from a constant number of sites, which are activated at a constant rate till becoming depleted at some intermediate stage of the transformation. Equation (2.13) is usually linearized and takes the following form [31]:

$$ln(-ln(1-\alpha)))=lnK+m\,ln\,t \qquad (2.14)$$

Therefore, the Avrami coefficient, 'm', can be calculated from the slope of the plot of $-ln[-ln(1-\alpha)]$ against $ln(t)$. The linearity of such a plot is taken as an indication of the validity of the JMAK equation for the case under study. When homogeneous nucleation is the operative mechanism, one can also use the y-axis intercept of such plot, $ln(K)$, to compute the crystal nucleation rates, i.e,. $I = 3K/\pi U^3$.

Equation (2.12) will be used to infer the crystallization mechanism and to estimate the nucleation rates [31].

2.8 Glass transition and crystallization kinetics using Differential Thermal Analysis(DTA)

The theoretical basis for interpreting DTA results is provided by the formal theory of transformation kinetics as developed by Johnson and Mehl [27] and Avrami [28-30]. This theory describes the evolution with time, t, of the volume fraction crystallized, χ, in terms of the crystal growth rate μ [32]:

$$\chi = 1\text{-}\exp[-gN_0(\int^t U(t')dt')^m] \qquad (2.15)$$

where N_0 is the number of pre-existing nuclei per unit volume, and m is an exponent, which depends on the dimensionality of the crystal growth. In the c case where ‘‘site saturation’’ is observed [33], the kinetic exponent is n = m.

By assuming an Arrhenian temperature dependence for $\mu = \mu_0 e^{E/RT'}$ and a heating rate, $\beta=dT/dt$, substituting $y'=E/RT'$ into the integral becomes an alternating series [34]. Consequently considering that in this type of series the error produced is less than the first term neglected and bearing in mind that in most crystallization reactions $y'=E/RT' >>1$ (usually $E=RT'\geq 25$), it is possible to use only the first term of this series, without making any appreciable error, and the above-mentioned integral becomes

$$I=e^{-y}y^{-2}=RT^2E^{-1}\exp^{(-E/RT)} \qquad (2.16)$$

with another assumption that $T_0 = T$ (T_0 is the initial temperature), so that y_0 can be taken

as infinity. This assumption is justifiable for any thermal treatment that begins at a temperature where crystal growth is negligible, i.e. below the glass transition temperature, Tg [35].

Substituting Eq. (2.15) into Eq. (2.16), the volume fraction crystallized in a non-isothermal process is expressed as

$$\chi=1-\exp[-Q(K_r T^2 \beta^{-1})^n] \qquad (2.17)$$

where $Q = gN_0(R/E)^n$ and K_r is the reaction rate constant. It should be noted that Eq. (2.17) is a general expression for all values of the parameter n, which, as it is well known, in the case of ‘‘site saturation’’ depends on the mechanism of the crystal growth.

With the aim of calculating the kinetic parameters, the crystallization rate can be obtained by derivating Eq. (2.17) with respect to time, where it has been assumed that the reaction rate constant is a time function through its Arrhenian temperature dependence.

The maximum crystallization rate is found by making $d^2x/dt^2 = 0$ with the assumption in the above-mentioned hypothesis that E=RT>>1, and subsequently the logarithmic form is written as

$$\ln(T^2_p/\alpha)=E/RT_P - \ln q=0 \qquad (2.18)$$

which is an equation of a straight line, whose slope and intercept give the activation energy, E, and the pre-exponential factor, $q = Q^{1/n} K_{R0}$, respectively.

It is suggested that Eq. (2.18) is valid also for the glass transition according to Kissinger’s

formula [36], which has often been used to calculate the activation energy of transition Ec and given by

$$\ln(T^2_g/\alpha)=Ec/RTg + \text{constant} \quad (2.19)$$

In the non-isothermal crystallization, the volume fraction of crystallites, χ, precipitated in a glass heated at constant rate, α, is related to the crystallization activation energy, Ec, through the following expression

$$\ln[-\ln(1-\chi)]=-n \ln \alpha - 1.052(mE/RT) + \text{constant} \quad (2.20)$$

where m and n are integers or half-integers which depend on the mechanism of the growth and the dimensionality of the crystal [32]. Besides, from the mean value of the kinetic exponent, n, it is possible to postulate a crystallization reaction mechanism for different silicate glasses [38].

2.9 Spectroscopic Studies in Cr-doped glasses and glass-ceramics

Optical spectra of 3d ions in crystalline solids exhibit broad bands associated with vibrational interactions. These broad emission bands provide an opportunity for making tunable lasers. Particular advantages of chromium as a laser ion over other transition metal ions are its chemical stability, existence of broad pump bands, large energy level splitting, and reduced excited state absorption. These advantages have led to more than a dozen crystals demonstrated as laser hosts for Cr [38].

The four-level laser scheme is depicted in figure (2.6). As in the three-level laser, the excitation energy pumps electrons from the ground state to a short-lived highly excited level E_4. The atoms then drop quickly to a metastable upper laser level E_3. The laser transition then takes these atoms to a lower level E_2, rather than all the way down to the ground state. After they have dropped to level E_2, the atoms lose the rest of the excess energy by spontaneous emission or other processes, and finally fall to the ground state [39].

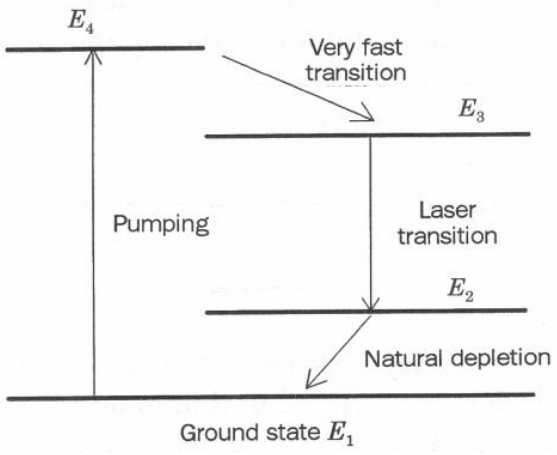

Fig.2.6 Energy level diagram of a four-level laser [39].

The Cr^{4+} emission belongs to a transition between the $^3B_2$ ($^3T_2$) excited state and the $^3B_1$ ($^3A_2$) ground state, which is only magnetic-dipole allowed. $^3T_2$ and $^3A_2$ denote the energy levels in T_d symmetry (regular tetrahedron) and $^3B_2$ and $^3B_1$ denote the energy levels in D_{2d} symmetry (distorted tetrahedron). In Ca_2GeO_4, Cr^{4+} in the ($3d^2$) configuration is in tetrahedral ("oxo") coordination with a $^3A_2$ ground state, a $^3T_2$ emitting state, and the higher excited spin triplet states $^3T_2$(F) and $^3T_2$(P). However, the tetrahedron is distorted and the true site symmetry is C_s. This leads to orbital splitting of the T state in T_d symmetry. A detailed assignment of the ground state absorption (GSA) spectrum of Cr (IV) doped Ca_2GeO_4 was given by M. F. Hazenkamp et al. [40-41]

Tanabe and Sugano [42], Fig. A.3, presented a series of energy level diagrams for $3d^n$ ions in octahedral coordination showing energy levels of an ion as a function of crystal field parameter Dq and the Racah parameters B and C. The Tanabe-Sugano diagrams can be used for ions with tetrahedral coordination as well if we apply the rule: d^n (tetr)=d^{10-n} (oct), developed by MClure [43].

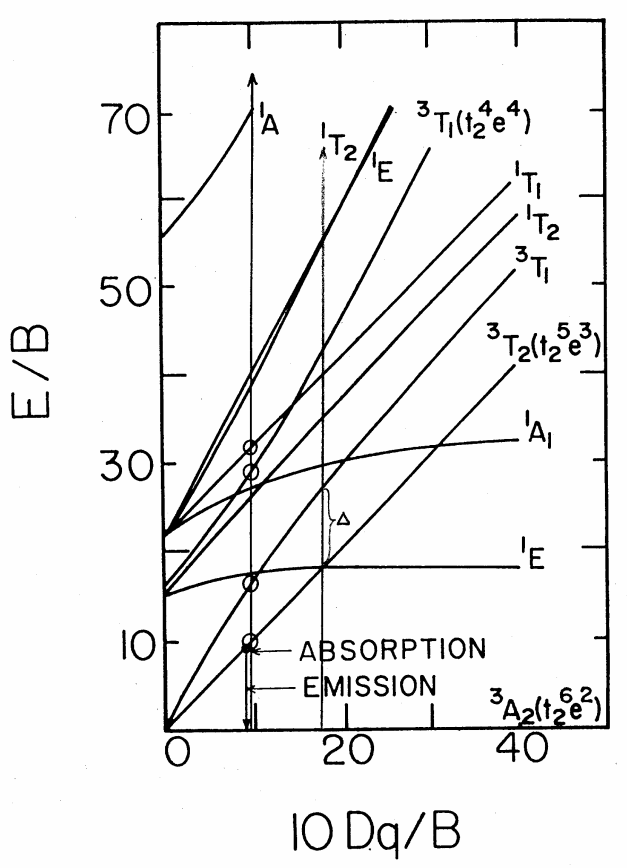

Figure 2.7: Tanabe-Sugano diagram for Cr^{4+} in tetrahedral coordination [44].

CHAPTER 3

EXPERIMENTAL TECHNIQUES

3.1 Materials synthesis

The fabrication of optical devices, for example tunable solid-state lasers, requires the use of flawless single crystals several centimeters long and of the order of 1 to 2 cm in diameter. Although the process is simple in principle, it is complex in detail and a variety of variables must be carefully controlled. Alternative routes require the use of glass-ceramics or porous glasses impregnated with optically active nano-scale crystallites or assemblies of quantum dots. The common feature of all of these routes is material synthesis and material characterization. Let us consider the development of tunable solid – state lasers. The following must be done:

- Prepare host materials and dope them with the laser active ion.
- Steady - state and time-resolved fluorescence measurement to determine the emission properties of the tentative materials.
- Determine the structure type of the materials, which meet the required emission properties.
- Determine phase diagrams and phase transitions. This is done to determine the necessary conditions for the growth of (nano-) crystalline photonic and laser materials.
- Prepare high quality materials.
- Determine the material properties, the knowledge of which is necessary for the design and fabrication of working devices.

3.2 Differential thermal analysis

When using differential thermal analysis the sample-reference couple is heated or cooled at some constant rate and either the difference in temperatures (DTA-mode), Ts - Tr (ΔTsr) or the required differential thermal energy input, (DSC-mode), q, required to maintain constant rate of temperature rise of the sample-reference couple is monitored. The temperature difference is recorded either as a function of the sample temperature, or that of the reference temperature, or that of the furnace temperature, or as a function of time. An inert material such as α - Al_2O_3 is usually chosen as a reference material. The temperature difference is caused by the specific heat difference between the sample and the reference material. The heat capacity of α-alumina (Al_2O_3) is a smoothly and almost linearly varying function of temperature between 300 and 1900°K. If the sample undergoes some kind of a transformation, either physical or chemical, at a given temperature and the transformation is either endothermic or exothermic, then its heat capacity will change discontinuously at the transformation temperature [45]. Thus ΔTrs will also change discontinuously. Some phase transitions, reduction and dehydration reactions are endothermic. Meta-stable state to stable-state transitions, crystallization, oxidation and recombination reactions are exothermic. The differential technique makes it possible to accurately detect the difference between Ts and Tr and thus observe accurately the temperature where the event occurs. Fig.3.1 is a schematic representation of the experimental apparatus. The experimental equipment is controlled by a personal computer. The DTA software program controls the experimental module, collects and

stores data and can be used to analyze and display the experimental information. The size of the specimen needed for the experiments is of the order of six to thirty milligrams.

The instrument used is SDT 2960 Simultaneous DTA/TGA from TA Instruments. TGA denotes the fact that the instrument is also usable as a thermogravimetric analyzer. Fig. 3.2 shows a typical DTA curve for a Cr-doped Ca_2GeO_4-Li_2O-Al_2O_3-B_2O_3 glass ceramic. A glass transition is observed at 480 ^{0}C, followed by crystallization at 550 ^{0}C.

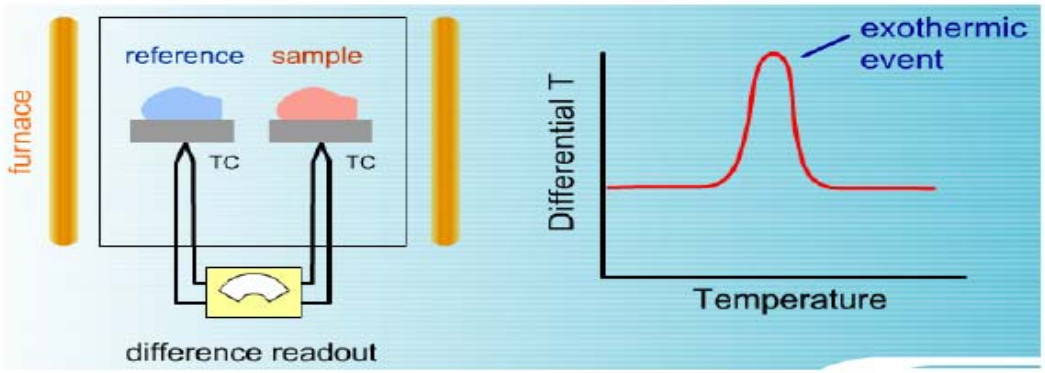

Fig.3.1: A schematic representation of the experimental apparatus.

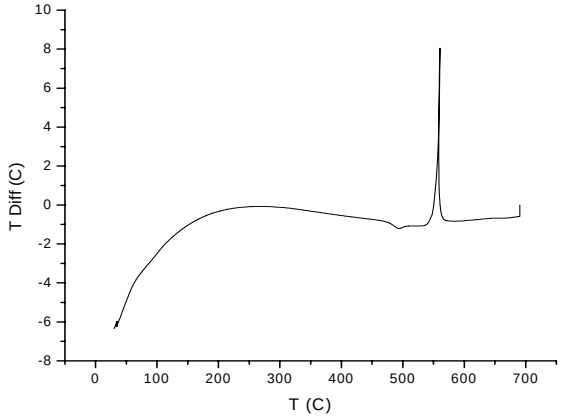

Fig.3.2: Typical DTA curve for a Cr-doped Ca_2GeO_4-Li_2O-Al_2O_3-B_2O_3 glass ceramic heat treated at 470 ^{0}C for 6 hours.

3.3 Fluorescence spectroscopy

To identify which of the synthesized materials possess the potential of being usable as a tunable solid-state laser, emission spectra are taken using 670-nm excitation to determine the fluorescence wavelengths and the fluorescence life times. A typical setup for a fluorescence experiment is shown in Fig. (3.3).

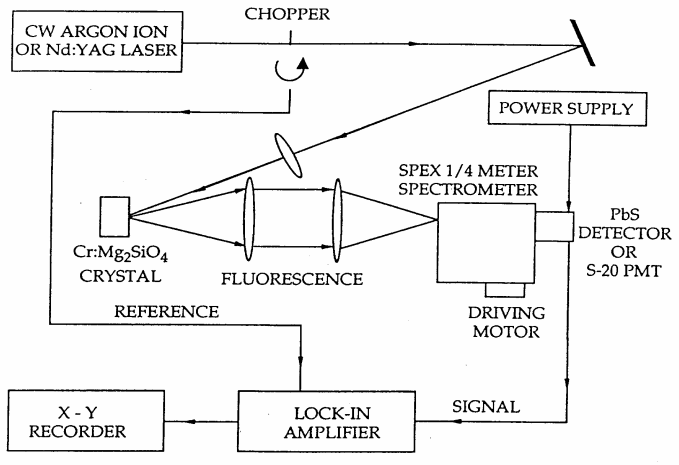

Figure 3.3: Schematic of fluorescence spectrometer [43].

For chromium doped materials the Cr^{4+} emissions are usually observed in the range 800-1800nm. The strength of the fluorescence determines if the material is suitable for laser purposes. Fig. 3.4 shows a typical curve for Cr-doped Mg_2GeO_4 powder sample prepared by solid state reaction.

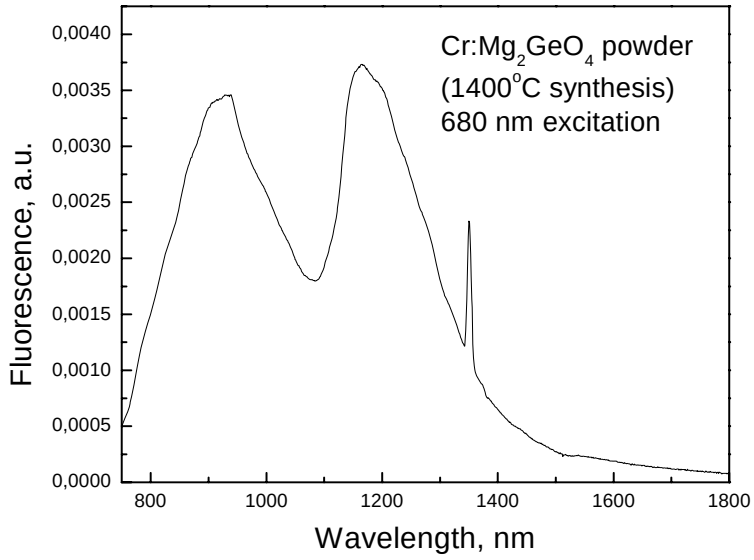

Fig. 3.4: Fluorescence of Cr-doped Mg_2GeO_4 powder sample prepared by solid state reaction.

3.4 Diffraction Analysis

A beam of monochromatic X-rays of known wavelength is required for XRD analysis. Striking a pure anode of a particular metal with high-energy electrons in a sealed vacuum tube generates X-rays that may be used for X-ray diffraction. By the right choice of metal anode and energy of accelerated electrons, a known wavelength (i.e., energy) or group of wavelengths will dominate the X-rays generated. Copper (Cu) X-ray tubes are most commonly used for X-ray diffraction of inorganic materials. The wavelength of the strongest Cu radiation (Kα) is approximately 1.54 angstroms (Å). Other anodes commonly used in X-ray generating tubes include Cr (Kα 2.29 Å), Fe (Kα 1.94 Å), Co

(Kα 1.79 Å), and Mo (Kα 0.71 Å).

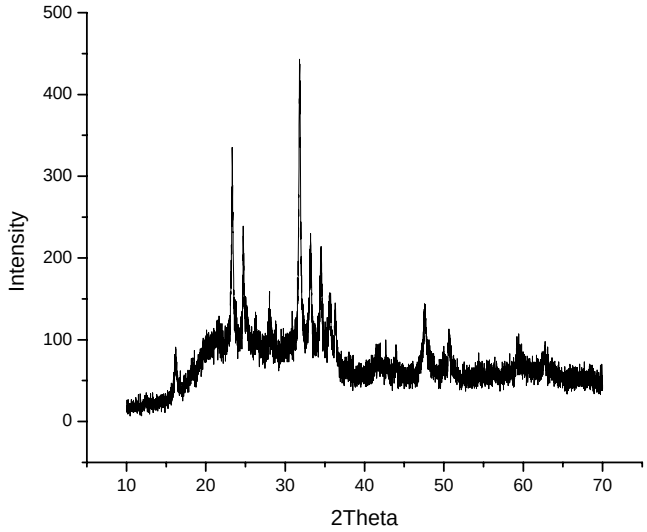

Fig.3.5: Example of an X-ray powder diffractogram produced during an X-ray scan for a glass ceramic sample heat treated at 520 ^{0}C for 1 hour.

The peaks in Fig.3.5 represent positions where the X-ray beam has been diffracted by the crystal lattice. The set of *d*-spacings (the distance between adjacent planes of atoms), which represent the unique "fingerprint" of the mineral, can easily be calculated from the 2-theta values shown. The use of degrees 2-theta in depicting X-ray powder diffraction scans is a matter of convention and can easily be related back to the geometry of the instrument. The angle and the *d*-spacings are related by Bragg's Law.

3.5 Scanning Electron Microscopy (SEM)

The number and size of the crystallites are usually measured using scanning electron microscopy (SEM). The Zeiss DSM 940 thermionic SEM with a resolution of 5 nm at 30 kV was used for imaging. It is designed for lower magnifications (100x to 20kx) and it is equipped with an X-ray detector for EDS. The Zeiss Supra 55 VP which is a field emission SEM with a maximum resolution of 1 nm was also used for high resolution studies. It has the following capabilities: secondary and backscattered electron imaging in high vacuum or in variable pressure mode, low voltage scanning transmission electron microscopy (STEM), electron beam lithography, energy dispersive x-ray spectrometry (EDS) and electron backscatter diffraction (EBSD).

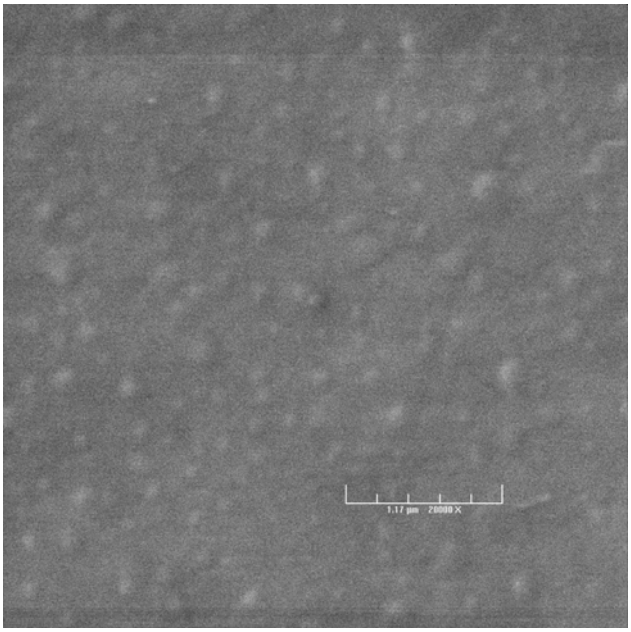

Fig. 3.6: A typical image of Cr-doped Ca_2GeO_4-Li_2O-Al_2O_3-B_2O_3 glass ceramic using the Zeiss DSM 940 thermionic SEM. The bar on bottom is 1.17µm at 20,000 resolution.

3.6 Confocal Microscopy

Confocal microscopy is an optical imaging technique used to increase micrograph contrast and/or to reconstruct three-dimensional images by using a spatial pinhole to eliminate out-of-focus light or flare in specimens that are thicker than the focal plane[46]. In a conventional (i.e., wide-field) fluorescence microscope, the entire specimen is flooded in light from a light source. Due to the conservation of light intensity transportation, all parts of the specimen throughout the optical path will be excited and the fluorescence detected by a photodetector or a camera. In contrast, a confocal microscope uses point illumination and a pinhole in an optically conjugate plane in front of the detector to eliminate out-of-focus information. Using the Confocal Raman Microscope *alpha300 R*, chemical properties of solid and liquid components can be analyzed with diffraction limited resolution (~200 nm). No labeling or other sample preparation techniques are necessary. The inherent depth resolution due to the confocal setup provides the ability to analyze the interior of transparent samples without microtome sectioning or freeze etching. A typical confocal image is shown in Figure 3.7.

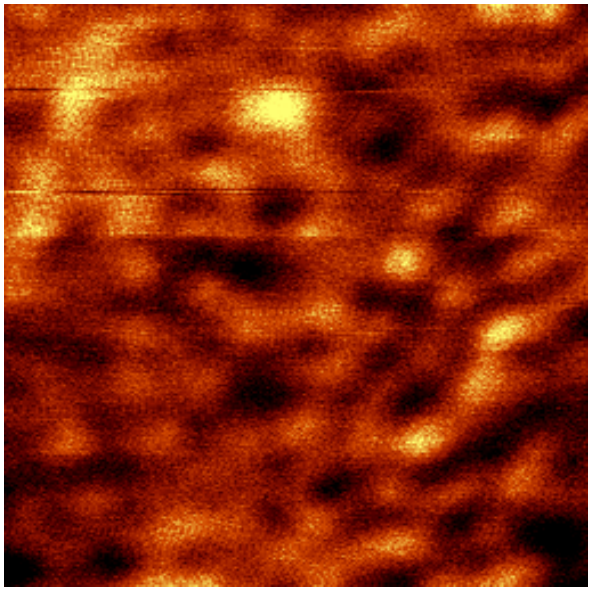

Fig. 3.7: A typical confocal image of Europium doped Ca_2GeO_4-Li_2O-Al_2O_3-B_2O_3 glass ceramic heat-treated at 500 ^{0}C for 24 hrs. The image is 5x6 µm.

3.7 Porosity and Surface Area Analysis

Surface area and porosity are important physical properties that influence the quality and utility of many materials and products. Therefore it is critically important that these characteristics be accurately determined and controlled. Likewise, knowledge of surface area and especially porosity often is an important key in understanding the formation, structure, and potential application of many natural materials. Micromeritics' Gemini V series of surface area analyzers was used in determining the size of the pores in mesoporous MCM-48 and HMS glasses. The knowledge of pore size distribution was a key factor in impregnation experiments of Cr-doped calcium germanate nano-crystals. A Schematic of a Micromeritics' Gemini V series of surface area analyzer is shown in Figure 3.8.

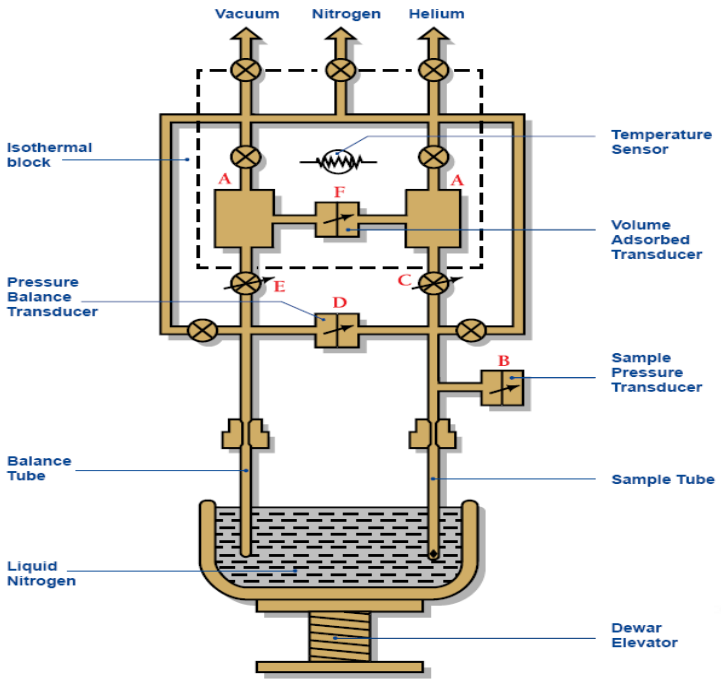

Fig. 3.8: Schematic of a Micromeritics' Gemini V series of surface area analyzer [47].

The Gemini has, as illustrated in Figure 3.8, two gas reservoirs (A) which are filled with equal volumes of the desired adsorptive, usually nitrogen. From the reservoirs, gas is dosed into the sample and balance tubes. A transducer (B) on the sample side monitors for the target pressure. As the sample adsorbs gas, the pressure would tend to decrease in the sample tube were it not that transducer (B) causes a fast response servo valve (C) to hold the pressure constant. Transducer (D) located between the sample and balance tubes detects any pressure difference between the two tubes and causes another servo valve (E) to balance the pressures in both tubes. A third pressure transducer (F) monitors the pressure between the two reservoirs to determine the amount of gas that is adsorbed on the sample. This method of dosing and accounting for the volume of gas uptake enables the Gemini to produce highly accurate, highly reproducible results in the minimum time [47].

CHAPTER 4

SYNTHESIS OF NANO-CRYSTALS AND POROUS GLASSES

4.1 Synthesis of nano-crystals.

4.1.1. Sol-gel method.

Cr-doped calcium germanate gels were prepared by room-temperature acid hydrolysis of a 2:1 mixture of $Ca(OOCCH_3)_2$ (calcium acetate) and $Ge(OCH_3)_4$ (tetramethoxy germanium). Ten milliliters of $Ge(OCH_3)_4$ (0.038 mol) in 5 ml of methanol was mixed with 10 ml of a 2:1 mixture of water and methanol containing 13.390 g of calcium acetate. The mixture was stirred for 30 min in an ice bath and 5 ml of methanol containing a weight of $CrCl_3x6H_2O$ corresponding to Cr/Ge ratios ranging from 0.01 to 1 was added followed by 0.5 ml of 1 M HCl. The resulting green solution was stirred for 2.5 hrs in an ice bath and then transferred to a glass container, covered, and allowed to gel at room temperature, 22^{o}C. A transparent greenish gel was formed within 24 h. After drying and aging for two weeks at room temperature, all xerogels were further dried by CO_2 supercritical extraction. The dried extracted gels, which were highly transparent but quite brittle, were calcined for 6 hrs at different temperatures up to 1000^{o}C. All samples were heated at a rate of 1^{o}C/min in a Thermoline 48000 programmable furnace.

Fig. 4.1 shows X-ray spectra of the sol-gel powder heat-treated at different temperatures. A typical spectrum for a crystal phase appears at 500 ^{0}C. It was shown that Ca_2GeO_4 nanocrystals ~80 nm in size can be obtained at unexpectedly low temperature (550^{o}C). Low temperature synthesis is critically important for the fabrication of small size particles. The spectroscopy of particles separated by size shows no difference in optical behavior for the sizes ranging from 80-1000 nm. Fig. 4.2 shows spectra of fluorescence of these samples. In full agreement with X-ray data, typical for the Cr^{4+}:Ca_2GeO_4 crystals' a fluorescence band centered at 1280nm appears at 500-550 ^{0}C. Fig. 4.3 shows AFM image of the powder, indicating a size of particles is as low as ~80nm. Fig.4.4. shows scattering of the He-Ne laser beam in the sol-gel powder suspended in methanol solution. The dependence of scattering on wavelength will be used for estimation of particle size in our future experiments.

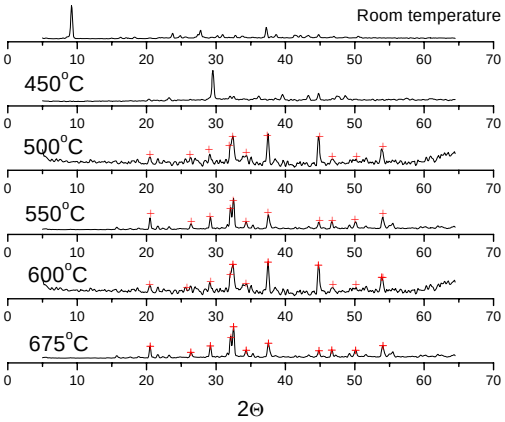

Fig. 4.1. X-ray data on low-temperature sol-gel synthesis of Ca_2GeO_4 nanopowder.

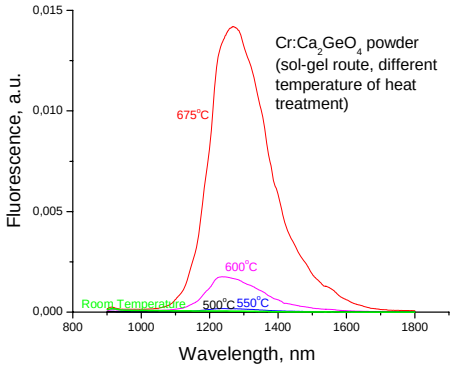

Fig. 4.2. Fluorescence spectra taken from glass-ceramics after heat treatment at 500, 550, 600 and 675 ^{o}C.

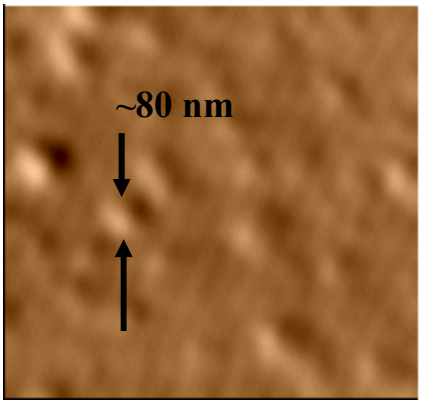

Fig.4.3 AFM image of Sol-Gel powder after heat treatment at 550 ^{o}C.

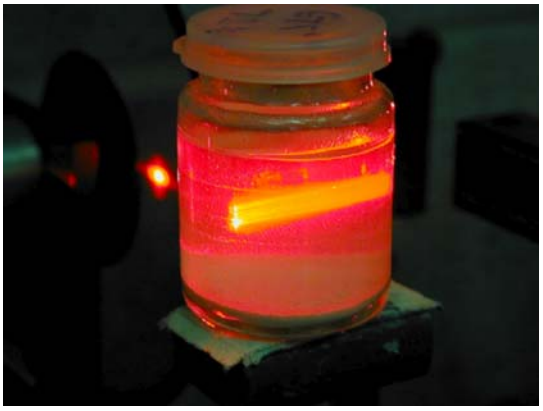

Fig.4.4. Light scattering of Sol-gel Cr:Ca_2GeO_4 powder in methanol.

A nano-powder of Ca_2GeO_4 laser crystal has been prepared by the Sol-Gel method at unexpectedly low temperature of T=550 ^{0}C. This leads to formation of crystallites of a size as low as 80 nm.

4.1.2 Precipitation method

The precipitation technique was used for preparation of Cr-doped Mg_2GeO_4 olivine nano-crystallites. The procedure was: 100 cm^3 of an aqueous solution of germanium acid containing 0.4308g. of germanium dioxide was treated with 25cm^3 of 1N magnesium sulfate solution and 15cm^3 of 2 N ammonium sulfate solution. Upon addition of 20cm^3 of ammonium hydroxide, a bulky white precipitate immediately formed. The mixture was raised to boiling, allowed to cool and to stand for

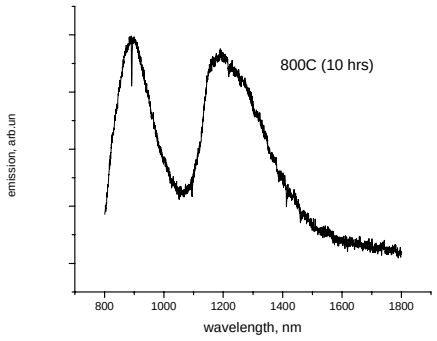

Fig. 4.5. Fluorescence of Cr:Mg_2GeO_4 powder

12 hours. The filtrate was collected and dried. After heat treatment at 800^{o}C for 10 hours the material was examined by X-ray diffraction and spectroscopic techniques. The particle size distribution was about 200- 800 nm.

Fig.4.5 shows the fluorescence spectrum of Cr:Mg_2GeO_4 fabricated by the precipitation method. There are 2 bands in the spectrum: i) the band centered at ~900 nm belongs to the $^4T_2$-$^4A_2$ transition of trivalent chromium (Cr^{3+}); ii) the band at 1200 nm belongs to $^3T_2$-$^3A_2$ transition of tetravalent chromium (Cr^{4+}). Unfortunately, the size of crystallites formed during precipitation was 10 – 100 □m.

The rather large size of the particles is due to the non-optimized initial chemical composition. More research is needed to fabricate smaller particles with uniform size distribution.

4.2 Porous glass synthesis

4.2.1. Synthesis of Hollow Mesoporous Spheres (HMS)

10.20 ml tetrapropylammonium hydroxide (TPAOH, 17.39% in water (89.0%) and 0.93 NaOH were mixed in 45 ml H_2O and 3.391 g $Al_2(SO_4)3x18H_2O$ and 11.2 ml tetraethylorthosilicate (TEOS) were mixed in 47 ml H_2O with stirring for 20 min; then the two solutions were mixed with each other. To control the hydrolysis process of TEOS, the temperature was kept under 20^{o}C by putting the beaker with a magnetic stirrer in ice bath. The resulting solution was stirred for 4 h and aged for 8 days. The sample

was heated for 10 min at 60^{o}C, after aging.

3 ml of prepared sample was centrifuged for 25 mins and kept in the test tubes for 24 hrs at room temp to let the water be evaporated completely from the gel. DTA was done after that. No phase transition/gel formation was observed thermally at 140 ^{0}C at atmospheric pressure.

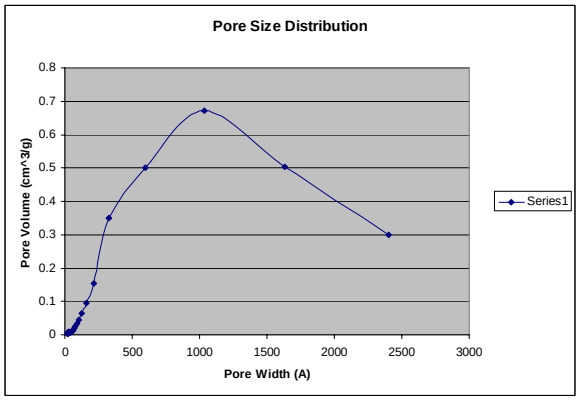

Fig.4.6. Pore size distribution

The samples then were autoclaved at 135^{o}C for 78 hrs at the applied vapor pressure of 2.5 atm. A gel was formed. After that they were put into a vacuum oven at 60^{o}C followed by calcination at 550 ^{o}C. Dark carbon like material was formed with a wide pore distribution exhibiting a maximum at ~100 nm (Fig. 4.6).

4.2.2. Synthesis of cubic mesoporous MCM-48

0.1 wt% solution of cetyltrimethylammonium bromide in H_2O (CTAB) was prepared first and 90 mL of this solution was stirred for one hr at 30-65 ^{0}C. 10mL of silicon tetraethoxide (TEOS) was mixed with 9mL of distilled water and 90mg of NaOH in a separate beaker. Both solutions were mixed and stirred for 30 min at 30^{o}C. Molar

composition of the synthesis mixture was TEOS:CTAB:H_2O=1:0.55:112. The whole solution was put in the Teflon bottle for 120 hr at 373K with the purpose to initiate solidification under static hyrdrothermal conditions. Then the material was calcined at 823K (550^oC) in flowing nitrogen. Nitrogen flow was continued for 15 hrs. Then the nitrogen flow was switched to oxygen and the sample was calcined in oxygen for 2 hrs. Fig. 4.7 shows the microscope image of a porous glass obtained. This glass will be used as a matrix for nanosize crystallites.

The DTA and TG curves of the resulting material are shown in Fig. 8. DTA was done on SDT 2960 Simultaneous DSC-TGA by TG Instruments. Fig. 4.8 shows a weight curve (TG) (green curve) and the differential temperature (DTA, blue curve) curve as a function of temperature. No change occurs up to 600 ^0C indicating that the calcination process is completed and there is no residual organic material.

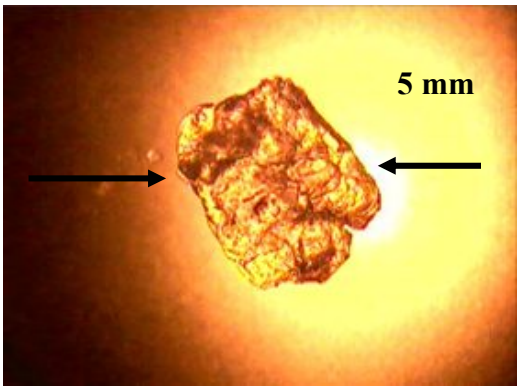

Fig.4.7 MCM-48 mesoporous glass

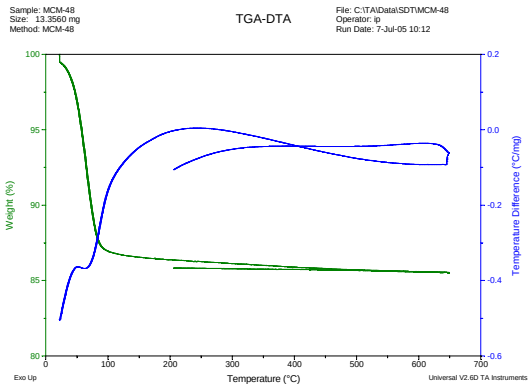

Fig. 4.8. DTA analysis of mesoporous glass

4.2.3 Porosity analysis

Porosity measurement was carried out in Micromeritics Gemini V surface area and pore size analyzer system. 0.157 g of the calcined sample was degassed in vacuum for 20 min at room temp and for 2 hr at 200^{o}C with low flow to nitrogen. After degassing the sample weighting ~ 0.100 g was placed in the Micromeritics Gemini V analyzer to take measurements. The pore measurement results are shown in Fig. 4.9. The pores are mainly in the 20 nm range. To achieve further reduction of the size down to 10nm, the preparations conditions will have to be improved. The pH is known to be a major factor defining pore size distribution in MCM-48 mesoporous glasses, therefore the variation of pore sizes is expected to be achieved by changing pH of initial composites.

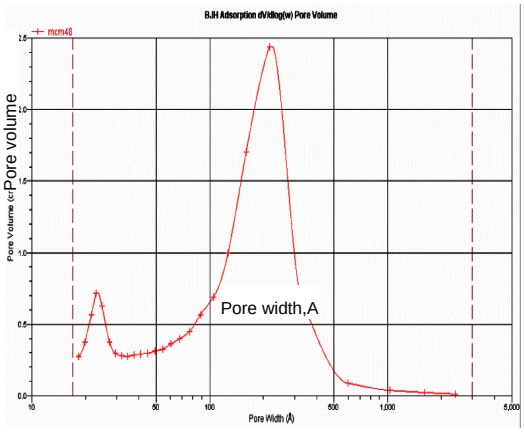

Fig.4.9 Pore volume distribution. The size of the pores is in the 20 nm range.

Outcome: Cubic mesoporous glasses MCM-48 were synthesized with the porous size of ~20nm.

4.3 Study of impregnation processes

4.3.1. Ethanol solutions

Difficulties in preparation of porous glasses with narrow pore size distribution forced us to look at commercially available materials. Further experiments on glass impregnation were carried out using Vycor porous glasses produced by Corning Inc. These type of glasses exhibited ~ 5 nm pore sizes, with less than 10% variation, in the size distribution. To test the possibility of impregnating these glasses by ethanol solutions, and to estimate the porosity (volume of pores / volume of glass) of the material, experiments were done by immersing a glass sample in pure ethanol, and determining the weight of pore absorbed ethanol.

Alcohol incorporated in glass (after 2 hours of immersion) = 0.0479 g

Density of alcohol = 0.785g/cm^3

Volume of alcohol in the pores (volume of pores) ~60 mm^3

Volume of glass sample = 227.5 mm^3

Porosity = Volume of pores/ Volume of glass ~ 0.25 (25%)

4.3.2. Cr:Ca2GeO4 sol solutions

A series of experiments were carried out with Cr: Ca_2GeO_4 sol. The porous glass was immersed in ethanol solution of an appropriate stoichiometric amount of germanium in the form of germanium tetraethoxide (Ge $(OC_2H_5)_4$ or TEOG) and calcium in the form of calcium nitrate (Ca $(NO_3)_2$).

The first step of these experiments was to make a sol of Ca_2GeO_4. Ethanol solutions of calcium nitrate, and germanium tetraethoxide, were prepared. Calcium nitrate was prepared from Ca $(NO_3)_2$ x $4H_2O$ by dehydration at 250^oC, for a few hours, on a hot plate. Both, Ge $(OC_2H_5)_4$ and Ca $(NO_3)_2$, are very moisture sensitive and vigorously react with water. For this reason the solutions were prepared and kept under nitrogen atmosphere to ensure the absence of moisture. The solution compositions were: 1) 3.28g (0.02 mol) Ca $(NO_3)_2$ + 5.52g (0.12 mol) C_2H_5OH, and 2) 5.1g (0.02 mol) TEOG + 7.95g (0.17 mol) C_2H_5OH. The mixtures were stirred for two hours. 2-5 wt% of $CrCl_3$ was also added to the Ca- mixture. After that the Ge-solution was placed in an ice bath, and the Ca-solution was added drop-wise at a slow rate to the Ge-solution to prevent formation of amorphous flakes during mixing. This step was performed at low temperature to avoid possible gel formation.

Gelation is the result of hydrolysis and condensation reactions according to the following equations:

$$\text{-Ge-OEt} + \text{H-OH} \rightarrow \text{-Ge-OH} + \text{H-OEt (hydrolysis)} \quad (1)$$

$$\text{-Ge-OEt} + \text{HO-Ge-} \rightarrow \text{-Ge-O-Ge -} + \text{HOEt (dealcoholation)} \quad (2)$$

$$\text{-Ge-OH} + \text{HO-Ge} \rightarrow \text{-Ge-O-Ge} + \text{H-OH (dehydration)} \quad (3)$$

$$Ca^{2+} + NO_3^- + \text{-Ge-OH} \rightarrow \text{-GeO}^- + Ca^{2+} + HNO_3 \quad (4)$$

At room temperature the kinetics of the hydrolysis reaction (equation 1) is much faster than the kinetics of the condensation reactions (equations 2 and 3). The number of Ge-O-Ge bonds formed is not sufficient to give gelation and precipitation of the hydrated germanium oxide-alkoxide aggregate. Mixing at a lower temperature (0°C) allows: (a) control of the hydrolytic reactivity of TEOG so that soluble polymeric intermediates are obtained, which then undergo further polymerization to form a gel; and (b) the introduction of the modifier cation, Ca^{+2}, into the germanate network. These reactions lead to the formation Ca_2GeO_4 gel, but for our experiments, we have to suppress these reactions to keep the sol size and its viscosity as low as possible for successful impregnation of porous glasses.

Testing of the sol as a precursor of Cr-doped Ca_2GeO_4 was done by evaporation of a small amount of the sol on a hot plate at ~200^{o}C until a white powder was formed. This

white powder was heated in a muffle furnace to 650^{o}C and held at this temperature for 20 hours. As a result, a green powder was formed. The powder exhibited a broad band emission band typical for Cr^{4+}:Ca_2GeO_4 (Fig. 4.10).

A number of glass-impregnating experiments were carried out with this sol. None of the Vycor porous glasses used, showed any evidence of liquid penetration into the pores. The reason of this is that the size of the colloidal particles in the solution exceeded the size of the pores in the glass. A macro-porous SiO_2 glassy sample impregnated by Cr^{4+}:Ca_2GeO_4 sol, followed by heat-treatment at 650^{o}C for 20hr, turned to a green color (Fig. 4.11) and showed emission typical for Cr^{4+}:Ca_2GeO_4.

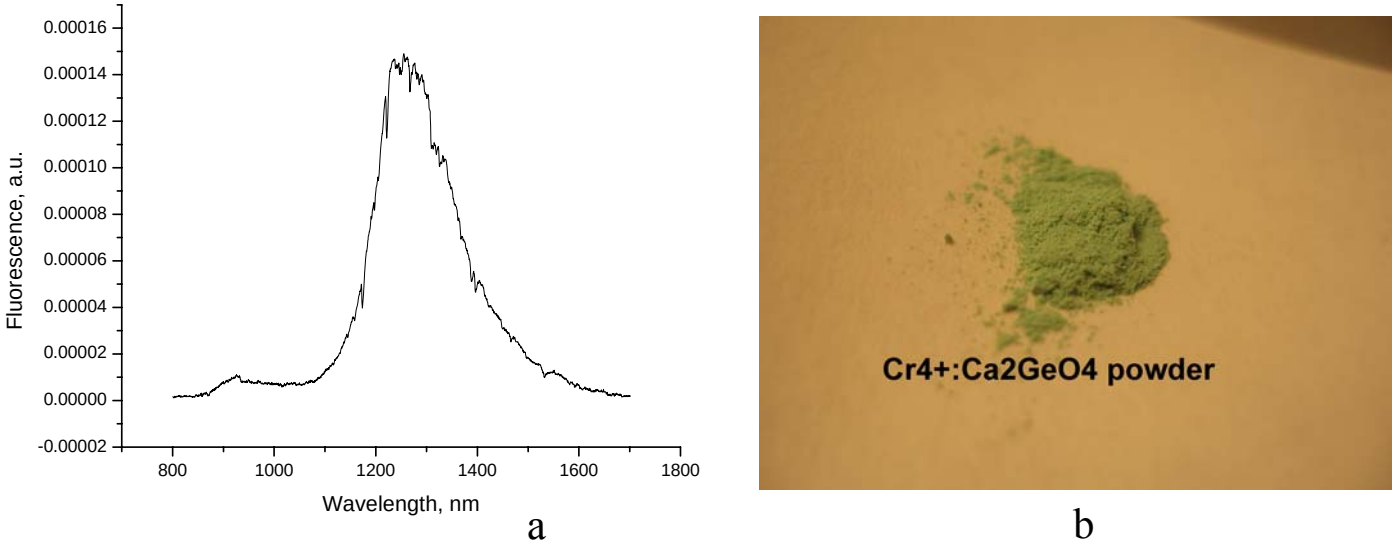

Figure. 4.10. Fluorescence spectra (a) of the powder (b) prepared from Cr-doped Ca_2GeO_4 sol

Figure 4.11. Macro-porous SiO_2 glassy sample impregnated by Cr^{4+}:Ca_2GeO_4 sol and subjected to heat-treatment (650^{o}C, 20hr). Green spot in the middle is due to Cr^{4+}:Ca_2GeO_4

To ensure penetration of Ca and Ge solutions into the nano-porous glass, we focused our efforts on preparation of Ca and Ge ethanol solutions separately without mixing them and studied the penetration behavior of each solution by separately immersing porous glass samples into one and then into the other solutions.

Two samples were immersed into the liquids at 70^{o}C (to lower viscosity) for one hour. Then they were rinsed in ethanol and dried at 200^{o}C on a hot plate. The Vycor glass sample immersed into the Ca-solution became green and opaque, but the sample immersed into the Ge-solution turned brown and transparent. Then both samples were put into a muffle furnace at 550^{o}C (1hr). After the heat treatment the Ca-sample became yellow, and the Ge-sample turned green. After putting these samples in the reversed solutions (Ca-immersed sample – into Ge-solution, and Ge-immersed sample – into Ca-solution for one hour at ~70^{o}C, both samples became greenish after removal from solution. Next step was drying of the samples on a hot plate at ~250^{o}C.

First heat treatment of the samples was at 700^{o}C for a period of ~ 20 hrs. Both samples

after this heat treatment exhibited Cr^{3+} type fluorescence. Heating to 800°C for two hours caused considerable increase in the intensity of emission (~2-3 times). Corresponding emission curves are presented below in Fig. 4.12.

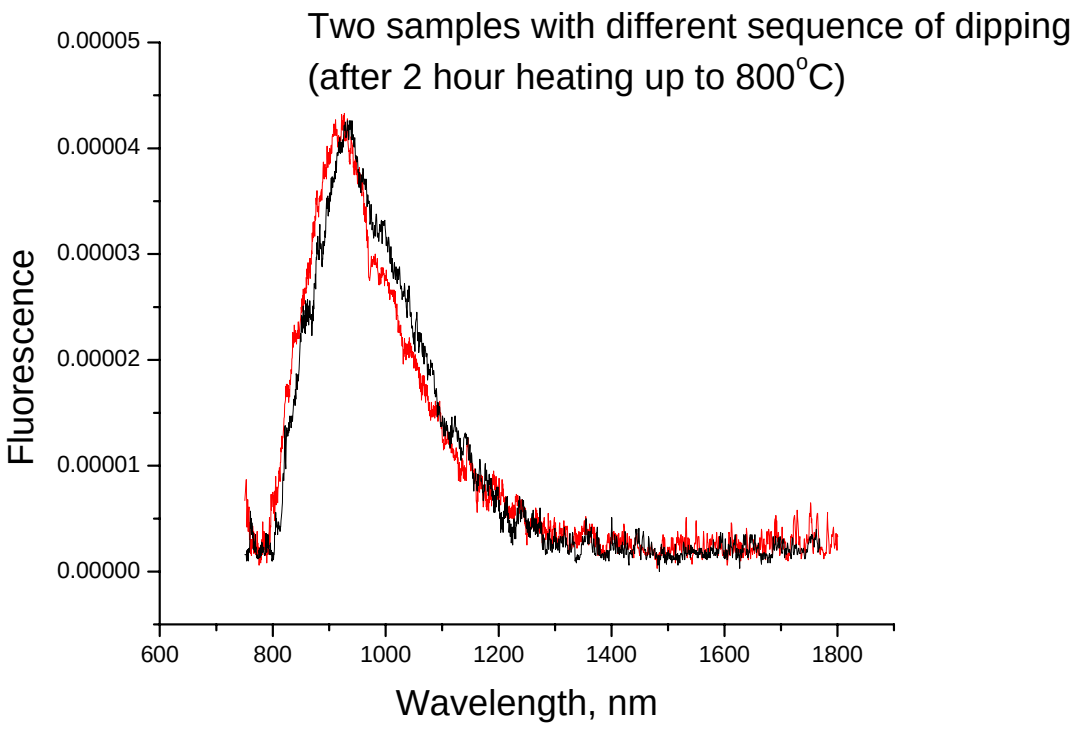

Figure 4.12: Fluorescence spectra of porous glass sample impregnated by Ca and Ge solutions with different sequence (black – first Ca-solution, red – first Ge-solution)

As can be seen from Fig. 4.12, both samples are characterized by broad band emission centered at ~ 900 nm. This type of broad band emission is usually assigned to emission due to $Cr^{3+,}$ occupying octahedral sites. Heat treatment of the glass samples at higher

temperature (~ 820^{o}C) led to devitrification (crystallite nucleation and growth) of the glass, thus the temperatures of impregnated porous glass heat treatments will not exceed 800^{o}C in future experiments.

Unfortunately, the emission spectra shown in Fig. 4.12 do not contain information about where Cr-ions reside in the host, i.e. in the crystallites or in the glass. Cr ions may be incorporated into the SiO_2-based glass host during heat treatment, or into Ca-Ge-O crystallites (but not of the olivine structure) formed in the glass pores during heat treatment.

Estimation of the quantity of a Ca solution infused into a porous glass is shown in Table 4.1. In this experiment we studied the infusion procedure by measuring the weight of a porous glass sample before and after immersing of the sample in $Ca(NO_3)_2$- ethanol solution, followed by drying at room temperature in nitrogen atmosphere, and on a hot plate in air atmosphere at ~250^{o}C.

Table 4.1. Impregnability of porous glass.

	Soak 1	Soak 2	Soak 3	Soak 4	Soak 5	Soak 6
Before soaking (gram)	0.338	0.3703	0.3785	0.3966	0.384	0.381
After soaking (gram)	0.408	0.3786	0.4095	0.4121	0.4134	0.4176
After drying in nitrogen flow (gram)	0.3698	0.378	0.3872	0.394	0.3933	-
After heating (gram)	0.3679				0.3793	0.3637
Vol. $Ca(NO_3)_2$ (mm^3)	13.47458	16.94915	20.84746	23.72881	17.5	10.88983
Percentage of pores filled %	0.224576	0.282486	0.347458	0.39548	0.2916667	0.181497

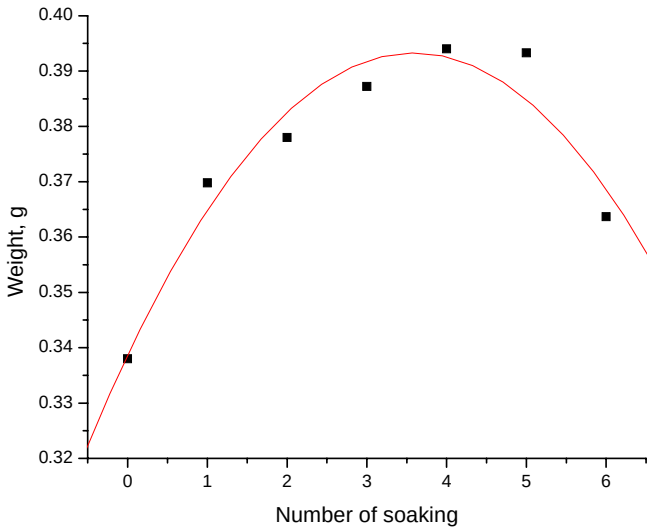

Figure 4.13. Weight change of the porous glass sample depending on the number of soaks

As can be seen from Table 4.1 and Fig. 4.13, the weight curve goes through a maximum that takes place after the fourth soaking. It is estimated that the portion of pores filled by $Ca(NO_3)_2$ ethanol solution was about ~40%. However, the maximum in Fig. 4.14 is probably connected with $Ca(NO_3)_2$ decomposition during drying. Evaporation of ethanol at that point was not completed. Partial release of NO_2 gas could also take place after drying in further soaking procedures (#5 and #6). The most important result of this soaking experiment is that after first soaking the sample became opaque (Fig. 4.14). The sample did not become transparent even after long term drying. An explanation of this may be connected with possible chemical reaction of the $Ca(NO_3)_2$-ethanol solution with the glass matrix. But, it is necessary to point out that soaking the glass sample in Ge-ethoxide solution left the sample transparent after drying.

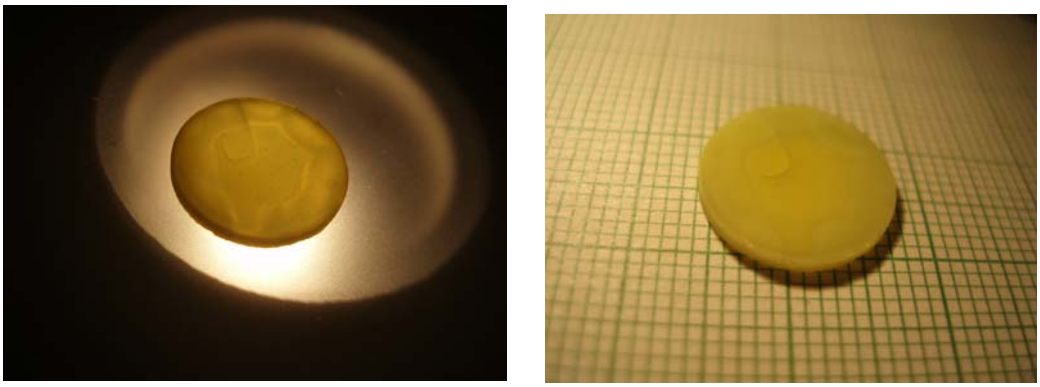

a **b**

Figure 4.14. Porous glass sample after soaking in $Ca(NO_3)_2$ ethanol solution (a – transmitted light, b – reflected light)

Final soaking of the sample was completed in Ge-ethoxide solution (Table 4.2). Considerable changes in the sample weight after soaking in Ge-ethoxide solution were only observed after immersion, because of adhesion of solution on the surface. After the drying procedure, the sample weight reverted nearly to its original value.

Table 4.2. Impregnability of porous glass by Ge-ethoxide

	Soak 7 (Ge)
Before soaking	0.3698 gram
After soaking	0.4304 gram
After nitrogen	-
After heating	0.3718 gram
Volume Germanium ethoxide	1.75 mm^3

Heat treatments of the sample were done at ~ 600°C, 700°C, and 800°C. The appearance of Cr^{3+} type emission was observed after first heating to 600°C (Fig. 4.15). After the heat treatment procedure the optical properties did not show considerable changes. The absorption curve of the porous glass sample is shown in Fig, 4.16. The absorption data showed a band centered at 650 nm that can be assigned to Cr^{3+} in octahedral occupation, and another very strong absorption band below 400 nm, that may be assigned to Cr^{6+} absorption.

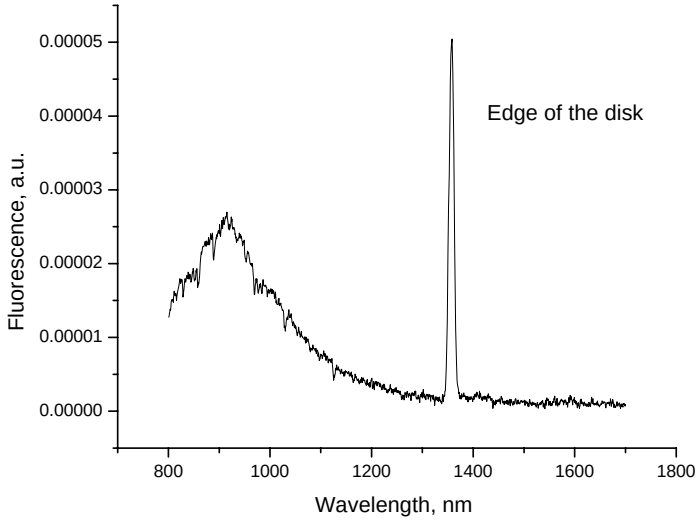

Figure 4.15. Emission of impregnated porous glass sample after heat treatment at 650°C (72 hr)
(680 nm excitation)

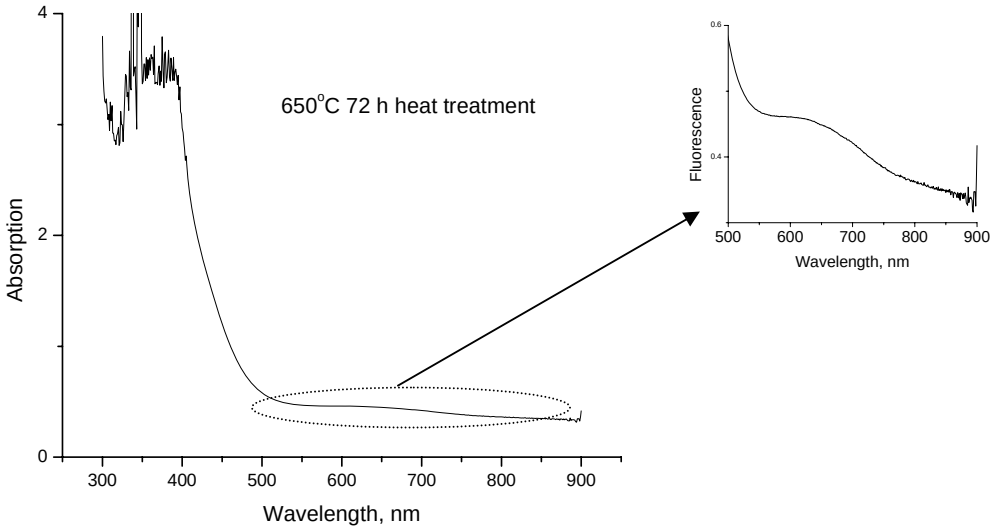

Figure 4.16. Absorption of impregnated porous glass sample after heat treatment at 650°C (72 hr)

CHAPTER 5

DEVELOPMENT OF Cr^{4+}-DOPED GLASS CERAMICS.

5.1. Synthesis of transparent nanocrystalline glass ceramics.

Nucleation and crystallization of glasses are topics of technological as well as scientific interest and importance. Crystallization must be avoided entirely in glasses used for certain practical applications. In other applications, (including Cr^{4+}-doped glass-ceramic materials) crystallization is desired, but it must be evoked in a controlled manner. Crystallization of laser olivines (Cr^{4+}:Mg_2SiO_4, Cr^{4+}:Ca_2GeO_4 and appropriate solid solutions) in glasses has never been considered, and only one publication is known to deal with Cr^{4+}:Mg_2SiO_4 glass ceramics [48], but there is no information about the composition and/or material preparation procedure in the publication. Therefore, the first key problem is to find the appropriate composition of glass for crystallization of Cr^{4+}:Ca_2GeO_4 during the after growth heat-treatment procedure.

Search for compositions providing acceptable glass forming ability and proper crystallization of Ca_2GeO_4 in glass media during after-growth heat treatment proved to be a very difficult. Obviously, the simplest solution could be a preparation of a stoichiometric Ca_2GeO_4 glass composition with a following ceramming (devitrification) process, but the numerous unfavorable thermodynamic properties of Ca_2GeO_4 (high melting point, polymorphism, vapor pressure) make this approach impossible. Using different additives for improving glass forming ability and lowering melting temperature

becomes inevitable. It is known [49-51] that the glass-forming ability in binary CaO-GeO_2 system takes place only for the GeO_2 enriched wing and is enhanced with increasing GeO_2 contents. However, to initiate crystallization of Ca_2GeO_4 in glassy media we supposedly should have the proper Ca/Ge ratio (>1) in the initial composition.

The search for glass-forming additives to Ca_2GeO_4 was carried out with the purpose to provide, on the one hand, an acceptable glass-forming ability of Ca_2GeO_4 –based mixtures, and, on the other hand, the crystallization of only Cr^{4+}-doped Ca_2GeO_4 micro/nano crystallites in glass media during devitrification. Boron oxide (B_2O_3) was chosen as the general glass-forming agent to be added to the CaO-GeO_2 system in the CaO enriched range. The first set of experiments was implemented for the ternary system Ca_2GeO_4-CaO-B_2O_3. To make glass samples, thoroughly mixed powder consisting on appropriate amounts of $CaCO_3$, GeO_2, B_2O_3, were melted in a platinum crucible in an electrically heated furnace in air atmosphere at 1350–1400 ^oC for 30 min followed by a quenching procedure (pouring into a copper mold or glassy-carbon boat). To avoid crack formation, after-quenching heat treatment (450^oC for 10 hours following slow cooling 20^oC/h to room temperature) was used. All compositions were activated by 0.5-1 wt.% Cr_2O_3 that allowed us to test the fluorescence properties of the parent (as quenched) glass as well as of the glass-ceramic samples after devitrification. Measuring fluorescence spectra is a very sensitive technique to detect presence of Cr^{4+}-doped crystallites in glass-ceramics. The broad band fluorescence spectrum of tetravalent chromium typically located in the wavelength range beyond 1 □m is easily revealed even at small amounts of crystallites in a sample.

5.2 $CaO-GeO_2-B_2O_3$ system

We determined the glass-forming region in a ternary system as an area of compositions where the material is still capable to be solidified in glass form under the given cooling conditions (cooling rate – pouring into a copper mold or glassy-carbon boat (2 cm^3 capacity) in the air atmosphere. Boron oxide considerably decreased the original melting point of Ca_2GeO_4 and created a good glass-forming ability of the melt in a wide temperature-concentration range. A number of glassy samples have been obtained using this quenching technique. The samples after quenching exhibited different properties. Some of them looked like pure glass without any evidence of crystallization occurring during the quenching procedure. Some samples looked like partially crystallized material. The compositions studied and the results of glass-forming region determined in the $CaO-GeO_2-B_2O_3$ system are shown in Table 1 and Fig 5.1. Devitrification of glass samples was carried out in the temperature range from 650-750^oC for different periods of time until full crystallization occurred. These experiments did not reveal any compositions providing volume crystallization of $Cr:Ca_2GeO_4$, but a small range of compositions exhibiting NIR fluorescence similar to Cr-doped Ca_2GeO_4 after devitrification was found (see Table 5.1, Fig. 5.2). Optical properties of Cr-doped $CaO-GeO_2-B_2O_3$ of as quenched glasses are characterized by lack of any emission or by low intensity emission from Cr^{3+} centers only, with a maximum at 900 nm. After the ceramming procedure, broadband fluorescence centered at 1300 nm appears in some glass-ceramic compositions similar to that of Cunyite single crystal (see Fig. 5.2), showing formation of Cr^{4+} centers. Cr-doped $CaO-GeO_2-B_2O_3$ glass samples before devitrification used for absorption and

fluorescence measurements are shown in Fig. 5.3. Unfortunately, only surface crystallization (hetero-nucleation) took place for those compositions.

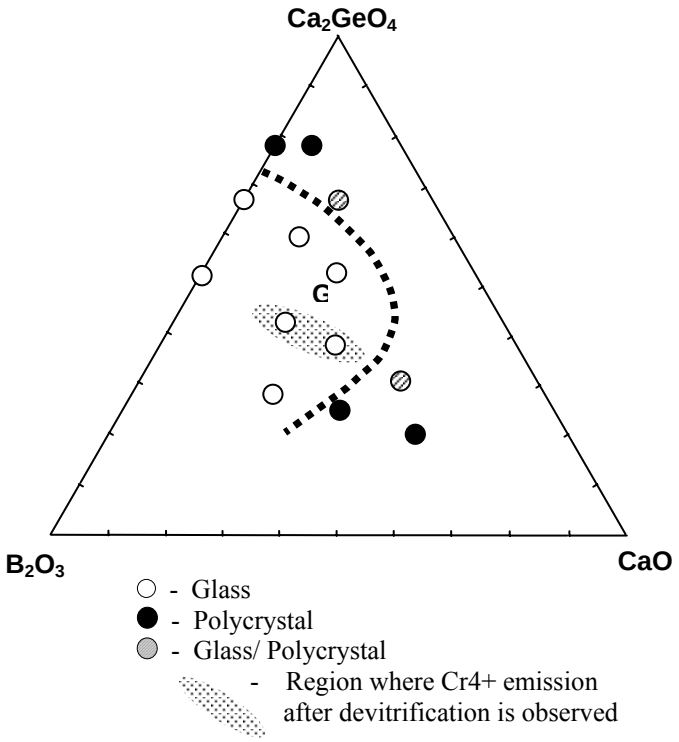

Fig. 5.1: Glass forming region in the Ca_2GeO_4-CaO-B_2O_3 system

Table 5.1. Glass compositions and their characterization in Ca_2GeO_4-CaO-B_2O_3 system

	Ca_2GeO_4 mol	CaO mol	B_2O_3 mol	Fluorescence maximum (nm)			Glass-forming ability
				Parent glass	As-grown crystals*	After devitrification	
1	1	0.25	0.5	900 nm weak	1240 nm weak	1240 nm weak	Good
2	1	0.5	1	900 nm weak	1240 nm weak	1240 nm	Good
3	1	4	2	-	900 nm strong	-	No glass
4	1	2	2	-	900 nm strong	-	No glass
5	1	1	2	900 nm strong	900 nm	920 nm	Good
6	1	0.5	0.5	900 nm weak	1240 nm	No emission	Good
7	1	0.25	0.25	900 nm weak	1240 nm	No emission	50%
8	1	1	1	900 nm weak	1240 nm and 920 nm	1240 nm strong	Good
9	1	2	1	None	1240 nm (needles) and 920 nm (opaque)	1240 nm and 920 nm both weak	50% (opaque stuff)
10	1	1	1+ 0.2 Al_2O_3	900 nm	None	920 nm (surface crystallization)	Good

* “as grown crystals” means crystallization while quenching procedure

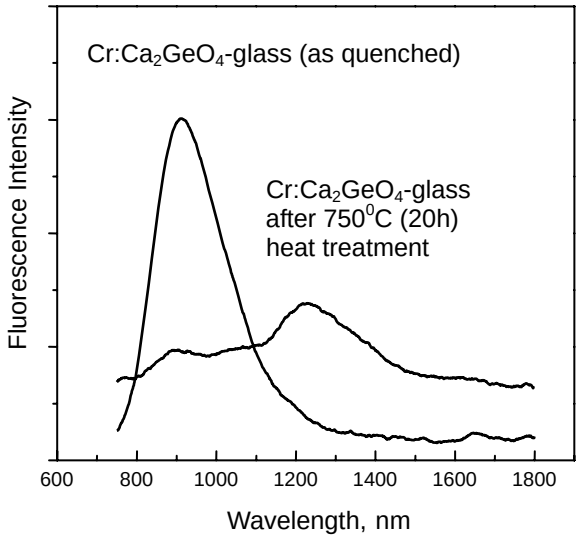

Fig. 5.2: Fluorescence spectra of Cr-doped $CaO\text{-}GeO_2\text{-}B_2O_3$ glass matrix and glass-ceramic after the devitrification (ceramming) procedure (750°C, 20 hours)

Fig. 5.3: Cr-doped $CaO\text{-}GeO_2\text{-}B_2O_3$ glass samples after cutting and polishing before devitrification (cramming) procedure

Optical microscope images of glass samples after devitrification where surface crystallization occurred are shown in Fig. 5.4-5.5. Scanning electron microscopic images of micro-nano-crystallites formed in surface vicinity of the glass sample during the devitrification procedure are shown in Fig. 5.6. The crystallites have a dendrite-like appearance and in accordance with powder X-ray diffraction measurements are identified as olivine-like Ca_2GeO_4. The broad band fluorescence spectrum (Fig. 5.2) is similar to bulk Cr-doped Ca_2GeO_4 crystals.

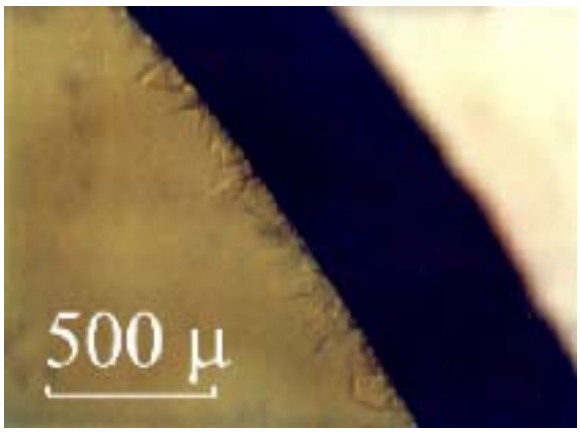

Fig. 5.4: Growth of Cr^{4+}:Ca_2GeO_4 crystallites (needle-like) on the surface of CaO-GeO_2-B_2O_3 glass sample.

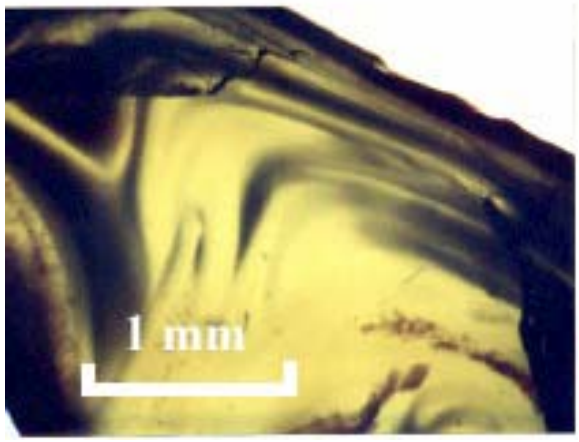

Fig. 5.5: Crystallization of Cr^{4+}:Ca_2GeO_4 in CaO-GeO_2-B_2O_3 glass sample on internal imperfections.

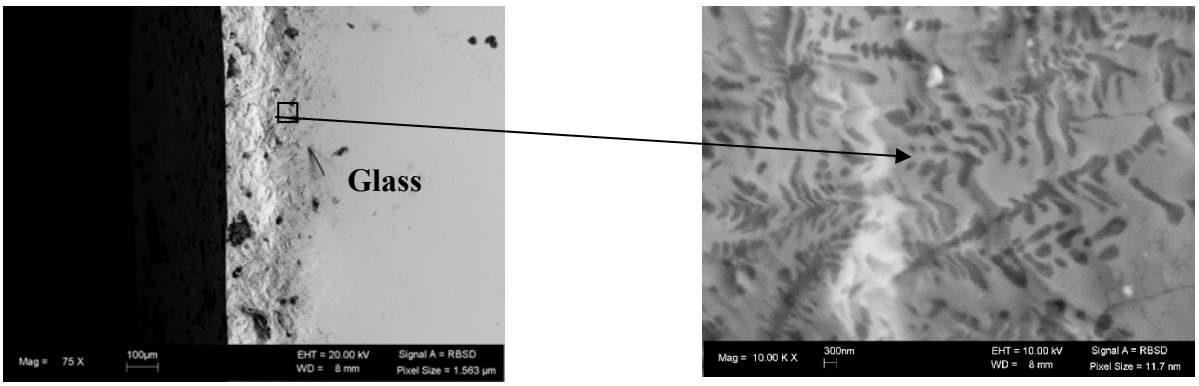

Fig. 5.6: Scanning electron-microscopic images of Cr^{4+}:Ca_2GeO_4 crystallization in the surface vicinity area of the glass samples.

Heterogeneous (surface) crystallization in CaO-GeO_2-B_2O_3 glass compositions was also confirmed by differential thermal analysis (DTA) measurements of bulk and powdered samples (Fig. 5.7). DTA experiments provide information on the glass-forming temperature range, temperature of nucleation and crystallization. The powdered sample is characterized by a sharp crystallization peak at lower temperature comparable with the

bulk sample, because of an increase in the total surface leading to massive increase in a number of crystal nuclei.

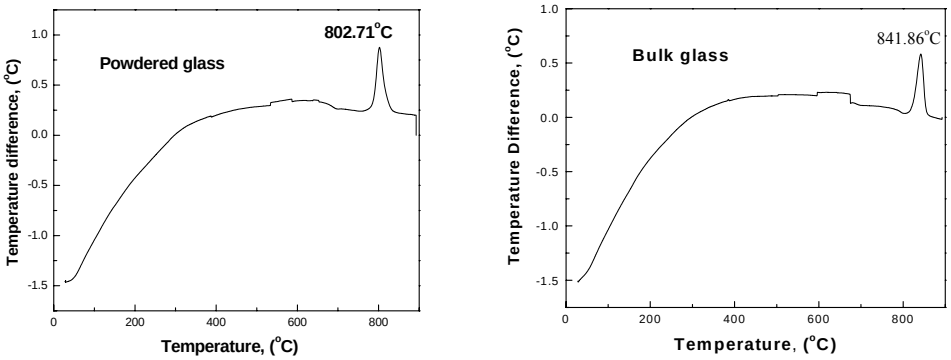

a b

Fig. 5.7: DTA curves for $CaO\text{-}GeO_2\text{-}B_2O_3$ glass samples (a – powdered sample, b – bulk sample,).

Heterogeneous crystallization does not provide homogeneous spacial distribution of crystallites in the glass media and formation of optically transparent glass-ceramics. Only homogeneous nucleation is acceptable for these purposes. Theoretical and experimental approaches to homo- and hetero-nucleation in glasses during devitrification are described in numerous publications [52-53]. Transfer from hetero- to homogeneous nucleation can be done by adding crystallizing agents to the glass composition or by modifying the initial glass composition by changing the alkali-acidic properties of the glass matrix causing proper change of solubility of components to be crystallized in the solid phase; in our glasses it is CaO and GeO_2. Such modification of $CaO\text{-}GeO_2\text{-}B_2O_3$ composition may lead to significant changes in the crystallization mechanism in glass-media to provide conditions for homogeneous volume (bulk) nucleation and crystallization.

Adding small amounts of different nucleation agents, such as P_2O_5, TiO_2, ZrO_2, PbF_2, Al_2O_3 to the initial glass composition did not provide significant changes in the devitrification mechanism, although some changes in the temperature range of the glass forming region and crystallization temperature were observed for those compositions. After these, the efforts were focused on search for appropriate modifiers for our CaO-GeO_2-B_2O_3 composition.

5.3 CaO-GeO_2-Li_2O_3-B_2O_3 system

After having tested numerous glass compositions, the glasses with the desired properties were discovered in the CaO-GeO_2-Li_2O_3-B_2O_3($A1_2O_3$) system[62]. The results on synthesis, devitrification behavior, and fluorescence properties of glasses and glass-ceramics are presented in Table 5.2. All compositions were doped with 0.5 - 1.0 wt.% Cr_2O_3. The experimentally determined glass-forming region in Ca_2GeO_4-Li_2O-B_2O_3 pseudo-ternary system is shown in Fig 5.8.

The initial set of experiments (#1-5, Table 5.2), were performed in the system CaO-GeO_2-Li_2O-B_2O_3. Compositions were varied within the range of 2.0CaO-1.0GeO_2-(0.5-1.0)Li_2O_3-(0.34-0.78)B_2O_3. Boron oxide is a key glass-forming component. Composition 2.0CaO-1.0GeO_2-0.7$Li_2O_3$0.34B_2O_3 (#5, Table 5.2) with low contents of B_2O_3 was polycrystalline. Increasing the B_2O_3 considerably improves glass-forming ability of the mixture. Good glass samples were obtained with compositions #1, 2, and 3 (Table 5.2).

Lithium oxide usually acts as a network modifier [54], and increasing the content of Li_2O in the $CaO\text{-}GeO_2\text{-}Li_2O\text{-}B_2O_3$ system changes devitrification behavior and degrades glass-forming ability. The composition with increased Li_2O content (#2, Table 5.1) is characterized by a poor glass forming ability, and only a quarter of this batch was glass, and the rest was polycrystalline. A small amount of aluminum oxide improved glass-forming properties of $CaO\text{-}GeO_2\text{-}Li_2O\text{-}B_2O_3$ system (#6-9, Table 5.2). Aluminum may also act as a stabilizer for tetrahedral coordinated germanium [55] – the sites suitable for Cr^{4+} substitution.

A test of the emission properties of as-quenched (parent) glass revealed the presence of a broad band fluorescence centered at 920 nm attributed to Cr^{3+} in octahedral sites for two glass compositions, #1 and #3, both of them with increased B_2O_3 contents. All other glasses did not exhibit any emission at room temperature. Testing emission properties of devitrified samples showed the presence of a broad band emission centered at 1260 nm (Cr^{4+} in tetrahedral occupation) for all compositions except composition #3 with increased contents of B_2O_3.

The heat treatment procedure to initiate crystallization in the glasses was carried out within the temperature range of 450-550°C for different periods of time. As can be seen from table 5.2, only the first composition with a low content of Li_2O ($2.0CaO\text{-}1.0GeO_2\text{-}0.5Li_2O_3\text{-}0.5B_2O_3$) exhibited surface crystallization during devitrification. All other samples are characterized by volume crystallization. Adding 0.2 moles of $A1_2O_3$ to the system radically changed the crystallization behavior of the glass media. Heat treatment

of $A1_2O_3$ - containing samples (# 7-9, Table l) at 525°C for one hour yielded semi-transparent glass-ceramics with sub-micron sized crystallites. These compositions were used for more detailed examination. Fig.5.9 shows optical microscopy image of the transparent glass-ceramic sample (composition #7, Table l) exhibiting Cr^{4+} emission (b), and parent glass sample (a). Parent glass did not exhibit any emission, but heat treatment within the temperature range of 450 - 550°C initiated nucleation of Cr^{4+}-doped crystallites exhibiting NIR fluorescence. Fig. 5.10 shows images of the glass and glass-ceramic samples used for spectroscopic measurements.

Table 5.2. Glass compositions in CaO-GeO_2-Li_2O_3-B_2O_3 (Al_2O_3) system

Exp. #	CaO Mol.	GeO_2 Mol.	Li_2O Mol.	B_2O_3 Mol.	Al_2O_3 Mol.	Sample* "as-quenched"	Sample** after devitrification	Fluorescence			
								Parent glass		Glass-ceramics	
								Cr^{3+}	Cr^{4+}	Cr^{3+}	Cr^{4+}
1	2	1	0.5	0.5	-	G	S/N	Yes	None	Yes	Yes
2	2	1	1	0.5	-	G/P	V/O	None	None	None	Yes
3	2	1	1	0.78	-	G	V/O	Yes	None	None	None
4	2	1	0.7	0.5	-	G	V/O	None	None	None	Yes
5	2	1	0.7	0.34	-	P	-	-	-	-	-
6	2	1	1	0.5	0.1	G	V/O	None	None	None	Yes
7	2	1	1	0.5	0.2	G	V/T	None	None	None	Yes
8	2	1	0.85	0.5	0.2	G	V/T	None	None	None	Yes
9	2	1	0.92	0.5	0.2	G	V/T	None	None	None	Yes

* G/P - glass/polycrystal, G-glass, P-polycrystal

** S/N - surface crystallization, not-transparent; V/O - volume crystallization, opaque (semi- transparent); V/T - volume crystallization, transparent.

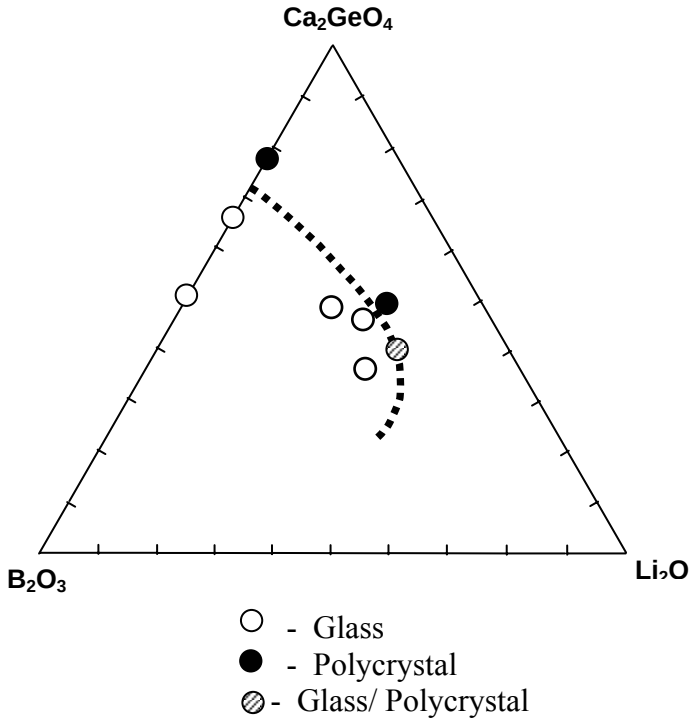

Fig. 5.8: Glass formation in Ca_2GeO_4-Li_2O-B_2O_3 system

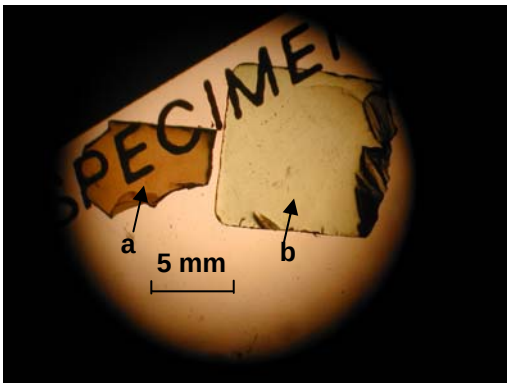

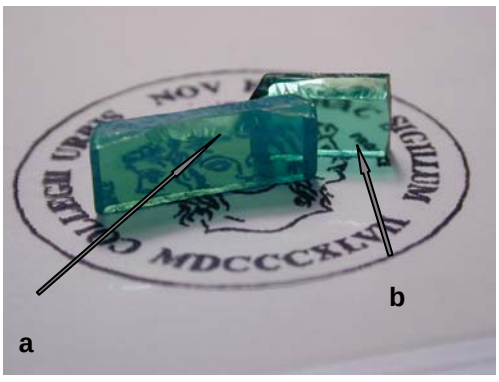

Fig. 5.9: Optical microscopy picture of parent glass (a) and glass-ceramic (b) samples (transmitted light)

Fig.5.10: Glass-ceramic (a) and parent glass (b) samples

The SEM study was carried out to visualize crystallites formed during after-growth heat-treatment in the glass media. Fig. 5.11 shows the scanning electron micrographs recorded for the fractured sample after heat-treatment at 525^{o}C for 1 h. The crystals formed in the glass media after heat-treatment have spherical shape with a size of up to 1 □m. We expect that crystallites with the size below 100 nm may be formed by adjustment of the initial glass composition and heat treatment procedure parameters.

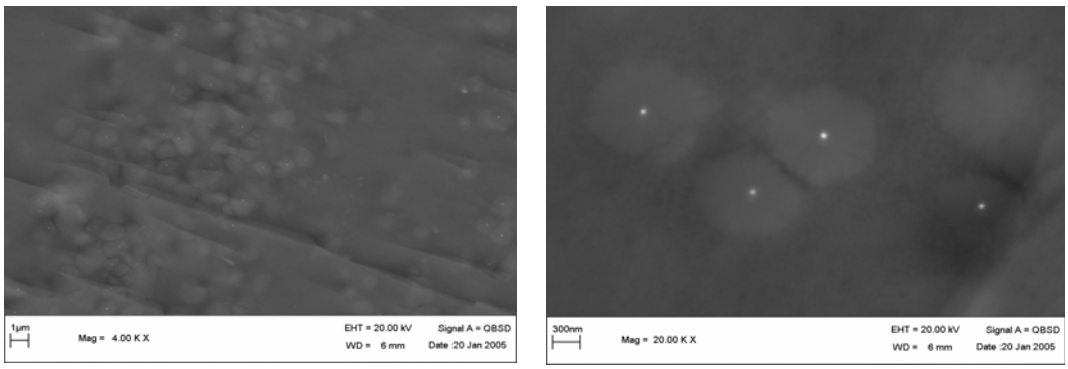

a) b)

Fig. 5.11: SEM picture of crystallites formed during after growth heat-treatment (composition #6, 525^{oC}(1h)) at 4.00k x (a) and 20.00 k x (b) magnification.

5.4 X-ray diffraction measurements

To identify the type of Cr^{4+}-doped crystals X-ray powder diffraction measurements have been carried out. All parent glasses were characterized by X-ray diffraction pattern without reflections. The appearance of X-ray diffraction reflections after devitrification is a firm evidence of crystal formation in the glass media. Evolution of the crystalline phase in glass media during devitrification as a function of temperature and duration of heat-

treatment is shown in Fig. 5.12 for composition #9. Heat treatment at 475°C for the period of 1 hour leads to the appearance of the first few reflections. Increasing the temperature and the duration of heat treatment, leads to an increased intensity of the reflections and the appearance of new reflections. X-ray diffraction spectra of glass-ceramics prepared from the parent glasses containing different amounts of Li_2O, and also with and without Al_2O_3, are characterized by similar reflections (Fig. 5.13). It means that there are no critical changes in the crystalline structure of the crystallites formed during devitrification in that glass-ceramic composition range. A typical X-ray diffraction spectrum of glass-ceramic sample (composition #7 after heat-treatment at 525 °C for 1.5 hour) is shown in Fig. 5.14. As can be seen from Fig. 5.14, the two major crystalline phases may be identified as Li_2BGeO_4 and Ca_2GeO_4. Some unknown XRD peaks are also present in the spectrum.

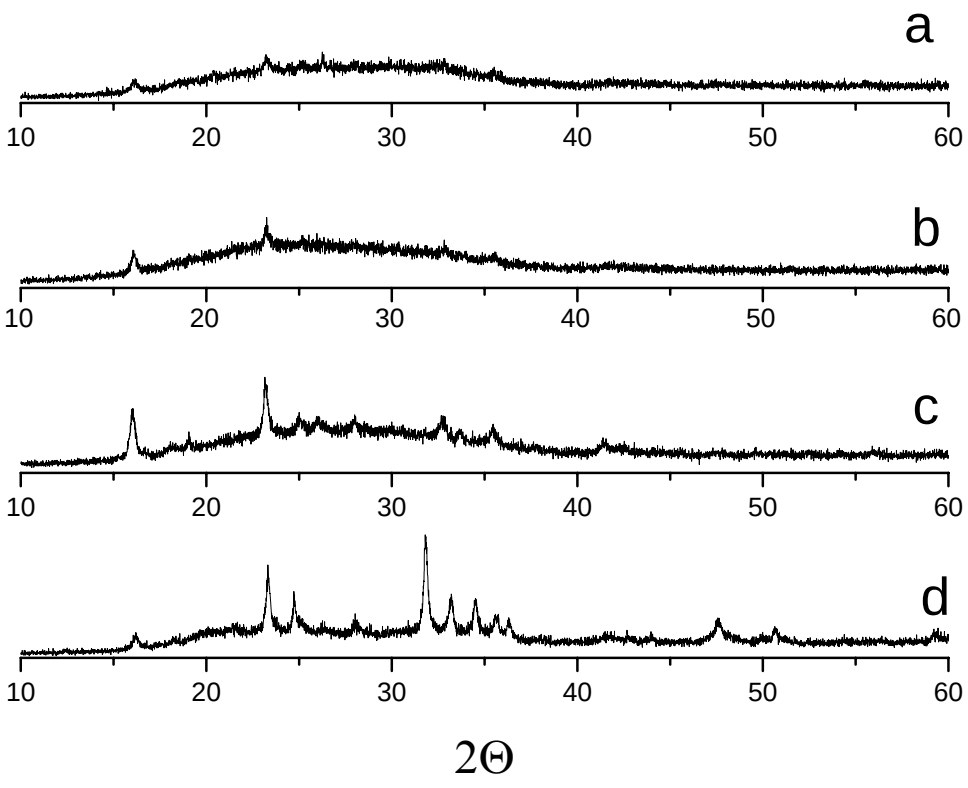

Fig. 5.12: X-ray diffraction spectra of 2.0CaO-1.0GeO_2-0.92Li_2O-0.5B_2O_3-0.2Al_2O_3 (#9, Table2)

a 460°C (1 h)
b 475°C(1 h)
c 490°C(15 min)
d 490°C(1.5 h)

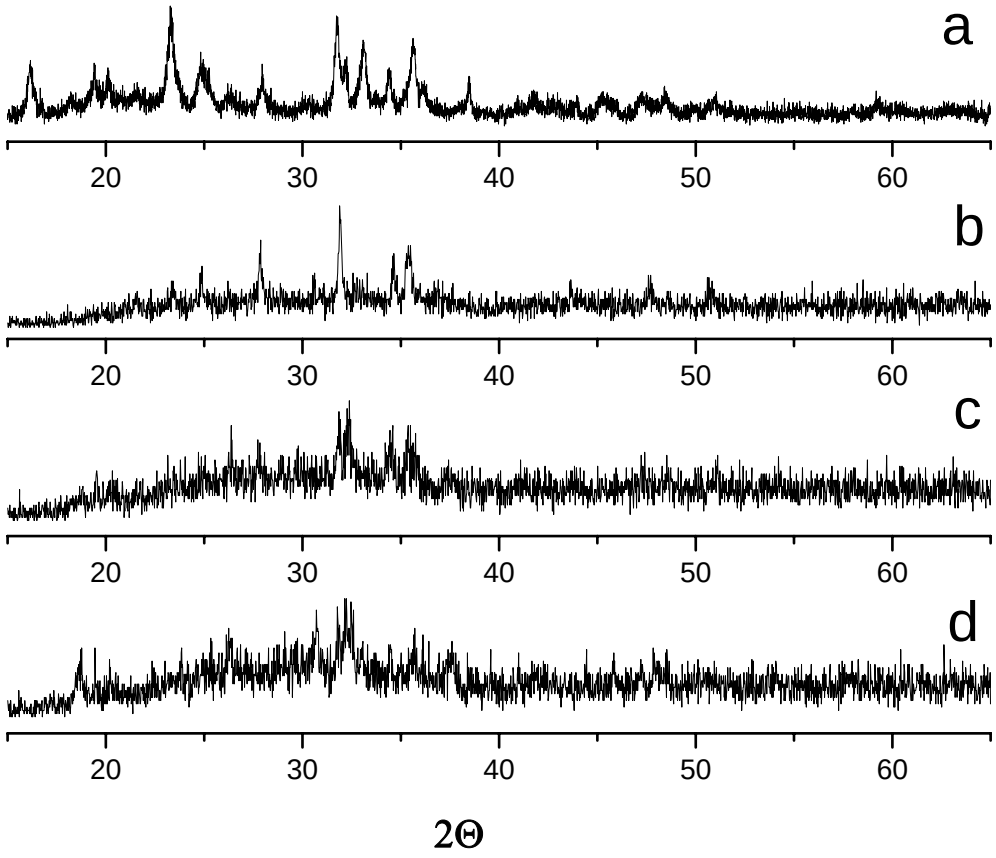

Fig. 5.13: X-ray diffraction spectra of glass-ceramic samples of different initial glass-composition (different Li_2O and Al_2O_3 contents)

a) #7 (2.0CaO-1.0GeO_2-1.0Li_2O-0.5B_2O_3-0.2Al $_2O_3$)

b) # 2 (2.0CaO-1.0GeO_2-1.0Li_2O-0.5B_2O_3)

c) #4 (2.0CaO-1.0GeO_2-0.7Li2O-0.5B_2O_3)

d) #1 (2.0CaO-1.0GeO_2-0.5Li_2O-0.5B_2O_3)

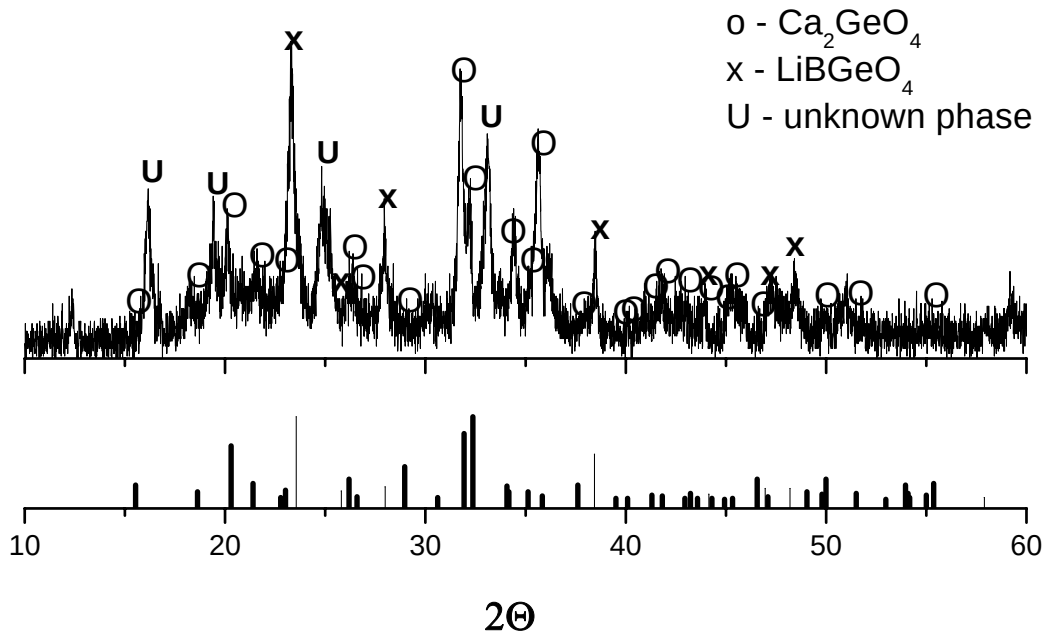

Fig. 5.14: X-ray diffraction pattern of glass-ceramic sample #7 (2.0CaO-1.0GeO_2-1.0Li_2O-0.5B_2O_3- 0.2Al $_2O_3$) and reference data (thick drop line -Ca_2GeO_4 JCPDS #26-0304, and thin drop line - $LiBGeO_4$ JCPDS #33-0792)

5.5 Fluorescence and absorption measurements

Glasses of various compositions (Table 5.2) are characterized by similar absorption spectra with a maximum at ~ 660 nm and a long tail extending beyond 1000 nm (Fig. 5.15, curve a). A long tail over 1000 nm in absorption is a feature commonly observed in Cr^{4+} doped crystals. The absorption bands of Cr^{4+} located between 600 and 900 nm are usually attributed to the $^3A_2$ □ $^3T_1$ transitions and the weak near infrared absorption band around 1 □m - to the $^3A_2$ □ $^3T_2$ transitions. Similar spectra were observed in Cr-doped Ca-Al-Si-O glasses [56] where the Cr^{4+}-oxidation state was achieved. Identification of Cr

valence state in the parent glasses (before heat treatment) by taking excitation emission spectra is difficult because of the prevailing non-radiative processes and lack of emission at room temperature.

The heat treatment procedure and formation of crystallites in glass media does not essentially change absorption spectra except for the appearance of a background related to scattering off crystallites (Fig.5.15). Light scattering significantly increases with the increasing temperature and duration of heat treatment caused by the increasing size of crystallites.

Crystallization occurring in glasses during devitrification causes the appearance of an emission in the 1000-1600 nm wavelength range with a maximum at about 1260 nm (Fig.5.16). Increasing the temperature and duration of heat treatment leads to increase of the number and size of crystallites that increase absorption of glass-ceramic media, and, as a result, the intensity of the fluorescence also increases, as shown in Fig. 5.16. Broad-band emission with a maximum around 1260 nm remains the same for all varieties of initial glass composition with different contents of Li_2O and $A1_2O_3$ shown in Table 5.1, which may confirm that the same type of crystallites is formed in these glasses after devitrification.

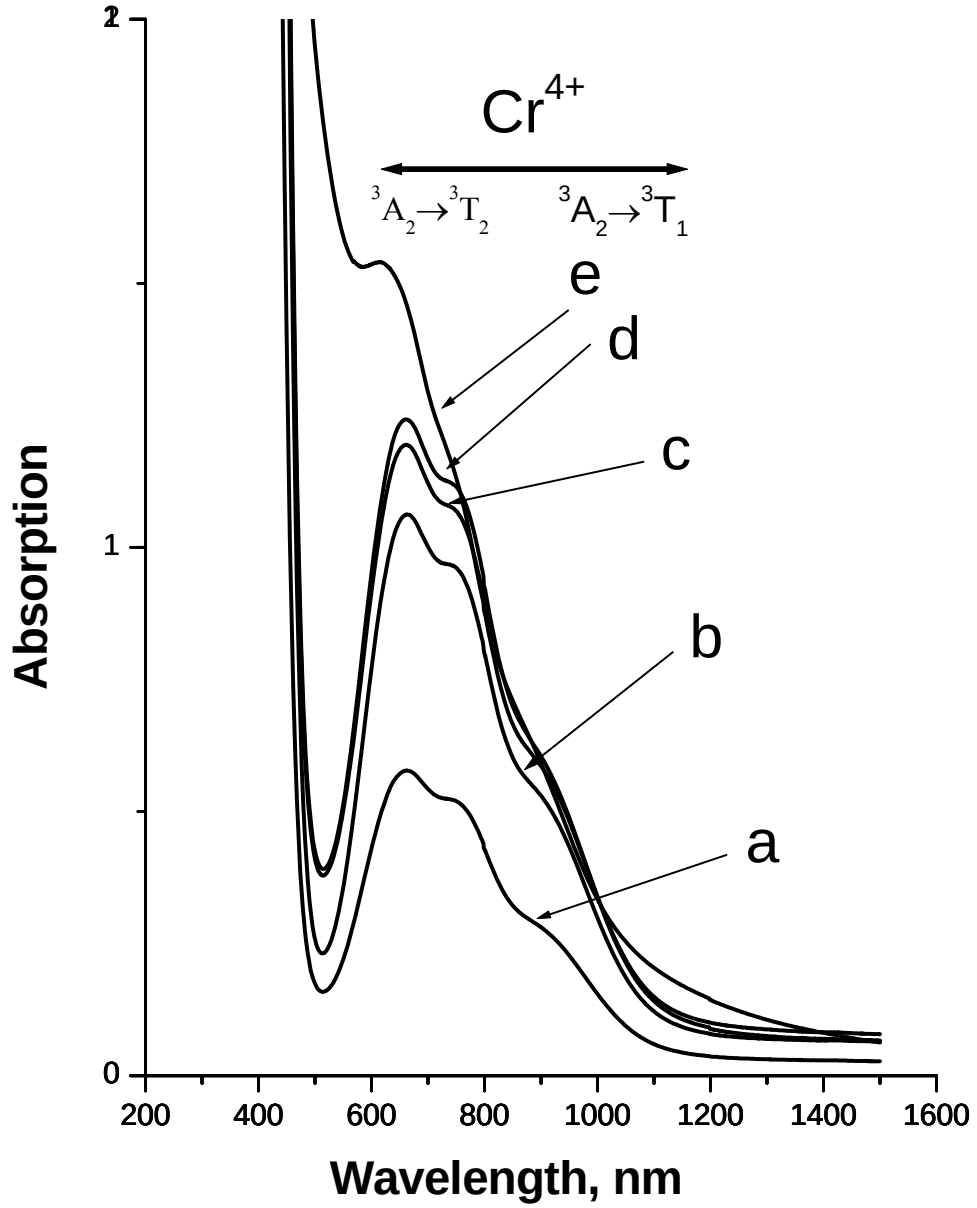

Fig. 5.15: Absorption spectra of 2.0CaO-1.0GeO_2-0.92Li_2O-0.5B_2O_3–0.2Al_2O_3 glass sample before heat treatment and after different heat treatment procedures:

a – parent glass, no heat trearment,
b - 460^{o}C(1 h),
c - 475^{o}C(1 h),
d - 490^{o}C(15 min) ,
e - 490^{o}C (30 min))

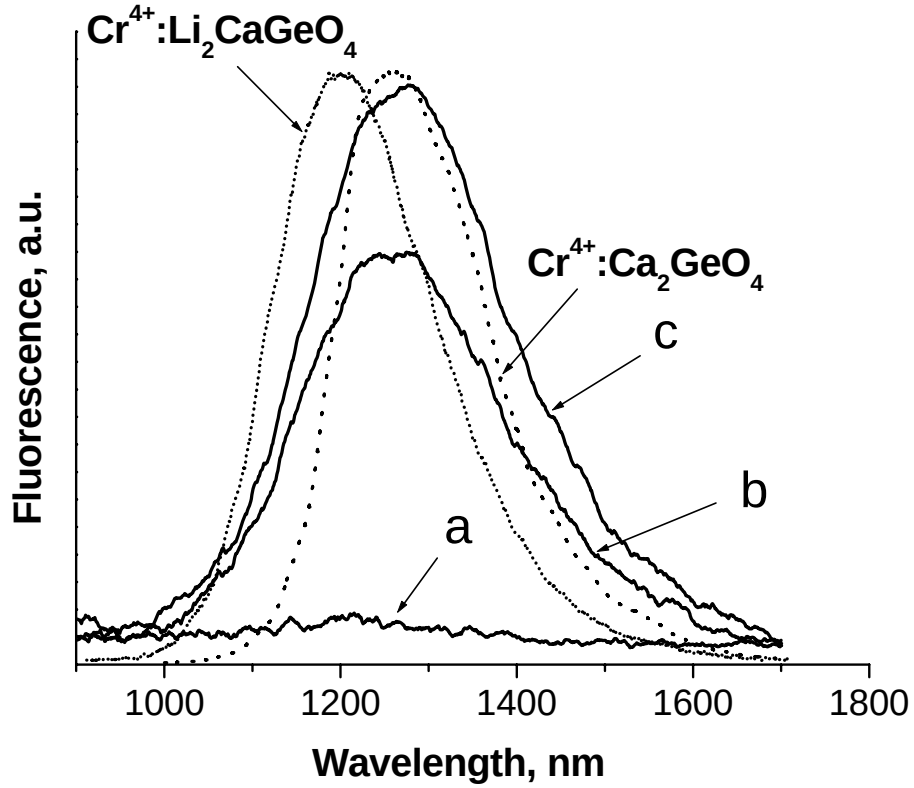

Fig. 5.16: Fluorescence spectra of glass-ceramic #9 (2.0CaO-1.0GeO_2-0.92Li_2O-0.5B_2O_3-0.2Al_2O_3) after different hear-treatment procedures: a-490^{o}C(15 min), b-490^{o}C(30 min), c- 490^{o}C(1.5 h), and fluorescence of Cr^{4+}:Li_2CaGeO_4 and Cr^{4+}:Ca_2GeO_4 reference samples.

Additional data for the identification of crystallites exhibiting near infrared emission may be acquired from the measurements of spectroscopic properties. A major feature of Cr^{4+} ions occupying tetrahedral sites in the crystal structure is a high probability of non-radiative transitions. For this reason the number of Cr^{4+}-doped materials exhibiting useful near infrared fluorescence at room temperature is very limited. Only three structural types of crystals with Cr^{4+} emission can be formed in the CaO-GeO_2-Li_2O-Al_2O_3-B_2O_3 system:

Cr^{4+}:Ca_2GeO_4, Cr^{4+}:Li_2CaGeO_4, and Cr^{4+}:$LiAlO_2$. The latter one can be taken out of the consideration because Cr-doped glass-ceramic samples are also produced from the glass compositions without Al_2O_3 (Table. 5.2). Therefore, in order to make the structural identification of crystallites in glass-ceramics from spectroscopic data, only Cr^{4+}:Ca_2GeO_4 and Cr^{4+}:Li_2CaGeO_4 may be considered as a potential source of near infrared fluorescence. However, X-ray powder diffraction reflections of Li_2CaGeO_4 absolutely do not match reflections of glass-ceramics. As can be seen from Fig. 5.13, a number of XRD reflections of glass-ceramics including the maximum one at $2\theta \sim 32^o$ may be assigned only to Ca_2GeO_4 with increased lattice parameters. Therefore, Cr^{4+}:Ca_2GeO_4 crystallites have to be considered as a sole source of fluorescence in glass-ceramics.

Fluorescence spectra of Cr^{4+}:Ca_2GeO_4, Cr^{4+}:Li_2CaGeO_4 and Cr-doped glass-ceramic samples are shown in Fig. 5.14. The maximum of the emission of Cr^{4+}:Li_2CaGeO_4 is located at ~1180 nm, Cr^{4+}:Ca_2GeO_4 at ~1260 nm, and Cr-doped glass-ceramics at ~1280 nm. The spectrum of Cr^{4+}:Li_2CaGeO_4 is characterized by a blue shift of about 100 nm with respect to the Cr-doped glass-ceramics spectrum. The spectrum of the Cr-doped glass-ceramics is very similar to the spectrum of Cr^{4+}:Ca_2GeO_4, but slightly broader.

Taking into consideration the X-ray diffraction results and fluorescence spectra, formation of Cr-doped structurally distorted Ca_2GeO_4 crystallites in glass-ceramics may be affirmed. The structure distortion could be caused by hetero-valent substitutions with Li or B occurring during the nucleation and growth of crystallites in the solid state during devitrification.

5.6 Thermal analysis and crystallization kinetics

The DTA curves (Fig. 5.17) for $CaO\text{-}GeO_2\text{-}Li_2O_3\text{-}B_2O_3$ glasses are typical for phase separated glass samples [57]. The curve exhibits a slope change in the 450-500^{o}C temperature range related to the glass transition. The inflection point at the slope change on the DTA curve at 485^{o}C (minimum on the derivative plot in Fig. 5.17b) is usually considered to be the glass transition temperature. The exothermic maximum at 560°C corresponds to the separation of the crystalline phase. Crystallization starts at 540°C (see onset of the maximum). Melting of the crystalline phase at a higher temperature appears as a minimum on the DTA curve at 908°C. Cooling down of the sample without quenching leads to crystallization of the material at 800°C.

Preparation of high quality glass ceramics usually includes two steps of heat treatment. The first heat treatment is carried out for nucleation, and second one – for controlled growth of nuclei formed during previous heat treatment. To evaluate the optimal temperature condition of heat treatment procedure, the DTA runs were carried out for the samples having undergone heat treatment at different temperatures for the same (6 hours) period of time. It was shown that the position of the crystallization peak on the DTA curve depends on the nucleation temperature heat treatment. A number of heat treatment experiments followed by DTA measurements have been carried out and results showing crystallization temperature shift that depend on the temperature of nucleation are shown in Fig. 5.18. The temperature of heat treatment when some rearrangements in the glass

structure corresponding to nucleation process in glass media just starts is around 460^{o}C.

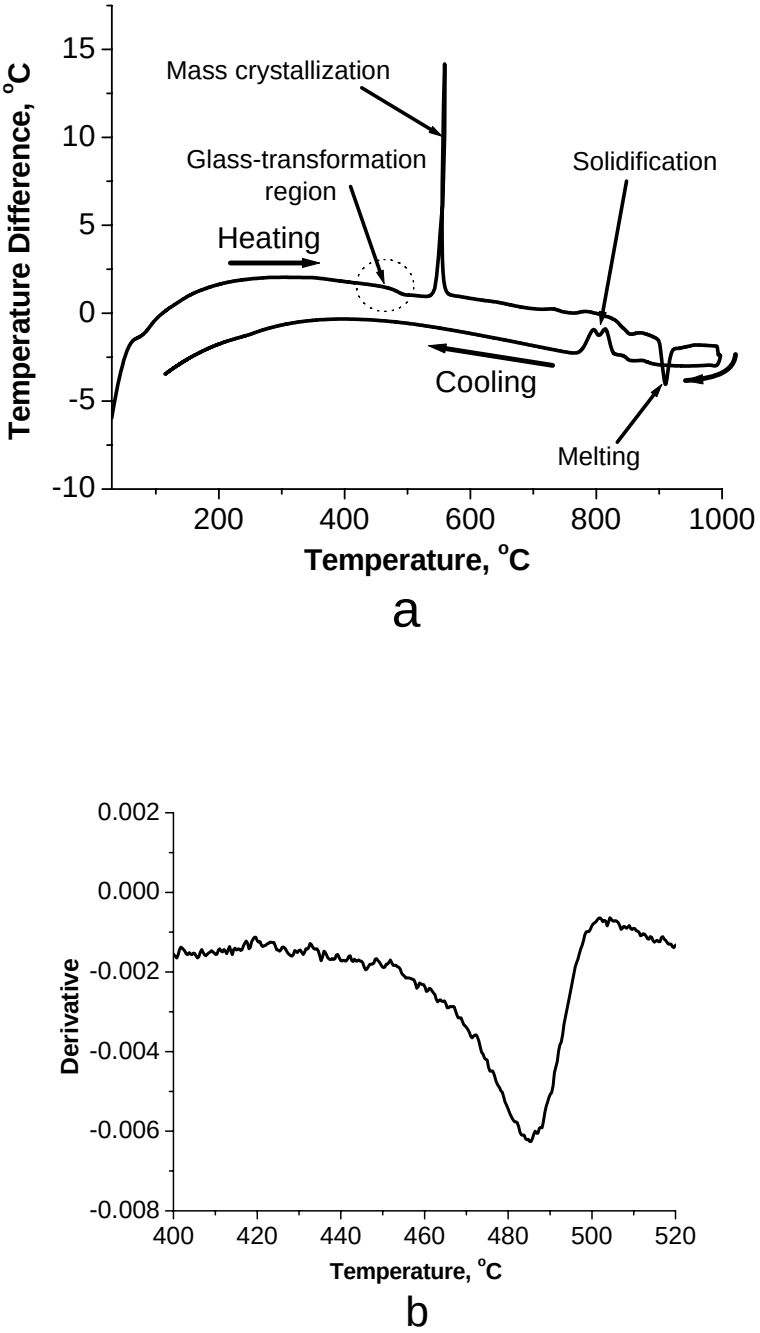

Fig. 5.17: Differential thermal analysis results (a) with derivative plot (b) of glass transformation region (composition #7, table 5.2).

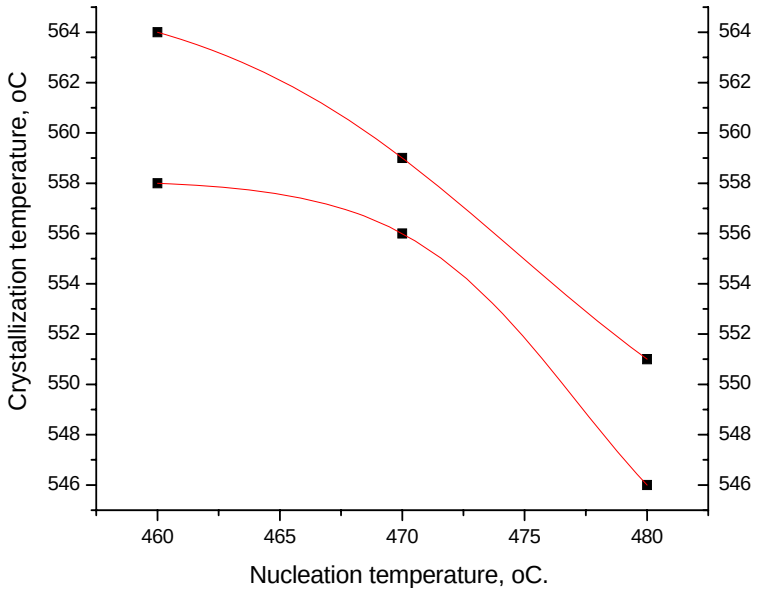

Fig. 5.18: Crystallization temperature (position of crystallization peak on DTA curve) as a function of heat treatment temperature

CHAPTER 6

NUCLEATION AND CRYSTALLIZATION KINETICS

6.1 Glass Transition

For detailed study of the nucleation and crystallization kinetics of Cr-doped Ca_2GeO_4-$Li_2O(Al_2O_3)$-B_2O_3 a series of DTA-DSC experiments were conducted. The composition of the glass sample was $2CaO - 1GeO_2 - 1Li_2O - 0.5B_2O_3 - 0.2Al_2O_3$ (#7, Table 5.2). A typical curve is shown in figure 6.1 for a 20mg sample of the glass that was heated to 600^{o}C. An endotherm around 489^{o}C followed by an exotherm at 551^{o}C, are observed, which are associated with the glass transition (Tg) and the crystallization (Tc) temperatures of the as-quenched sample. The glass transition temperature and the onset of the crystallization temperature are identified as the temperature corresponding to the intersection of two linear portions of the transition (glass transition and crystallization) elbows of the DSC trace. The DSC traces that are obtained for Cr-doped Ca_2GeO_4-$Li_2O(Al_2O_3)$-B_2O_3 glass at different heating rates (5, 10, 15, 20, and 25 K/min) are shown in the Fig. 6.2 The peak glass transition temperature (Tgp) is the temperature at which it attains its maximum, which is the peak temperature of the endotherm in the DSC curves. There is an upward shift in Tgp with increasing heating rate, α.

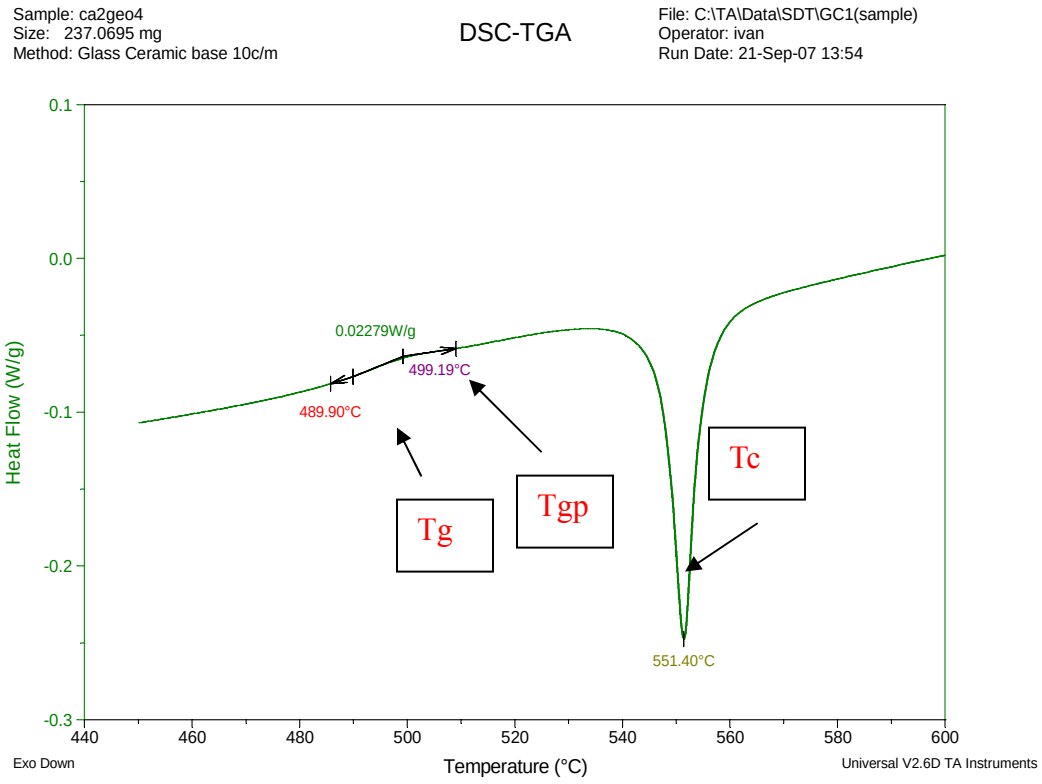

Fig. 6.1 DSC curve for glass sample #7 (Table 2)

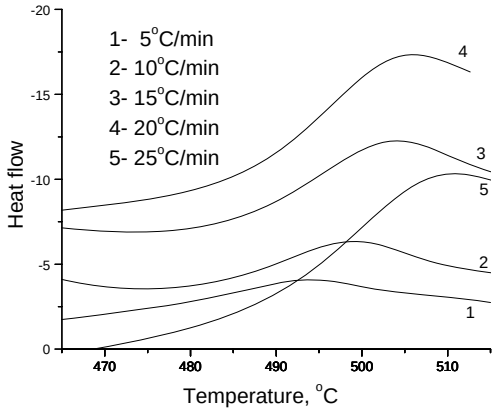

Fig. 6.2: Glass transition region on DSC curves for different heating rates

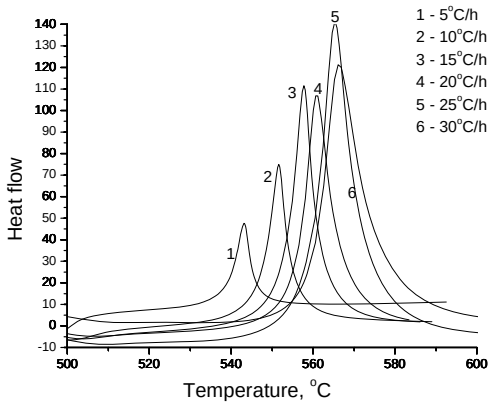

Fig. 6.3: Crystallization peaks on DSC curves at different heating rates

The Tg dependence on the heating rate (α) has been analyzed using the following three different approaches. The empirical relation between Tg and according to Lasocka [54] is in the following form:

$$Tg = A + B \ln \alpha \qquad (5.1)$$

where A and B are constants for a given glass composition and at a particular temperature T. The constant B is related to the method of quenching the sample. Lowering the cooling rate of the melt, lowers the B-value. It signifies the response of the configurational changes within the glass transition region to the heating rate [58]. The plot of Tg versus log α for Cr-doped $CaO–GeO_2–Li_2O–B_2O_3(Al_2O_3)$ glass and a theoretical fit (solid line) are shown in Fig. 6.4 and its values in Table 6.1. A Tg dependence on the heating rate (α) was obtained from the slope of the graph and B was the x-y intercept. The values that are obtained for A and B are 748 and 8.1 K, respectively, for Cr-doped $CaO–GeO_2–Li_2O–B_2O_3(Al_2O_3)$ glass. Therefore, the above relation can be written as

$Tg = 748 + 8.1 \ln \alpha$

Table 6.1 Values of Tg and α

Tg (Cº)	Tg(K)	α	log α
481.99	754.99	5	0.69897
483.36	756.36	10	1
485.53	758.53	15	1.176091
486.2	759.2	20	1.30103
487.8	760.8	25	1.39794

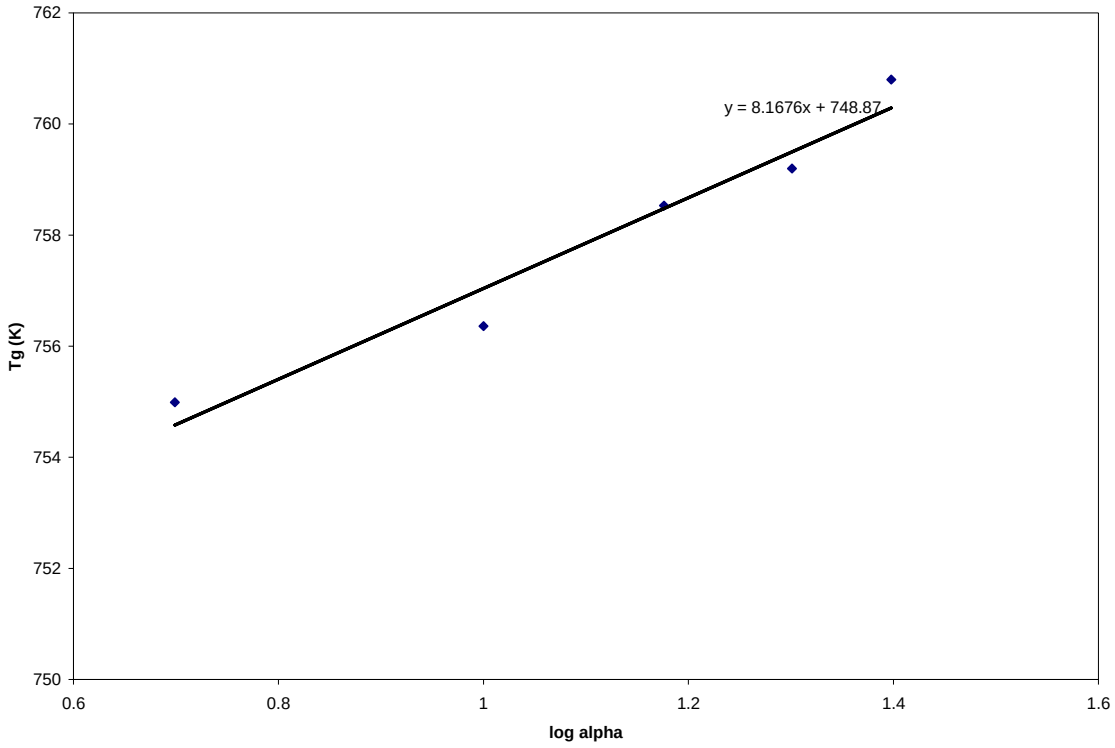

Fig 6.4 Tg versus Log (α) for Cr-doped $CaO–GeO_2–Li_2O–B_2O_3(Al_2O_3)$ glass

The second approach for analyzing Tg or Tgp is based on the Kissinger's formula [36], in which the Tgp has a linear dependence on the heating rate, according to which

$$\ln(\alpha/T^2_{gp}) = -Eg/RT_{gp} + \text{constant} \qquad (5.2)$$

where Eg is the activation energy associated with the glass transition and R is the universal gas constant.

A plot of $\ln(\alpha / T^2_{gp})$ versus $(1000/T_{gp})$ gives a linear relation, which is depicted in Fig. 6.5. The experimental points of the present work along with a theoretical fit (solid line) to

the above relation suggest its validity. From the slope of the straight line, the value of Eg is found to be 517 kJ/mol. This value is calculated by multiplying the slope of the fitted line by the gas constant.

Tgp	Tgp(K)	α	$\ln(\alpha / T^2_{gp})$	ln α
494.47	767.47	5	-11.6768	1.302982527
499.4	772.4	10	-10.9964	1.294665976
503.54	776.54	15	-10.6016	1.28776367
505.25	778.25	20	-10.3184	1.284934147
510	783	25	-10.1074	1.277139208

Table 6.2 Values of $\ln(\alpha / T^2_{gp})$ and $(1000/T_{gp})$ for Cr-doped $CaO–GeO_2–Li_2O–B_2O_3(Al_2O_3)$ glass

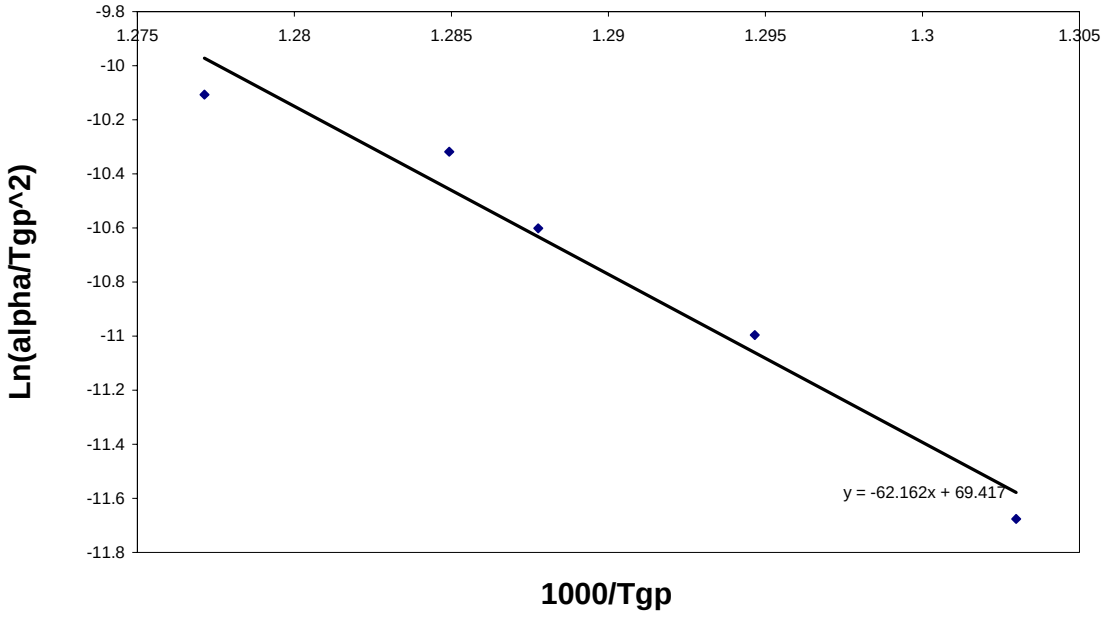

Fig. 6.5: A plot of $\ln(\alpha / T^2_{gp})$ versus $(1000/T_{gp})$ for Cr-doped $CaO–GeO_2–Li_2O–B_2O_3(Al_2O_3)$ glass

The third approach, which is due to Moynihan et al. [59], is given as

$$d \ln \alpha / d(1/T_{gp}) = -Eg/R \qquad (6.3)$$

the necessary constraint is that prior to reheating, the glass must be cooled from above to well below the glass transition region at a rate, which is either equal to or proportional to the reheating rate. In the present experiment, the sample is heated and cooled around the glass transition region in such a way that the cooling rate is equal to the reheating rate [58]. The value obtained for Eg from Fig. 6.6 is 530kJ/mol, which is in excellent agreement with that obtained by Kissinger's method.

Tgp (C^0)	Tgp (K)	α	ln(α)	1000/Tgp
494.47	767.47	5	1.609438	1.302982527
499.4	772.4	10	2.302585	1.294665976
503.54	776.54	15	2.70805	1.28776367
505.25	778.25	20	2.995732	1.284934147
510	783	25	3.218876	1.277139208

Table 6.3 Values of ln(α)and ($1000/T_{gp}$) for Cr-doped $CaO–GeO_2–Li_2O–B_2O_3(Al_2O_3)$ glass

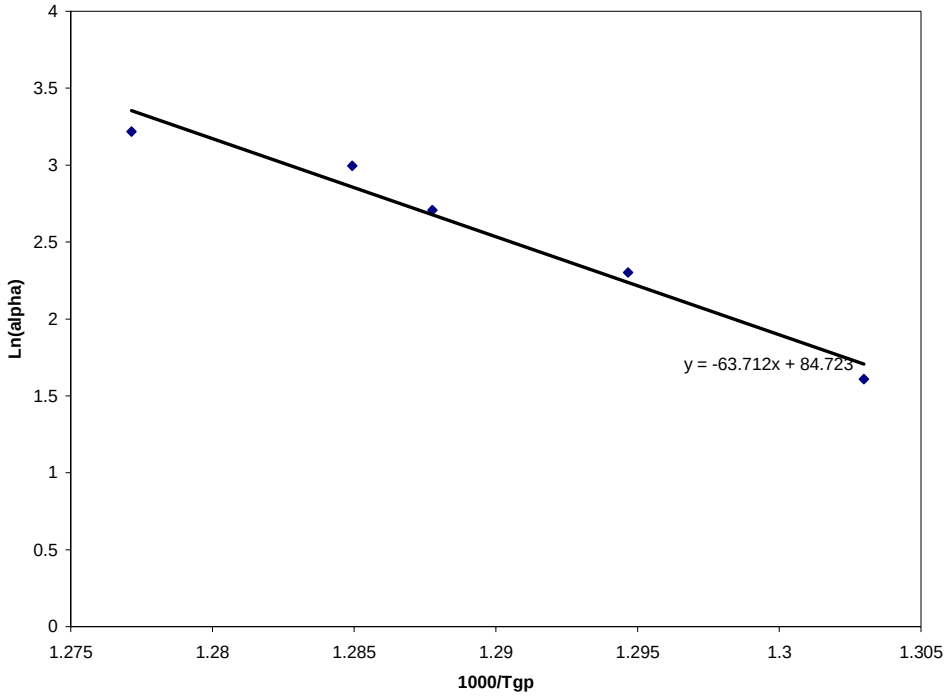

Fig. 6.6: A plot of ln(α)versus (1000/T_{gp}) for Cr-doped CaO–GeO_2–Li_2O–B_2O_3(Al_2O_3) glass

6.2 Non-Isothermal Crystallization

Crystallization of the Cr-doped CaO–GeO_2–Li_2O–B_2O_3(Al_2O_3) glass has been studied by the nonisothermal method. Various theoretical methods have been suggested to understand the nucleation and growth process using the non-isothermal DSC data. All the methods assume a constant heating rate, α, in the DTA or DSC experiments:

$$T = T_0 + \alpha t \qquad (6.4)$$

where T_0 is the initial temperature (300 K) and α is the heating rate. The objective of all these methods is to identify two parameters, which, when plotted one against the other, will result in a straight line, from the slope of the line, the overall effective activation energy, Ec, or the order of the reaction, n, are calculated. Non-isothermal exotherms of Cr-doped $CaO–GeO_2–Li_2O–B_2O_3(Al_2O_3)$ glass crystallization at various heating rates (5, 10, 15, 20, 25, and 30 K/min) are shown in Fig. 6.3.

The crystallization activation energy Ec could be calculated using the following formula suggested by the Augis and Bennett [60] which gives 415 KJ/mol. The resulting values are shown in table 6.3 and Fig. 6.7.

$$\ln [\alpha/(T_p-T_0)] = \ln K_0 - E_c/RT_p \qquad (6.5)$$

Tp (C^0)	Tp(K)	alpha	ln(α/(Tp-300))	1000/Tp
543.13	816.13	5	-4.63692	1.22529499
551.64	824.64	10	-3.96013	1.212650369
557.76	830.76	15	-3.56626	1.203717078
560.67	833.67	20	-3.28405	1.199515396
565.33	838.33	25	-3.0696	1.192847685
566.11	839.11	30	-2.88872	1.191738866

Table 6.3 Values of ln(α/(Tp-300)) and ($1000/T_p$) for $CaO–GeO_2–Li_2O–B_2O_3(Al_2O_3)$ glass

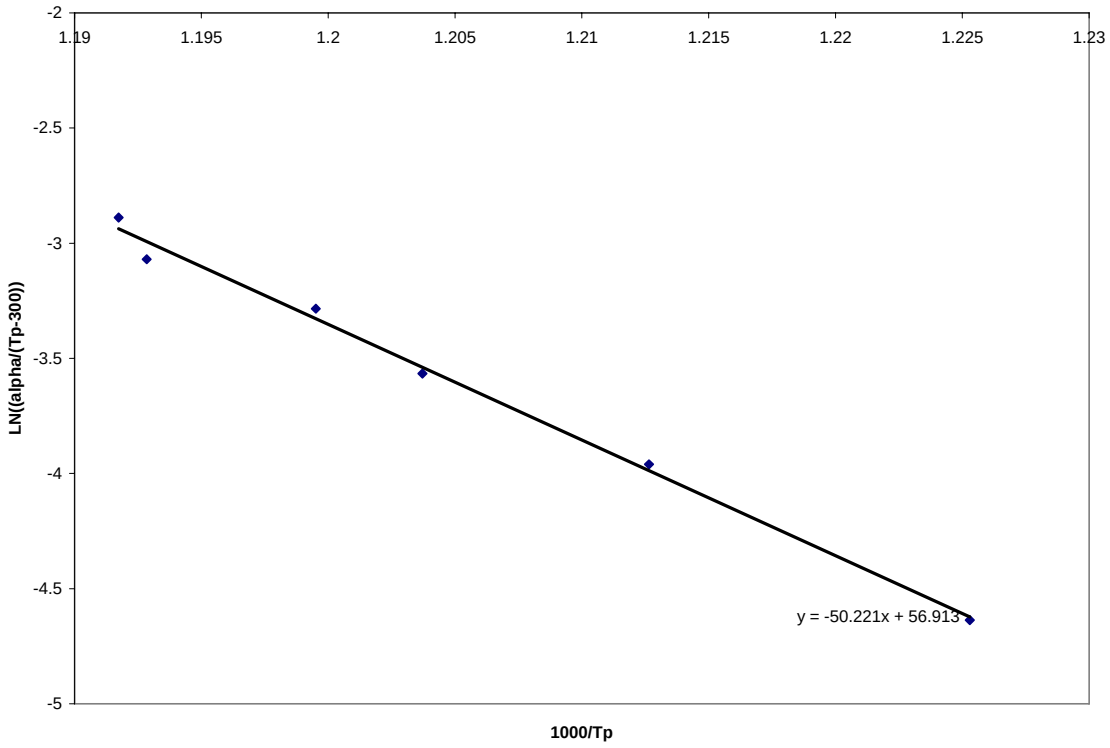

Fig. 6.7 A plot of ln(α/(Tp-300)) versus (1000/T_p) for Cr-doped CaO–GeO_2–Li_2O–B_2O_3(Al_2O_3) glass

Kissinger [36] developed a method, which could be used commonly for analyzing the crystallization data in DSC or DTA experiments. According to which

$$\ln (\alpha/T^2_p) = -Ec/RT_p + \text{constant} \qquad (6.6)$$

A plot of $\ln(\alpha / T^2_{p)}$ versus $(1000/T_p)$ is shown in Fig. 6.8 and its values in table 6.4. The value that is obtained for Ec is 414 kJ/mol, which is in close agreement with that obtained by Augis and Bennett's method.

Tp (C^0)	Tp(K)	α	of $\ln(\alpha / T^2_{gp})$	1000/Tp
543.13	816.13	5	-11.7997	1.22529499
551.64	824.64	10	-11.1273	1.212650369
557.76	830.76	15	-10.7366	1.203717078
560.67	833.67	20	-10.4559	1.199515396
565.33	838.33	25	-10.2439	1.192847685
566.11	839.11	30	-10.0635	1.191738866

Table 6.4 Values of $\ln(\alpha / T^2_{p)}$ and $(1000/T_p)$ for Cr-doped $CaO–GeO_2–Li_2O–B_2O_3(Al_2O_3)$ glass

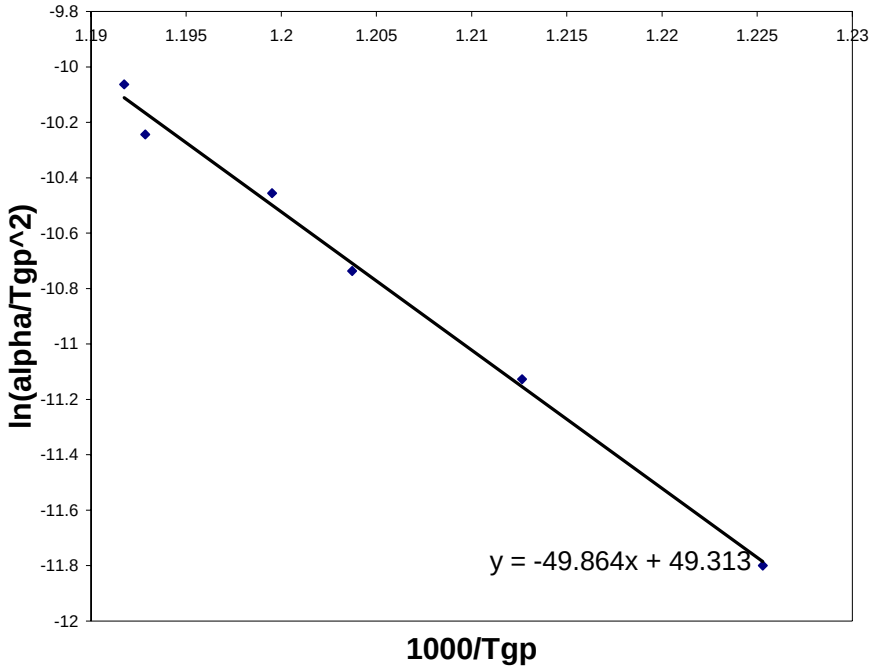

Fig. 6.8: A plot of $\ln(\alpha / T^2_{p)}$ versus $(1000/T_p)$ for Cr-doped $CaO–GeO_2–Li_2O–B_2O_3(Al_2O_3)$ glass

6.3 Calculations of the Avrami constant and the order of crystallization

Augis and Bennett [60] pointed out that the reactions with the same Ec but different values for n will show a crystallization peak at the same temperature. The value of n determines the shape of the crystallization peak; the higher the value of n, the narrower the peak. According to Eq. (6.7), a sharp peak (small ΔT_{FWHM}, large n) implies bulk crystallization while a broad peak (large ΔT_{FWHM}, small n) signifies surface crystallization. The following expression could be used for estimating the value for n:

$$n = 2.5xT^2_p /(\Delta T_{FWHM}(Ec/R)) \qquad (6.7)$$

where ΔT_{FWHM} is the width of the crystallization peak at half-maximum. The values of the Avrami exponent, n, were computed from Eq. (6.7) for a heating rate of 20 ^{0}C/min. At this heating rate, ΔT_{FWHM} was calculated to be 9 degrees, Tp equal to 833 K and Ec calculated from Augis and Bennet as 415 KJ/mol. The value of n was calculated to be 3.8 which suggest 3-dimensional bulk crystallization, just as expected based on visual studies.

The method proposed by Ozawa [61] is also used to deduce the order of the crystallization process, n. The expression for x (fraction of crystallization) is given by

$$x = 1- \exp[-(k(T-T_0)/\alpha)^n] \qquad (5.8)$$

Taking the logarithm of the above expression twice, one obtains

$$\ln[-\ln(1-x)] = n \ln[k(T-T_0)] - n \ln \alpha \qquad (5.9)$$

A plot of ln[-ln(1-x)] versus ln α yields a straight line with a slope equal to n. Alternately, by rearranging the above equation one arrives at

$$d\{\ln[-\ln(1-x)]\}/d(\ln \alpha) = -n \qquad (5.10)$$

To calculate n, Fig 6.10 was used to plot a curve of fraction crystallized vs. temperature for different heating rates, Fig 6.3. An isotherm at 830 K from this figure gives a straight line fitting with a slope of 3.6. The average value of the crystallization order parameter, n, is equal to 3.6, which suggests that there is mostly three dimensional bulk crystallization within the glass. Figure 6.9 shows the isotherm with values shown in table 6.5.

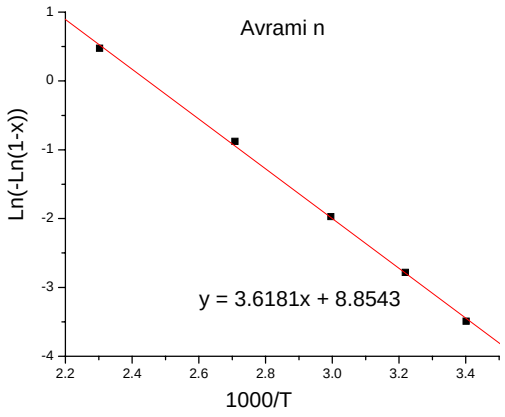

Fig.6.9: Avrami 'n' coefficient computation

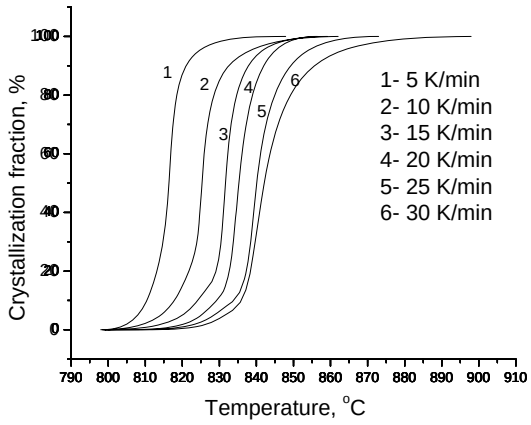

Fig.6.10: Fractions of crystalline phase at different heating rates.

α	ln α	Ln(-ln(1-x))	x
15	2.708050201	-0.8782355	0.34
20	2.995732274	-1.97139774	0.13
25	3.218875825	-2.78263253	0.06
30	3.401197382	-3.49136695	0.03
10	2.302585093	0.475885	0.8

Table 6.5. Values of $\ln(\alpha / T^2_{gp})$ and $(1000/T_{gp})$ for Cr-doped $CaO–GeO_2–Li_2O–B_2O_3(Al_2O_3)$ glass

The n values are in good agreement for the Augis and Bennet approximated and the method proposed by Ozawa.

CHAPTER 7

SEM AND CONFOCAL IMAGING STUDIES

7.1 Scanning Electron Microscopy

Our efforts have been also focused on the evaluation of a technique enabling to visualize study of crystallization kinetics in glass media during devitrification. The most significant problem proved to be estimation (visualization) of size of crystallites after different heat-treatment procedures. Unfortunately, the TEM method failed to provide good images of nucleated glass media because of a relatively big size of crystallites (over 100 nm).

SEM was used to observe the structure of glass-ceramics. The sample preparation method was a key for these experiments. We used two different sample preparation techniques involving fracturing and etching procedures to provide clean surface for SEM study. Images of glass-ceramic samples after etching in diluted HCl (1:100) are shown in Fig. 7.1. Unfortunately this sample preparation technique did not provide reproducible results. Different etching conditions gave us different character and size of etched spots on the surface for the same glass-ceramic material.

The best results allowing average estimation of size of crystallites was found to be SEM study of the material after hacking bulk glass-ceramic sample to pieces. The resulting crumb SEM images allowed an estimation of an average size of crystallites. Examples of SEM image of fractured surface of glass-ceramics are shown in Fig. 7.2.

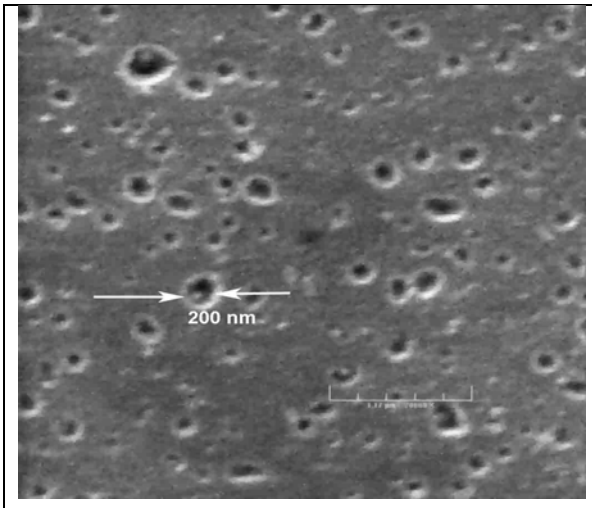

Fig.7.1 (a) SEM image of glass-ceramic sample after etching in HCl solution for 1 min

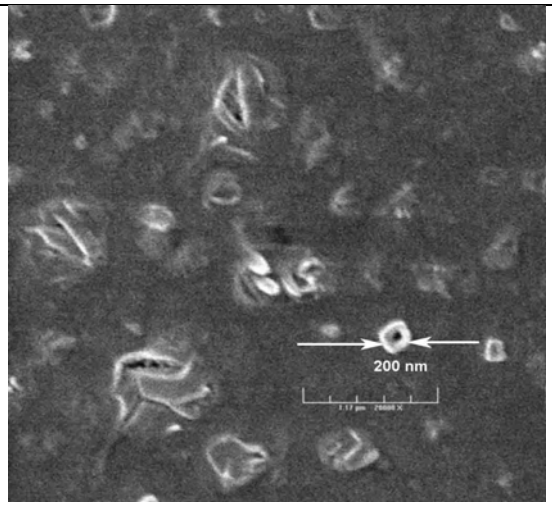

Fig.7.1 (b) SEM image of glass-ceramic sample after etching in HCl solution for 5 min

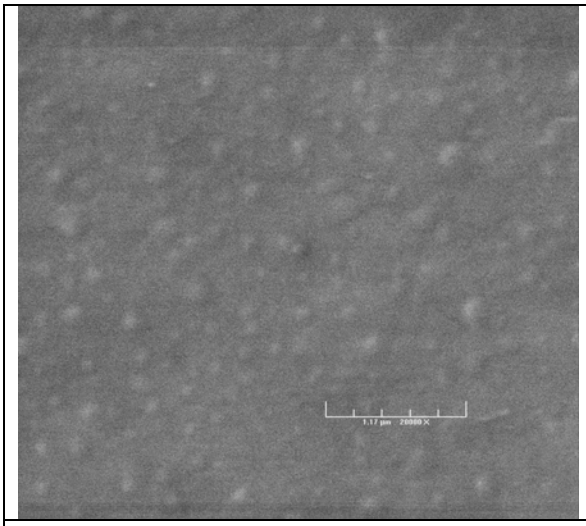

Fig. 7.2 (a) SEM image of glass-ceramic sample after hack of bulk sample to pieces (x20000)

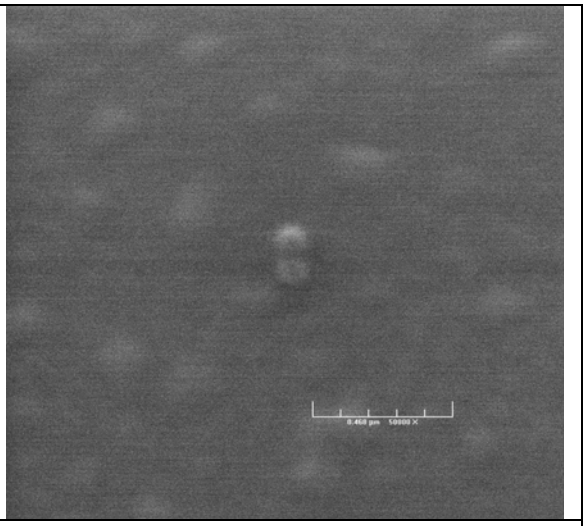

Fig. 7.2 (b) SEM image of glass-ceramic sample after hack of bulk sample to pieces (x50000)

7.2 Results of SEM Etching Experiments

A series of etching experiments were done in order to evaluate the number and size of crystallites using scanning electron microscopy. The Zeiss DSM 940 thermionic SEM with a resolution of 5 nm at 30 kV was used for imaging. It is designed for lower magnifications (100x to 20kx) and it is equipped with an x-ray detector for EDS. Fig. 7.1 shows what a typical glass should look like after an etching process. However all sets of experiments were unsuccessful in determining the crystal sizes or their number per unit area. The reasons for this can be one or a combination of the following, depending on the sample:

1) The surface in many experiments was “milky”, meaning the etching left a residue on the surface of the glass.
2) The crystallites were also etched away with the glass, and the surface was poorly seen with SEM.
3) The resolution of the SEM and the quality of images were not enough to determine the size or number of these crystals.

A list of some of the etching procedures attempted is shown below along with figures for selected samples. Each sample was cut and polished. Cut samples were than heat-treated above crystallization temperature to make sure that a significant number of crystallites were present in the glass-ceramic. After chemical etching samples were cleaned with ultra sound. The cleaned samples were then coated with gold or carbon for SEM imaging. Fig. 7.3 shows two samples with different etching procedures. It’s clearly seen that the surface is not what is expected.

List of Selected Samples:

Sample #1: Heat-treated for 1 hour, then 3 minutes in 20 drop HCl and 40 ml water.

Sample #2: Heat-treated for 1 hour, then 0.8% HF–0.2% HCl

Sample #3: Heat-treated 1 hour, then 0.8% Nitric Acid–0.2% HCl

Sample #4: Heat- treated 1 hour, then 0.8% Sulfuric acid –0.2% HCl

Sample #5: Heat-treated 1 hour, then Water/HCl. Ultrasound in acetone.

Sample #6: Heat-treated 1 hour. 3 mins in Water/HCl. Ultrasound in methanol.

Sample #7: Heat-treated 1 hour. 3 mins in Water/HCl. Ultrasound in water.

Sample #8: Heat-treated 1 hour. Ultrasound in methanol.

Sample #9: Heat-treated 1 hour. Ultrasound in acetone.

The etching experiments did not provide enough data to analyze the crystal size and number densities of Cr-doped Ca_2GeO_4-$Li_2O(Al_2O_3)$-B_2O_3. Another technique was applied to find these values. Instead of etching the glass-ceramics with an acid solution, the glasses were cut into thicker samples and heat treated for different times and temperatures. The next step was to crack these samples and use the clean and smooth surface of the glass for imaging. These surfaces were then gold coated or carbon coated for SEM. Carbon coating was done for X-ray analysis (EDAX). Images below show some of the results obtained after the samples were prepared using this technique. Fig. 7.4 (a) is a SEM image of a sample heat treated at 580 ^{0}C for 1 hour, above crystallization temperature. Fig.7.4 (b) is a sample with no heat treatment.

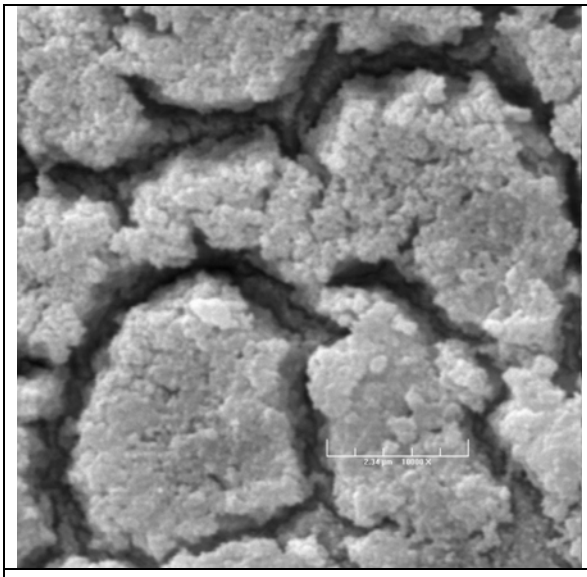

Fig. 7.3 (a) Sample #2: Heat-treated for 1 hour, then 0.8% HF–0.2% HCl

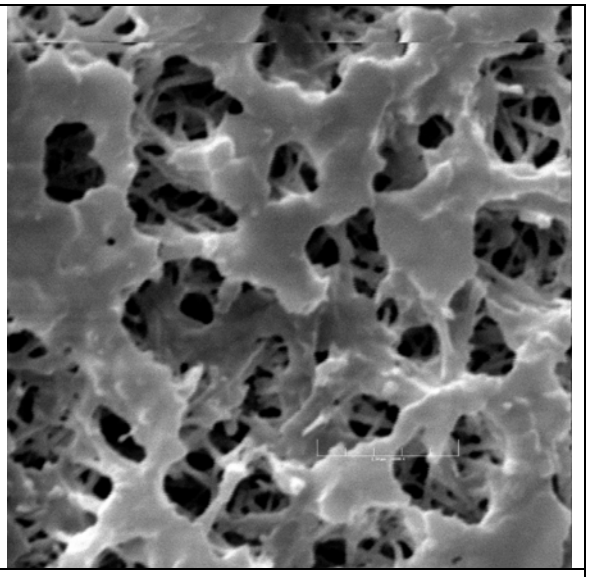

Fig. 7.3 (b) Heat- treated 1 hour, then 0.8% Sulfuric acid –0.2% HCl

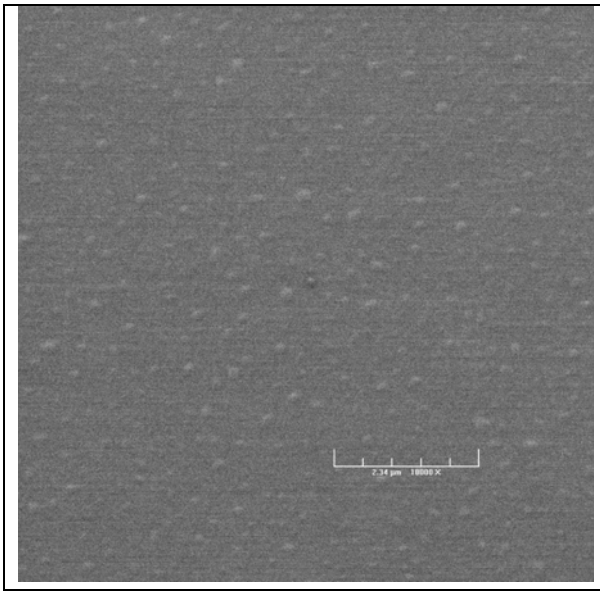

Fig.7.4 (a) SEM image of glass-ceramic sample after hack of bulk sample to pieces. Heat treated at 580 0C for 1 hour.

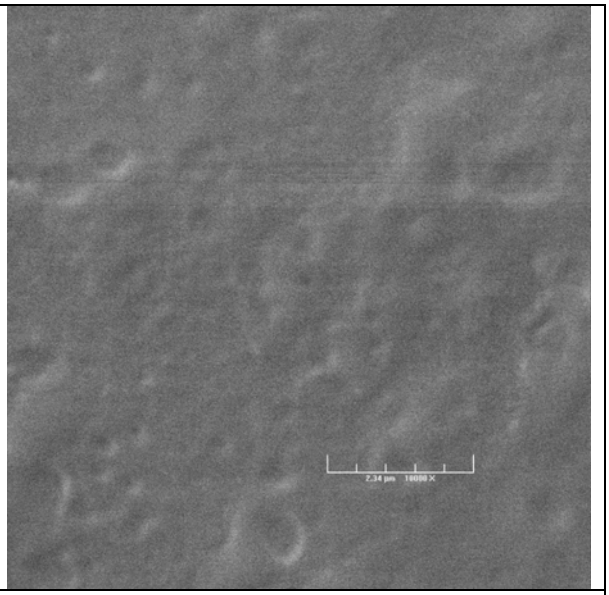

Fig.7.4 (b) SEM image of glass-ceramic sample after hack of bulk sample to pieces. No heat treatment

7.3 Confocal Microscopy

To conduct a series of confocal microscopy experiments a new glass of Ca_2GeO_4-$Li_2O(Al_2O_3)$-B_2O_3 was made with the same compositions as described in previous chapters. The only difference between this sample and the ones before is that instead of chromium, the sample was doped with a small percent of europium (about .1%). The reason europium was used and not chromium is that of its spectroscopic properties. Unlike chromium the europium when excited by green light (490-560 nm wavelength), emitts in the red spectral region (630-700 nm wavelength). By doping our samples with this ion, a confocal microscope can be used to image the surface and see the crystallites on the surface. A series of figures below (Fig. 7.5 (a-h)) show some of the results for samples for different heat-treatments and heat-treatment times. The results of these imaging experiments were not enough to make any conclusions on the exact size and number density of the crystals. After testing of this technique with different materials, i.e. alexandrite, ruby, and Ca_2GeO_4-$Li_2O(Al_2O_3)$-B_2O_3 glass, experiments showed that unlike alexandrite and ruby the Ca_2GeO_4 based glass had very low emissions after exciting it with the green light. Different techniques were used to amplify the emissions of the europium glass:

1) The amount of europium as a dopant was increased from .1% to .5% in Ca_2GeO_4-$Li_2O(Al_2O_3)$-B_2O_3 glass ceramic samples. This did not change the quality of images considerably.

2) A series of attempts was made in changing filters to find and isolate the region in which europium emits. Changing filters improved some of the images, but the resolution was still an issue.

3) Attempts were made to use the pinhole of the fiber optic laser and directly point it at the surface of the sample to have fewer losses from the light travel through the lenses. These attempts showed little improvement and were very difficult to put into practice, as holding and maintaining the laser steady and focusing were major issues.

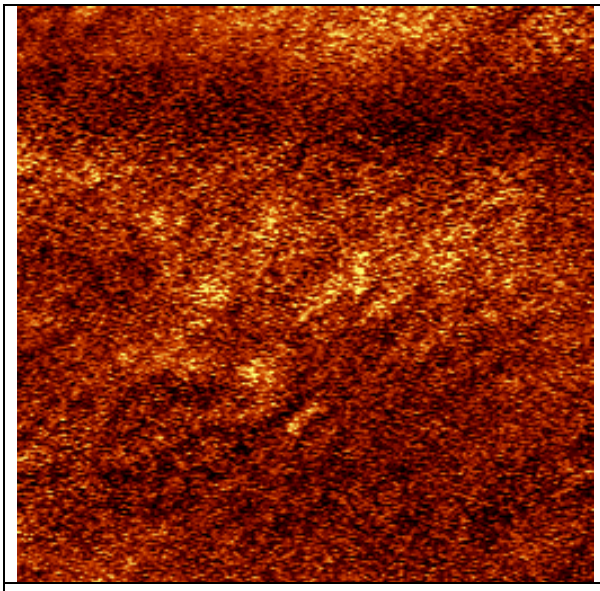

Fig.7.5 (a) Confocal image of a polished sample with no heat treatment. Image is 20x20 µm.

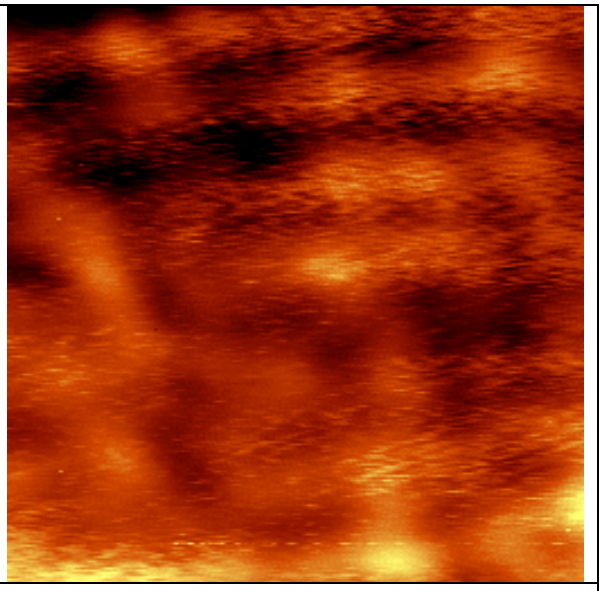

Fig.7.5 (b) Confocal image of sample heat treated at 560 ^{o}C for 1 hr. Image is 5x5 µm.

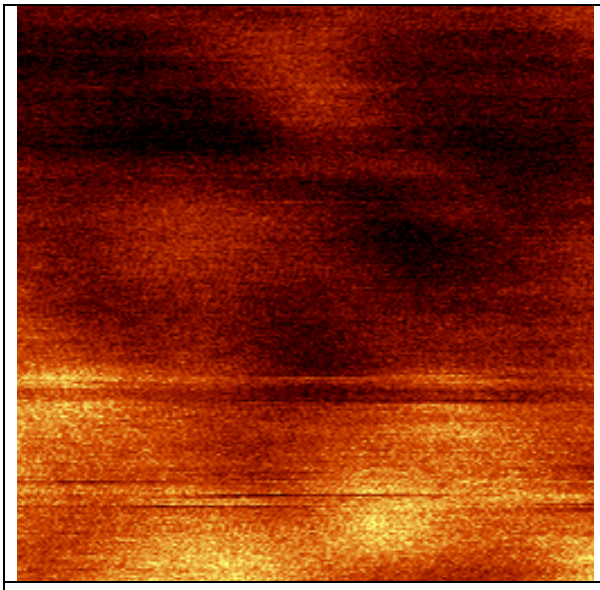

Fig.7.5 (c) Confocal image of sample heat treated at 590 ^{o}C for 9 hrs. Image is 2x2 µm.

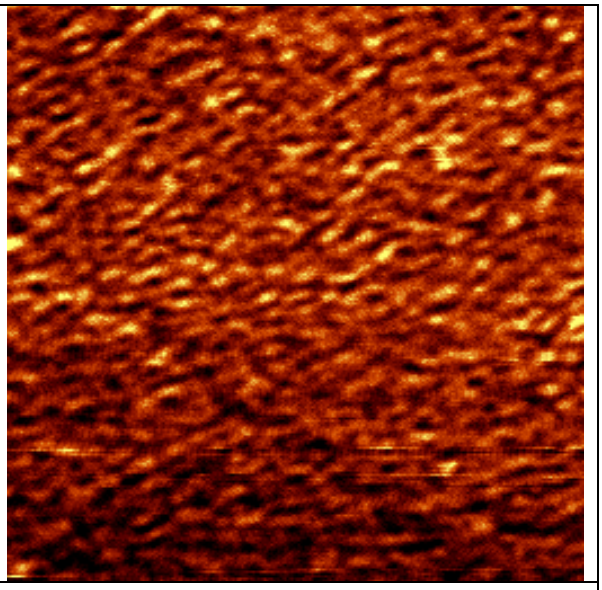

Fig.7.5 (d) Confocal image of sample heat treated at 530 ^{o}C for 24 hrs. Image is 20x20 µm.

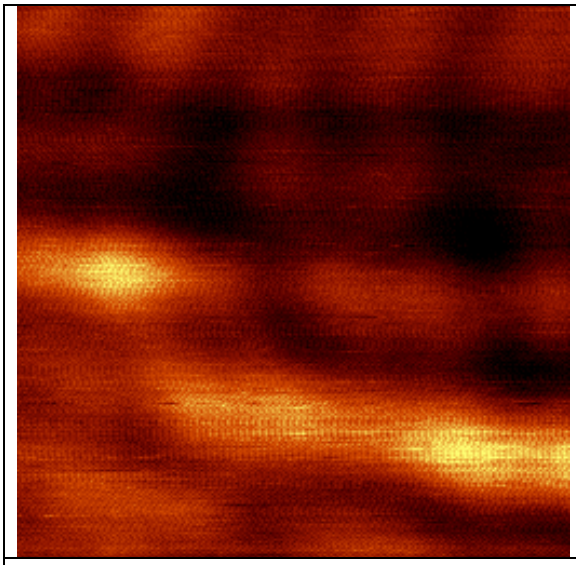

Fig.7.5 (e) Confocal image of sample heat treated at 525 ^{o}C for 6 hrs. Image is 5x5 µm.

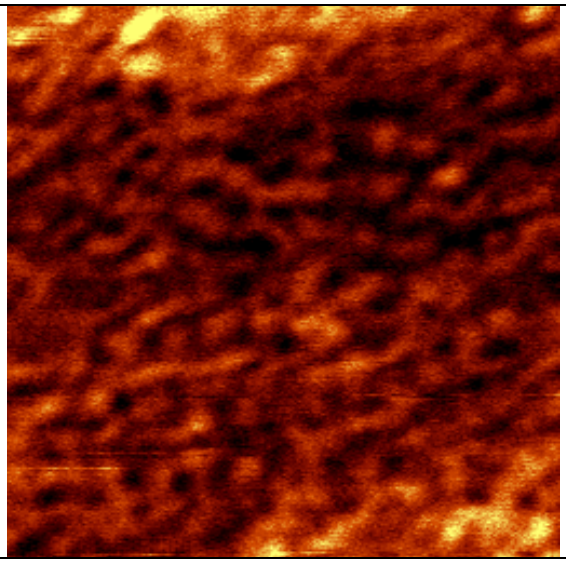

Fig.7.5 (f) Confocal image of sample heat treated at 500 ^{o}C for 24 hrs. Image is 10x10 µm.

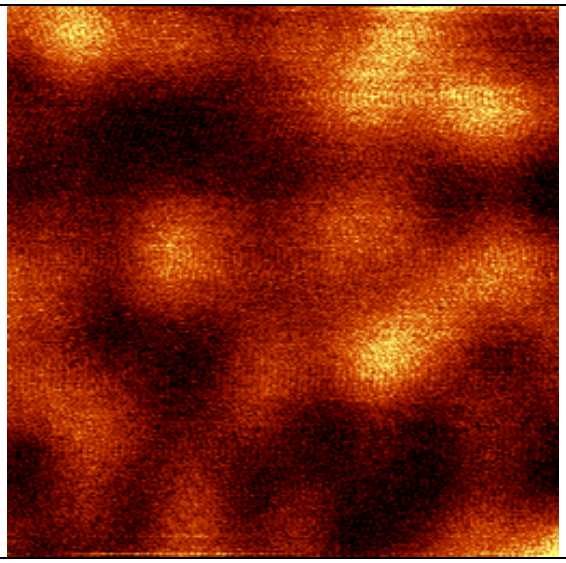

Fig.7.5 (g) Confocal image of sample heat treated at 500 ^{o}C for 24 hrs. Image is 3x3 µm.

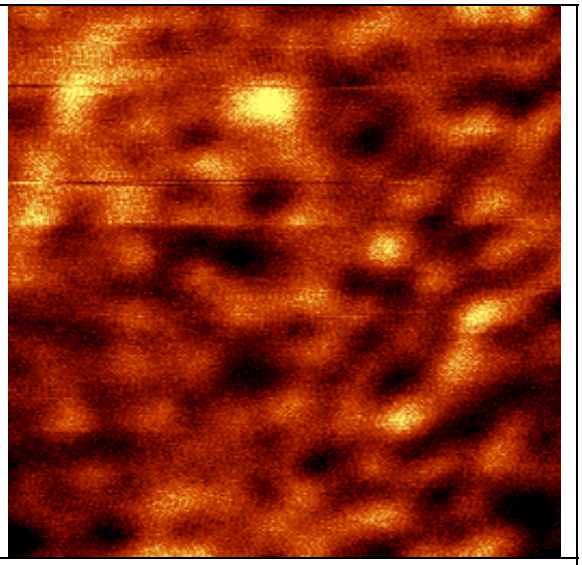

Fig.7.5 (h) Confocal image of sample heat treated at 500 ^{o}C for 24 hrs. Image is 5x6 µm.

7.4 High Resolution SEM

The Zeiss Supra 55 VP is a field emission SEM with a maximum resolution of 1 nm. It has the following capabilities: secondary and backscattered electron imaging in high vacuum or in variable pressure mode, low voltage scanning transmission electron microscopy (STEM), electron beam lithography, energy dispersive x-ray spectrometry (EDS) and electron backscatter diffraction (EBSD). This microscope was used to image Cr-doped Ca_2GeO_4-$Li_2O(Al_2O_3)$-B_2O_3 glass-ceramics to see the difference between quality of images from Section 5.3. The sample that was prepared for this experiment was first heat treated for 1 hour at a temperature of 520 ^{0}C, which is above the glass transition temperature. The sample was than cracked into smaller pieces. The cracked surfaces of the smaller pieces were used to image Cr-doped Ca_2GeO_4-$Li_2O(Al_2O_3)$-B_2O_3 crystallites. As seen in Fig.7.6 below, the images are very clear and imply that this

technique can be used with this high resolution microscope for crystal size and density analysis. The results show that the sizes of the crystals for this sample are 50-100 nm. A series of experiment will have to be done to further investigate the change in size and change in density of these crystals at different heat treatments and heat treatment times.

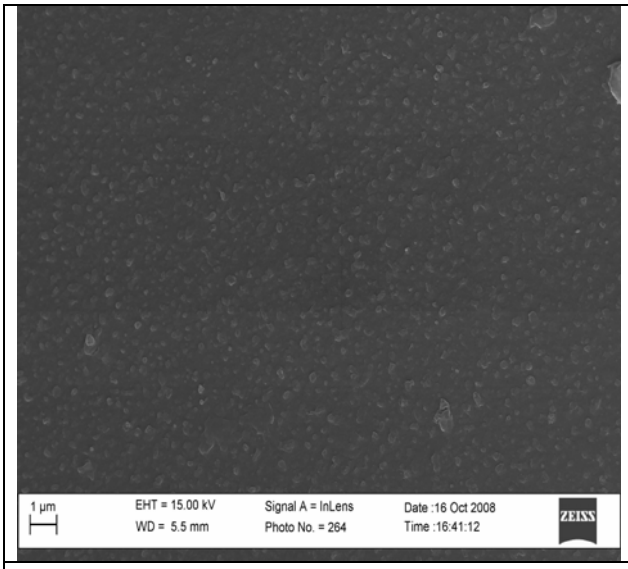

Fig.7.6 (a) SEM image of glass-ceramic sample after cracking the surface. Heat treated at 500 ^{o}C for 1 hour.

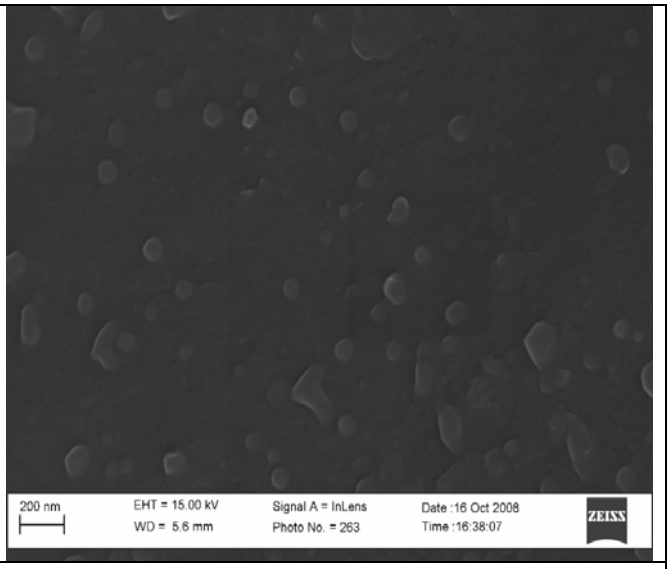

Fig.7.6 (b) SEM image of glass-ceramic sample after cracking the surface. Heat treated at 500 ^{o}C for 1 hour.

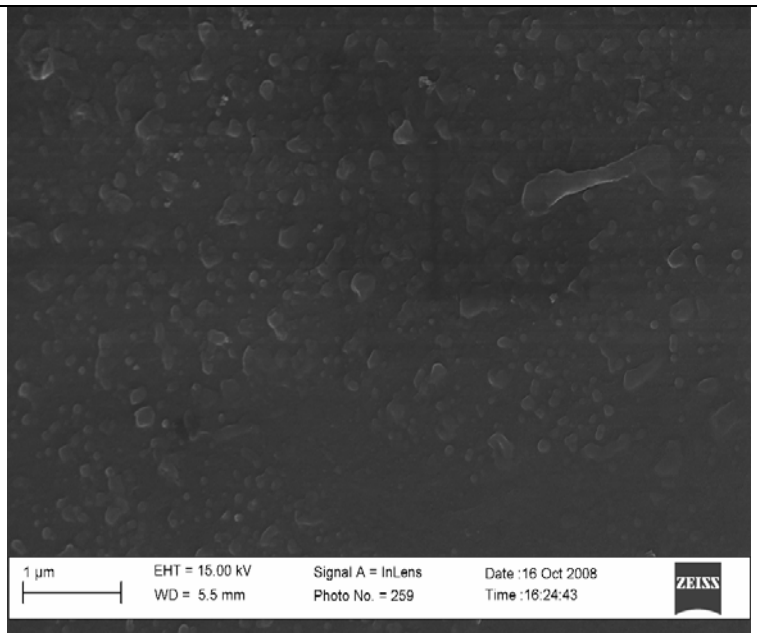

Fig.7.6 (c) SEM image of glass-ceramic sample after cracking the surface. Heat treated at 500^{o}C for 1 hour.

CHAPTER 8

CONCLUSIONS AND FUTURE WORK

8.1 Research Summary

The goal of the research presented in this thesis was to create new hybrid materials based on nanosize laser active crystallites embedded into a transparent glass matrix. Two different approaches were taken in order to make these materials: impregnation of porous glasses with Cr-doped olivine crystallites and synthesis of glass-ceramics nucleated with Cr-doped olivine nano-crystallites via conventional devitrification methods.

Two methods were employed in growing nano-crystallites. For the first method, Cr-doped calcium germanate gels were prepared by room-temperature acid hydrolysis. It was shown that Ca_2GeO_4 nanocrystals ~80 nm in size can be obtained at an unexpectedly low temperature (550^oC). Low temperature synthesis is critically important for the fabrication of small sized particles. For the second method, a precipitation technique was used for preparation of Cr-doped Mg_2GeO_4 olivine nano-crystallites. Particle size distribution was in the 200-800 nm range. The rather large size of the particles is due to not fully optimized initial chemical composition. More research is needed to fabricate smaller particles with uniform size distribution.

Hollow mesoporous spheres (HMS) were synthesized to use as a glass matrix for the nano-crystallites. Dark carbon-like material was formed with a wide pore distribution with the maximum at ~100 nm. Also, cubic mesoporous glasses, mobil crystalline material (MCM-48) were synthesized with the pore size of ~20nm. The MCM-48 was used in subsequent impragantion experiments due to its small pore size. The porous glass was immersed in ethanol solution of, an appropriate stoichiometric amount, germanium in the form of germanium tetraethoxide (Ge $(OC_2H_5)_4$ or TEOG) and calcium in the form of calcium nitrate (Ca $(NO_3)_2$). Heat treatments of the sample were done at ~ 600^{o}C, 700^{o}C, and 800^{o}C. Appearance of a Cr^{3+} type emission was observed after first heating to 600^{o}C.

Synthesis and devitrification behavior of Cr-doped $CaO–GeO_2–Li_2O–B_2O_3(Al_2O_3)$ glasses have been studied. A range of glass compositions was found to yield transparent glass-ceramics after devitrification. The size of the crystallites is below 1 μm. Glass-ceramic samples exhibit 1050–1600 nm broad-band emission with a maximum around 1260 nm, very similar to the emission of Cr^{4+}:Ca_2GeO_4 bulk crystals. X-ray diffraction measurements indicate that the structure of crystallites exhibiting near infrared emission in glass-ceramics may be assigned to Cr^{4+}:Ca_2GeO_4 with increased lattice parameters. Nucleation and crystallization kinetics of Cr-doped $CaO–GeO_2–Li_2O–B_2O_3(Al_2O_3)$ glasses were investigated. Activation energies were 530 KJ/mol for nucleation and 415KJ/mol for crystallization. The Avrami coefficient was found to be 3.7, suggesting 3-dimensional bulk crystallization within the glass.

8.2 Future Work

The study of transparent glass-ceramics is a new research field. The goal is to provide new materials with special optical properies. In recent years, fiberization of glass ceramic materials led to the demonstration of rare earth doped fiber lasers and amplifiers. The synthesis of glass-ceramics for these applications is cheaper than the conventional method of growing single crystals and not as difficult. Also, single crystals can not be used for some of the applications that glass-ceramics can. Cr^{4+}-doped glasses possess strong nonradiative processes that completely suppress the radiative emission and laser action. In contrast, glass-based hybrid materials containing nanometer to micro sized Cr^{4+}-doped crystals embedded in a glass matrix are intermediate between bulk crystals and glasses. This combination gives favorable radiative properties of Cr^{4+}-doped single crystals and the advantages of glasses for fiber optics.

Cr-doped $CaO–GeO_2–Li_2O–B_2O_3(Al_2O_3)$ is the first of its kind made at CCNY and proves to be a promising material for photonic applications. By further investigating the crystal nucleation and growth it can be improved and eventually may be used as an optical fiber. This material can open more possibilities in making Cr-doped glasses by the devitrification techniques investigated in this thesis. It will be interesting to see how these new materials will be employed into today's and future technology. The nano-scale optical materials are not only just a substitute for the single crystal laser material, but also open up new ways for the synthesis of laser materials. It provides us with the ability to manipulate the material's property on the nano-range, or even on the molecular level. This nano-technology has been described as the manufacturing technology of the 21^{st} century.

BIBLIOGRAPHY

1. Petricevic, V., S. K. Gayen, R. R. Alfano, Kiyoshi Yamagishi, H. Anzai, and Y. Yamaguchi, Appl. Phys. Lett. 52 (13), 28 March 1988
2. Petricevic, V., A. B. Bykov, J. M. Evans and R. R. Alfano, "Room temperature near-infrared tunable laser operations of Cr^{4+}:Ca_2GeO_4", Optics Letters, Vol 21, No. 21, 1996 pp 1~4.
3. Petricevic, V. *Ph. D. Thesis*, submitted to the faculties of the Department of Physics of CCNY and the Graduate School of CUNY, (1990)
4. Petricevic, V., S. K. Gayen, and R. R. Alfano, Appl. Phys. Lett. 53, 2590 (1988).
5. P.W. McMillan. Non-Metalic Solids - Volume 1: Glass-ceramics. Academic Press, London, 1964.
6. P. A. Tick, N. F. Borrelli, L. K. Cornelius and M. A. Newhouse. Transparent glass ceramics for 1300 nm amplifier applications. *Journal of Applied Physics*, 78, 6367, 1995.
7. Y. Wang and J. Ohwaki. New transparent vitroceramics codoped with Er^{3+} and Yb^{3+} for efficient frequency upconversion. *Applied Physics Letters*, 63, 3268, 1993.
8. Y.-H. Kao, Y. Hu, H. Zheng and J. D. Mackenzi. Second harmonic generation in transparent barium borate glass-ceramics. *Journal of Non-Crystalline Solids*, 167, 247, 1994.
9. Y. Takahashi, T. Fujiwara, T. Komatsu, and T. Benino. Second harmonic generation in transparent surface crystallized glasses with stillwellite-type $LaBGeO_5$. *Journal of Applied Physics*, 89, 5282, 2001.
10. Isabella-Iona Oprea *Ph.D Thesis,* Department of Physics of University of Osnabruck, (2005).
11. W. H. Zachariasen. The atomic arrangement in glass. *Journal of American Chemical Society*, 54, 3841, 1932.
12. Ostwald W.Z. (1887). Zeit Physik Chemie, 22, 289-330.

13. E. Muller, K. Heide, and E. D. Zanotto. Molecular structure and nucleation in silicate glasses. *Journal of Non-Crystalline Solids*, 155, 56, 1993.
14. Newton, Roy and Davison, Sandra. Conservation and Restoration of a Glass. Butterworth-Heinemann, 2003.
15. L. Pauling, "The principles determining the structure of complex ionic crystals". *J. Am. Chem. Soc.* **51** (4): 1010–1026. 1929.
16. P.W. McMillan. Non-Metalic Solids - Volume 1: Glass-ceramics. Academic Press, London, 1964.
17. G. H. Beall. Property and process development in glass-ceramics materials. *Corning Glass Works*, 1953.
18. Mayolet, A. Kerdoncuff and C. Pierron, in CLEO Proceedings, (2001) p. 211
19. M. Yamane and Y. Asahara. *Glasses for Photonics*. Cambridge University Press, Cambridge, 2000.
20. H. Bach and D. Krause. *Low Thermal Expansion Glass Ceramics*. Springer, 2005
21. W. Ostwald. 1896. *Lehrbuch der Allgemeinen Chemie*, vol. 2, part 1. Leipzig, Germany
22. Merriam-Webster Online. 3 March 2009 http://www.merriam webster.com/dictionary/citation
23. C.Newey, G. Weaver. Materials Principles & Practice, Butterworth-Heinemann, (March 23, 1990)
24. D. Turnbull and J.C. Fischer, J. Chem. Phys. 17 (1949) 71.
25. A.N. Kolmogorov, Izv. Akad. Nauk. SSR 3 (1937) 355.
26. Schmelzer, Jurn. Nucleation Theory and Applications. Wiley-VCH, 2005.
27. W.A. Johnson, R. Mehl, Trans. AIME 135 (1939) 416.
28. M. Avrami, J. Chem. Phys. 7 (1939) 1103.
29. M. Avrami, J. Chem. Phys. 8 (1940) 212.
30. M. Avrami, J. Chem. Phys. 8 (1941) 177.
31. A.A. Cabral, V.M. Fokin, E.D. Zanotto, C.R. Chinaglia, "Nanocrystallization of Fresnolite Glass. I. Nucleation and Growth Kinetics," *Journal of Non-Crystalline Solids,* 330 (2003) 174-186.

32. A. Arora, A. Goel, E.R. Shaaban, K. Singh, O.P. Pandey, J.M.F Ferreira, "*Crystallization kinetics of BaO–ZnO–Al2O3–B2O3–SiO2 glass*," Physica B (2007)
33. J. Va´ zquez, C. Wagner, P. Villares, R. Jime´ nez-Garay, J. Non-Cryst. Solids 235–237 (1998) 548.
34. J. Va´zquez, C. Wagner, P. Villares and R. Jime´nez-Garay, Acta Mater 44 (1996) 4807.
35. H. Yinnon and D.R. Uhlmann, J. Non-Cryst. Solids 54 (1983) 253.
36. H.E. Kissinger, Anal. Chem. 29 (1957) 1702.
37. K. Matusita, T. Konatsu and R. Yorota, J. Mater. Sci. 19 (1984) 291.
38. Baxter, R.A., in "Thermal Analysis" (Schwenker, R.F., Jr. and Garn, P.D., Editors). Vol. 1, Academic Press, New York, NY, 1969.
39. Yu, Francis and Yang, Xiangyang. Introduction to Optical Engineering. Cambridge University Press, 1997.
40. Hazenkamp, H., U. Gudel, M. Atanasov, U. Kesper and D. Reinen, Phys. Rev. B53, 2367 (1996).
41. Hazenkamp, M. F. *et al* "Absorption and luminescence spectroscopy of Cr^{4+} - doped Ca_2GeO_4. A potential near infrared laser material" Chemical Physics Letters, **233** (1995) 466-470
42. Moulton, P. F. "Tunable Paramagnetic-Ion Lasers" in Laser Handbook, Vol 5, M. Bass and M.L. Stitch ed. pp203-288 (1986)
43. McClure, D. S. in *Solid State Physics*, Vol 9, F. Seitz and D. Turnbull, eds., (Acdemic, New york, 1959) p 408
44. Manku, G.S. Theoretical Principles of Inorganic Chemistry. Tata McGraw-Hill, 1980.
45. D.Yao, *Ph.D. Thesis*, submitted to the faculties of the Department of Chemical Engineering of CCNY and the Graduate School of CUNY, (1998)
46. Merriam-Webster Online. 8 March 2009 http://www.merriam webster.com/dictionary/citation

47. Micrometrics Gemini Series Manual. <http://www.pss.aus.net/products/micromeritics/equip_surface_area/2375/2375.html>
48. Pinckney, N. F. Borrelli, A. Mayolet, A. Kerdoncuff, and C. Pierron, ''Cr^{4+}:forsterite nanocrystalline glass–ceramic fiber,'' in *Conference on Lasers and Electro-Optics (CLEO)*, Vol. 56 of OSA Trends in Optics and Photonics Series (Optical Society of America, Washington, D.C., 2001), pp. 211– 212.
49. G. Laudisio, M. Catauro and G. Luciani. 'Non-isothermal devitrification of strontium germanate glasses.", Materials Chemistry and Physics, Volume 58, Issue 2, 25 March 1999
50. M. Catauro and A. Marotta. "The non-isothermal devitrification of glasses in the $CaO{\cdot}4GeO_2$–$SrO{\cdot}4GeO_2$ composition range", *Thermochimica Acta, Volume 371, Issues 1-2, 26 April 2001, Pages 121-126.*
51. M. Catauro, S. Gargano and G. Laudisio. The non-isothermal devitrification of glasses in the $CaO{\cdot}4GeO_2$–$BaO{\cdot}4GeO_2$ composition range, *Thermochimica Acta, Volume 356, Issues 1-2, 7 August 2000, Pages 127-131*
52. J. Deubener, Structural aspects of volume nucleation in silicate glasses, *Journal of Non-Crystalline Solids* 351 (2005) 1500–1511
53. Vladimir M. Fokin , Edgar D. Zanotto , Nikolay S. Yuritsyn , JuËrn W.P. Schmelzer Homogeneous crystal nucleation in silicate glasses: A 40 year perspective Journal of Non-Crystalline Solids 352 (2006) 2681–2714.
54. Alfred Margaryan, Michael A. Piliavin, Germanate Glasses: Structure, Spectroscopy, and Properties, Artech House, Boston-London, 1993, p.142.
55. O. K. Geokchya, K. A. Kostanyan, A. M. Sheviakov, and I. V. Tarlakov, Arm. Chem. Jour., 27 (1974) 643.
56. Man Feng and Setsuhisa Tanabe, Optical Materials, 20 (2002) 63.
57. Z. Strnad, Glass-Ceramic materials, Elsevier , Amsterdam-Oxford-New York – Tokio, 1986
58. Rahul Vaish, K.B.R. Varma, Journal of Crystal Growth 307 (2007) 477–482
59. C.T. Moynihan, A.J. Easteal and J. Wilder, J. Phys. Chem. 78 (1974) 2673.
60. J.A. Augis and J.E. Bennett, J. Therm. Anal. 13 (1978) 283.

61. T Ozawa, H Suzuki and M Tanaka. Proc Natl Acad Sci U S A. 1980 February; 77(2): 928–930.